Stockholm
University

Probing Paramagnetic Systems by Solid-State NMR Spectroscopy

José P. Carvalho

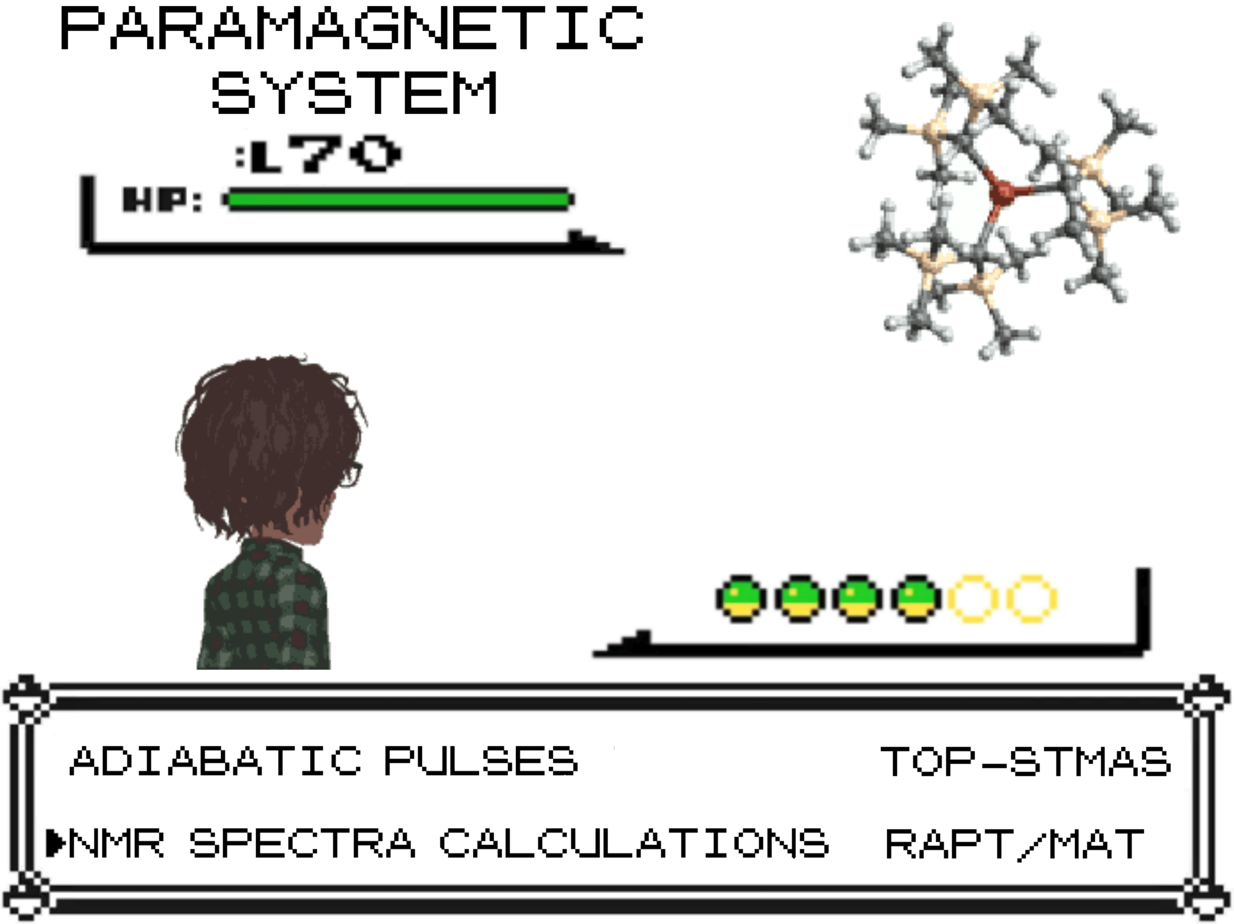
PARAMAGNETIC
SYSTEM
:L70
HP:
ADIABATIC PULSES
TOP-STMAS
▶NMR SPECTRA CALCULATIONS
RAPT/MAT

Doctoral Thesis in Physical Chemistry at Stockholm University, Sweden 2022

Probing Paramagnetic Systems by Solid-State NMR Spectroscopy

José P. Carvalho

Academic dissertation for the Degree of Doctor of Philosophy in Physical Chemistry at Stockholm University to be publicly defended on Wednesday 4 May 2022 at 14.00 in Magnélisalen, Kemiska övningslaboratoriet, Svante Arrhenius väg 16 B.

Abstract

Paramagnetic systems have a wide range of applications ranging from energy storage or conversion to catalytic processes, metalloproteins and light-emitting materials. Over the recent years nuclear magnetic resonance (NMR) spectroscopy has become an established tool for studying the structural and electronic properties of these systems, largely because it can provide a link between the structure and the bulk properties. This progress was only possible due to improved probe technology and better radiofrequency irradiation schemes, since the hyperfine interaction between nuclei and the unpaired electrons generally hampers both the acquisition and interpretation of the spectra and, therefore, techniques that are standard for diamagnetic systems often perform poorly when applied to paramagnetic systems.

The aim of the present thesis is to continue the development of solid-state paramagnetic NMR and address some of the remaining limitations and bottlenecks in the acquisition and spectral interpretation. One specific area for which great improvements have been seen is the development of new broadband excitation and inversion sequences for systems under Magic-Angle Spinning (MAS) which employ adiabatic pulses. In this work, we provide a more rigorous understanding of the adiabatic pulses in solid-state MAS NMR applicable to both the design of new and improved pulse schemes, and their application in studies of an increased variety of systems, whilst avoiding potential implementation pitfalls.

We also demonstrate how a thorough understanding of the hyperfine interaction combined with quantum chemistry calculations can link bulk magnetic properties and magnetic resonance signatures both in solid-state NMR and Electron Paramagnetic Resonance (EPR), thus providing an accurate description of the geometry and electronic configuration of an organoytterbium complex with applications in heterogeneous catalysis.

Lastly, we explore the development of methods suitable for quadrupolar nuclei (spin $I>1/2$) in paramagnetic systems which have, so far, lagged behind their spin 1/2 counterparts. We focus more specifically on half-integer quadrupoles for which we propose a new method of processing Multiple-Quantum and Satellite-Transition MAS spectra which permits the separation of shift and quadrupolar interactions into orthogonal dimensions and evaluate the performance and limitations of the state-of-the-art methods for extraction of both quadrupolar and shift anisotropy tensor parameters on structurally complex systems.

We anticipate that the work developed throughout this thesis can help extend the fields of application of solid-state paramagnetic NMR.

Keywords: *Solid-state NMR, Magic-Angle Spinning, Paramagnetic NMR, Frequency-Swept Adiabatic Pulses, Quantum Chemistry, Quadrupolar Interaction.*

Stockholm 2022
http://urn.kb.se/resolve?urn=urn:nbn:se:su:diva-202959

ISBN 978-91-7911-826-6
ISBN 978-91-7911-827-3

Stockholm University

Department of Materials and Environmental Chemistry (MMK)

Stockholm University, 106 91 Stockholm

PROBING PARAMAGNETIC SYSTEMS BY SOLID-STATE NMR SPECTROSCOPY

José P. Carvalho

Stockholm
University

Probing Paramagnetic Systems by Solid-State NMR Spectroscopy

José P. Carvalho

©José P. Carvalho, Stockholm University 2022

ISBN print 978-91-7911-826-6
ISBN PDF 978-91-7911-827-3

Printed in Sweden by Universitetsservice US-AB, Stockholm 2022

Doctoral Thesis in Physical Chemistry 2022

Department of Materials and Environmental Chemistry
Stockholm University
SE-10691, Sweden

Faculty Opponent:

Prof. Sharon Ashbrook
School of Chemistry
University of St Andrews
United Kingdom

Evaluation Committee:

Dr. Dominique Massiot
Director of Research
Conditions Extrêmes et Matériaux:
Haute Température et Irradiation (CEMHTI)
CNRS
France

Prof. Daniel Topgaard
Department of Chemistry
Lund Universitet
Sweden

Prof. Thomas Vosegaard
Interdisciplinary Nanoscience Center
Aarhus Universitet
Denmark

Substitute:

Prof. Istvan Furo
Head of Department
Department of Chemistry
Kungliga Tekniska högskolan
Sweden

I heard this story about a fish.
He swims up to this older fish and says,
"I'm trying to find this thing they call the ocean."
"The ocean?" says the older fish.
"That's what you're in right now."
"This?" says the young fish.
"This is water. What I want is the ocean."

Docter, P. H. (2020). Soul. Pixar Animation Studios

List of Publications

This dissertation is based on the following papers, referred to in the text by their Roman numerals.

PAPER I: **Frequency-swept adiabatic pulses for broadband solid-state MAS NMR**
José P Carvalho, Andrew J. Pell, *Journal of Magnetic Resonance*, **324**, 106911 (2021).
DOI: j.jmr.2020.106911
Scientific Contributions: Acquisition of the NMR spectra, simulations and writing of the manuscript.

PAPER II: **Geometry and electronic structure of of Yb(III)[CH(SiMe$_3$)$_2$]$_3$ from experimental and computational diffraction and magnetic resonance spectroscopies**
Anton Ashuiev, Florian Allouche, José P. Carvalho, Kevin Sanders, Matthew P. Conley, Daniel Klose, Giuseppe Lapadula, Michael Wörle, Dirk Baabe, Marc D. Walter, Andrew J. Pell, Christophe Copéret, Gunnar Jeschke, Guido Pintacuda, Richard A. Andersen - Manuscript in preparation
Scientific Contributions: Quantum chemical calculations, spectral analysis and fitting and leading role in writing of the manuscript.

PAPER III: **Half-integer-spin quadrupolar nuclei in magic-angle spinning paramagnetic NMR: The case of NaMnO$_2$**
José P. Carvalho, Wassilios Papawassiliou, Andrew J. Pell, *Journal of Magnetic Resonance* - Submitted Manuscript
Scientific Contributions: Acquisition of the NMR spectra, spectral fitting and analysis and writing of the manuscript.

PAPER IV: **Separation of quadrupolar and paramagnetic shift interactions with TOP-STMAS/MQMAS in solid-state lighting phosphors**
José P. Carvalho, Aleksander Jaworski, Michael J. Brady, Andrew J. Pell, *Magnetic Resonance in Chemistry*, **58**, 1055– 1070 (2020).
DOI: 10.1002/mrc.5004
Scientific Contributions: Acquisition of the NMR spectra, NMR simulations, spectral analysis and fitting, quadrupolar parameter calculations and writing of the manuscript.

Reprints were made with permission.

Publications not included in this thesis:

PAPER A: **Emergent Weyl fermions in WTe2 probed with Electron-States-Resolved NMR crystallography**
Wassilios Papawassiliou, José P. Carvalho, Hae Jin Kim, Chang-Yeon Kim, Seung Jo Yoo, Jin Bae Lee, Saeed Alhassan, Savvas Orfanidis, Vassilios Psycharis, Marina Karagianni, Michael Fardis, Nikolaos Panopoulos, Georgios Papavassiliou, Andrew J. Pell *Physical Review Research* - Under Review
arXiv: 2110.01300
Scientific Contributions: Collaborated in the acquisition of Tellurium 125 NMR spectra, spectral analysis and NMR simulations.

PAPER B: **Crystal and electronic facet analysis of ultrafine Ni_2P particles by solid-state NMR nanocrystallography**
Wassilios Papawassiliou, José P. Carvalho, Nikolaos Panopoulos, Yasser Al Wahedi, Vijay Kumar Shankarayya Wadi, Xinnan Lu, Kyriaki Polychronopoulou, Jin Bae Lee, Sanggil Lee, Chang Yeon Kim, Hae Jin Kim, Marios Katsiotis, Vasileios Tzitzios, Marina Karagianni, Michael Fardis, Georgios Papavassiliou, Andrew J. Pell , *Nature Communications*, **12-1**, 4334 (2021).
DOI: 10.1038/s41467-021-24589-5
Scientific Contributions: Spectral fitting and analysis.

PAPER C: **Artefact-free broadband 2D NMR for separation of quadrupolar and paramagnetic shift interactions**
Rihards Aleksis, José P. Carvalho, Aleksander Jaworski, Andrew J. Pell, *Solid State Nuclear Magnetic Resonance*, **101**, 51-62 (2019).
DOI: 10.1016/j.ssnmr.2019.05.001B
Scientific Contributions: Programming the spectral fitting and error estimation software in C++.

PAPER D: **Insights into the structural evolution during electrochemical cycling of the Na-ion battery anode Bi2Te3 through solid-state NMR crystallography - Manuscript in preparation**
Wassilios Papawassiliou, José P. Carvalho, Ronan Le Ruyet, William Brant, Andrew J. Pell - Manuscript in preparation
Scientific Contributions: Acquisition and analysis of Sodium 23 NMR spectra.

PAPER E: **Indium(III) in the "Periodic Table" of Di(2-pyridyl) Ketone: An Unprecedented Transformation of the Ligand and Solid-State ^{115}In NMR Spectroscopy as a Valuable Structural Tool**
Christina Stamou, Wassilios Papawassiliou, José P. Carvalho, Konstantis F. Konidaris, Vlasoula Bekiari, Pierre Dechambenoit, Andrew J. Pell, Spyros P. Perlepes, *Inorganic Chemistry* **60**, 4829-4840 (2021).
DOI: 10.1021/acs.inorgchem.0c03725
Scientific Contributions: Collaborated in the acquisition of Indium 115 NMR spectra, DFT calculations, spectral analysis and fitting and in the writing the NMR part of the manuscript.

PAPER F: **A biocompatible ZnNa2-based metal–organic framework with high ibuprofen, nitric oxide and metal uptake capacity**
Meghan Winterlich, Constantinos G. Efthymiou, Wassillios Papawassiliou, José P Carvalho, Andrew J. Pell, Julia Mayans, Albert Escuer, Michael P. Carty, Patrick McArdle, Emmanuel Tylianakis, Liam Morrison, George Froudakis, Constantina Papatriantafyllopoulou, *Materials Advances*, **1-7**, 2248-2260 (2020).
DOI: 10.1039/D0MA00450B
Scientific Contributions: Acquisition of Sodium 23 NMR spectra, spectral analysis and fitting and collaborated in the writing the NMR part of the manuscript.

Contents

Abbreviations **xvii**

List of Figures **xix**

List of Tables **xxvii**

1 Introduction **1**

2 NMR of Paramagnetic Solids: Theoretical Background **3**
- 2.1 Chemical Shift Interaction . . . 4
- 2.2 Quadrupolar Interaction . . . 5
- 2.3 Magic-angle Spinning . . . 7
  - 2.3.1 Spinning Sidebands . . . 8
  - 2.3.2 Quadrupolar Nuclei under MAS . . . 8
- 2.4 Paramagnetic effects in solid-state NMR . . . 11
  - 2.4.1 Line broadening from BMS effects . . . 14
  - 2.4.2 Paramagnetic relaxation enhancement . . . 15

3 Basics of Quantum Chemistry **17**
- 3.1 Wave function-based methods . . . 17
- 3.2 Density functional theory . . . 19
- 3.3 Basis sets . . . 20

4 Adiabatic Pulses in Solid-State MAS NMR: A Unified Analysis **21**
- 4.1 Theory of adiabatic pulses for solids under MAS . . . 23
  - 4.1.1 High-power regime . . . 24
  - 4.1.2 Low-power regime . . . 28
  - 4.1.3 Intermediate-power regime . . . 31
- 4.2 Applications . . . 34

5 Geometry and Electronic Structure of Yb(III)[CH(SiMe$_3$)$_2$]$_3$ **37**
- 5.1 Structural characterization . . . 38
- 5.2 EPR characterization and magnetic susceptibility studies . . . 39
- 5.3 NMR characterization . . . 40

6 Extraction of NMR Parameters of Half-Integer Quadrupolar Nuclei in Paramagnetic Systems **47**
- 6.1 RAPT . . . 48
- 6.2 MQMAS/STMAS . . . 51
  - 6.2.1 TOP-STMAS/MQMAS . . . 54

7 Summary **63**
7.1 Sammanfattning (Summary in Swedish) 65
7.2 Resumo (Summary in Portuguese) 67

Acknowledgements **69**

References **71**

Abbreviations

ABMS	Anisotropic Bulk Magnetic Susceptibility
aMAT	Adiabatic MAT
BMS	Bulk Magnetic Susceptibility
CASSCF	Complete Active Space Self-Consistent Field
CC	Coupled Cluster
CI	Configuration Interaction
Con.	Fermi-Contact Shift
CP	Cross-polarization
CSA	Chemical Shift Anisotropy
CT	Central Transition
CTP	Coherence Transfer Pathway
CW	Continuous-Wave
DFT	Density Functional Theory
EDNMR	ELDOR-Detected NMR
EFG	Electric Field Gradient
ELDOR	Electron Electron Double Resonance
EPR	Electron Paramagnetic Resonance
GGA	Generalized Gradient Approximation
GTO	Gaussian-Type Orbital
HETCOR	Heteronuclear Correlation
HF	Hartree-Fock
HYSCORE	Hyperfine Sub-level Correlation
IBMS	Isotropic Bulk Magnetic Susceptibility
LDA	Local Density Approximation
Ln	Lanthanide

MAS	Magic-Angle Spinning
MAT	Magic-Angle Turning
MBPT	Many-Body Perturbation Theory
MCSCF	Multi-Configuration Self-Consistent Field
meta-GGA	Meta-GGA
MP	Møller-Plesset
MP*n*	*N*th Order MP Perturbation Theory
MQMAS	Multiple Quantum MAS
MRI	Magnetic Resonance Imaging
NEVPT2	*N*-Electron Valence State Second-Order Perturbation Theory
NMR	Nuclear Magnetic Resonance
PAF	Principal Axis Frame
PASS	Phase Adjusted Spinning Sidebands
PCS	Pseudo-Contact Shift
PCS,LR	Long-range Intramolecular Pseudo-Contact Shift
PNMR	Paramagnetic NMR
PRE	Paramagnetic Relaxation Enhancements
RAPT	Rotor-Assisted Population Transfer
RF	Radiofrequency
SA	Shift Anisotropy
SAF	Superadiabatic Frame
SCS-MP2	Spin-Component Scaled MP2
SE	Semi-empirical
SHAP	Short High-Power Adiabatic Pulse
SOC	Spin-Orbit Coupling
ssNMR	Solid-State Nuclear Magnetic Resonance
ST	Satellite Transition
STMAS	Satellite Transition MAS
STO	Slater-Type Orbital
TEDOR	Transferred Echo Double Resonance
VOCS	Variable Offset Cumulative Spectroscopy
WURST	Wideband, Uniform Rate, Smooth Truncation
YAG	Yttrium Aluminum Garnets

List of Figures

2.1 Simulated spectra of a paramagnetic system subject to a shielding interaction. The high-resolution, isotropic solution spectrum is shown in (a), exhibiting a single peak at the isotropic offset. A powder sample in the solid-state gives the classic CSA powder pattern in (b), which splits into a series of spinning sidebands under MAS, as shown in (c). The chemical shielding parameters are $-\omega_0\Delta\sigma/2\pi = 500$ kHz, and $\eta = 0.3$, and the frequency is measured relative to the isotropic offset Ω_{iso}. Adapted from [11], with permission from Elsevier. 8

2.2 Simulated powder spectra of a spin $I = 3/2$ nucleus subject to a first-order quadrupolar interaction: (a) Static spectrum. (b) and (c) Expansions of (a) to highlight the broad ST resonances and the CT, respectively. (d) MAS spectra at 60 kHz spinning speed. (e) Expansion of (d) to highlight the CT resonance. The quadrupolar interaction parameters are C_Q = 3.3 MHz (corresponding to $\omega_q/2\pi$ = 825 kHz), η_Q = 0.21. The nuclear Larmor frequency is $\omega_0/2\pi = -105.9$ MHz. Adapted from [11], with permission from Elsevier. 9

2.3 Simulated powder spectra of a spin $I = 3/2$ nucleus subject to a first- and second order quadrupolar interaction: (a) Static spectrum. (b) and (c) Expansions of (a) to highlight the broad ST resonances and the CT, respectively. (d) MAS spectra at 60 kHz spinning speed. (e) Expansion of (d) to highlight the CT resonance. The quadrupolar interaction parameters are C_Q = 3.3 MHz (corresponding to $\omega_q/2\pi$ = 825 kHz), η_Q = 0.21. The nuclear Larmor frequency is $\omega_0/2\pi = -105.9$ MHz. Adapted from [11], with permission from Elsevier. 11

2.4 Illustration of the bulk magnetic susceptibility effects. The nuclei in the positions denoted in orange, red, purple do not experience the same nuclear shielding due to the nearby crystallites. Adapted from [46]. 15

4.1 Amplitude $\omega_1(t)$ (a)-(c), phase $\phi_{\mathrm{pul}}(t)$ (d)-(f), and frequency-sweep profiles (g)-(h) for hyperbolic secant [80], tanh/tan [81] and WURST [82] frequency-swept adiabatic pulses. All waveforms have symmetric amplitudes and phases with respect to the midpoint of the pulse ($t = \tau_p/2$). It is also worth noting that close to the midpoint of the pulse, the frequency-sweep behaves approximately linearly. Adapted from [11], with permission from Elsevier. 22

4.2 Simulated inversion profile and superadiabatic factor [87] contour plots for a SHAP (tanh/tan waveform, $\Delta\omega_1/2\pi = 5$ MHz, $\tau_p = 100$ μs) as a function of MAS rate and peak RF field strength for a single crystal, transcribed from paper I. The simulations were carried out considering an SA tensor with asymmetry parameter $\eta = 0.5$ and 60 kHz ((a) and (c)) and 500 kHz ((b) and (d)) anisotropy. The chosen crystal orientation was $\Omega_{\mathrm{PR}} = (0, \pi/4, 0)$. The z magnetization components after pulse irradiation were calculated via numeric integration of the Liouville-von Neumann equation, using the SA Hamiltonian in the rotating-frame, equation (4.2). The white lines highlight the rotary resonance conditions $\omega_1^{\mathrm{max}} = \omega_{\mathrm{MAS}}$ and $\omega_1^{\mathrm{max}} = 2\,\omega_{\mathrm{MAS}}$, and the dashed lines delineate the additional rotary resonance conditions with a periodicity in the MAS frequency dimension of 22 kHz. The superadiabatic factors were obtained numerically according to equations (4.13), (4.17) and (4.18), also considering the SA Hamiltonian in the rotating-frame. 27

4.3 Simulated inversion profile and superadiabatic factor [87] contour plots for an S^{3}AP (WURST waveform, $\Delta\omega_1 = \omega_{\mathrm{MAS}}$, $\tau_p = 1$ ms) as a function of MAS rate and peak RF field strength for a single crystal, transcribed from paper I. The $z-$magnetization components after pulse irradiation were calculated via numeric integration of the Liouville-von Neumann equation, using the SA Hamiltonian in the rotating-frame, equation (4.2). The simulations were carried out considering an SA tensor with asymmetry parameter $\eta = 0.5$ and 60 kHz ((a) and (c)) and 500 kHz ((b) and (d)) anisotropy. The chosen crystal orientation was $\Omega_{\mathrm{PR}} = (0, \pi/4, 0)$. The white lines highlight the rotary resonance conditions $\omega_1^{\mathrm{max}} = \omega_{\mathrm{MAS}}$ and $\omega_1^{\mathrm{max}} = 2\,\omega_{\mathrm{MAS}}$. The superadiabatic factors were obtained numerically according to equations (4.13), (4.17) and (4.18), also considering the SA Hamiltonian in the rotating-frame. 30

4.4 Superadiabatic factor [87] contour plots for an S^3AP (WURST waveform, $\Delta\omega_1 = \omega_{\text{MAS}}$ irradiating the centerband, $\tau_p = 1$ ms) as a function of MAS rate and peak RF field strength for a single crystal using the low-power approximation up to the third-order effective Hamiltonian, transcribed from paper I. The simulations were carried out considering an SA tensor with asymmetry parameter $\eta = 0.5$ and 60 kHz (a) and 500 kHz (b) anisotropy. The chosen crystal orientation was $\Omega_{\text{PR}} = (0, \pi/4, 0)$. The white line highlight the rotary resonance condition $\omega_1^{\max} = \omega_{\text{MAS}}$. The superadiabatic factors were obtained numerically according to equations (4.13), (4.17) and (4.18), in the low-power approximation. 31

4.5 Simulated $z-$magnetization, $\cos\left[\theta^{(0)}(t)\right]$ trajectories, and frequency sweep $\omega_{\text{rf}}(t)$ for SHAPs (tanh/tan waveform, $\Delta\omega_{\text{RF}} = 5$ MHz, $t_p = 100$ μs, $\kappa = \arctan 20$) under rotary resonance conditions, with $\omega_{\text{MAS}}/2\pi = 100$ kHz and $\omega_1^{\max}/2\pi = 200$ kHz. The intervals ΔT correspond to intervals of time where the divergence between the trajectories of the magnetization and effective field is most pronounced and are given by $\Delta T = 1/22$ ms. The simulations were carried out considering an SA tensor with asymmetry parameter $\eta = 0.5$ and 60 kHz anisotropy. The chosen crystal orientation was $\Omega_{\text{PR}} = (0, \pi/4, 0)$. The trajectories and $z-$magnetization components after pulse irradiation were calculated via numeric integration of the Liouville-von Neumann equation, using the SA Hamiltonian in the rotating-frame, equation (4.2). Adapted from paper I. 32

4.6 (a) Spin-echo pulse sequences: (1) Conventional Spin-Echo and (2) double adiabatic spin-echo. The arrow indicates the time point at which the isotropic shift is refocused, and must correspond to a multiple n of rotor periods τ_r. Filled rectangles indicate pulses with a nominal flip angle of 90°, unfilled rectangles indicate a 180° pulse and unfilled rectangles with a diagonal stroke indicate adiabatic pulses. All pulses have phase x. Adapted from [11], with permission from Elsevier. (b) Experimental example of improved refocusing properties of SHAPs when applied to paramagnetic materials compared to conventional pulses: (1) ^{31}P rotor-synchronized spin-echo spectra of the cathode material $\text{LiFe}_{0.5}\text{Mn}_{0.5}\text{PO}_4$ and (2) double-SHAP-echo spectra The SHAP is a tanh/tan pulse sweeping through 5 MHz in 50 μs . The RF field amplitudes were 417 kHz for all pulses and both spectra were recorded at 11.74 T at 60 kHz MAS. Adapted from [96], with permission from Elsevier. 35

4.7 (a) The aMAT sequence where the length of the SHAP is an integer multiple m of the rotor period τ_r and with an evolution time of N rotor periods, where N is an integer that is not a multiple of 3. Filled rectangles indicate pulses with a nominal flip angle of 90°, unfilled rectangles indicate a 180° pulse. All pulses have phase x. Reprinted with permission from Clément et al. [99] (J. Am. Chem. Soc. 2012, 134, 17178-17185). Copyright 2012 American Chemical Society. (b) Experimental ^{125}Te aMAT NMR spectrum at 30 kHz MAS in magnetic field of 9.4 T. Adapted from paper A. 36

5.1 Sketches of relevant bond lengths and angles: (a) Lu[CH(SiMe$_3$)$_2$]$_3$. (b) Yb[CH(SiMe$_3$)$_2$]$_3$. The Yb–Si$_1$ distance is 3.710 Å, while Lu–Si$_1$ distance is 3.677 Å. The hydrogens of the C$_3$-C$_7$ methyl groups are not shown for simplicity. (c) DFT optimized structure of Yb[CH(SiMe$_3$)$_2$]$_3$. The carbons of C$_5$-C$_7$ and the hydrogens of the C$_3$-C$_7$ methyl groups are not shown for simplicity. The Yb–Si$_1$ distance ranges between 3.711 and 3.716 Å (see table 6 of the SI for more details). All bond lengths are reported in Åand the bond angles (in red) are reported in degrees. Transcribed from paper II. . . 38

5.2 1D NMR spectra of Yb[CH(SiMe$_3$)$_2$]$_3$: (a) ^{1}H MAS spectra at 30 kHz MAS,(b) ^{13}C MAS spectra of at 14.286 kHz MAS and (c) ^{29}Si MAS spectra at 30 kHz MAS, showing two distinct ^{29}Si signals. The spinning sidebands are marked by asterisks ($*$). 2D aMAT spectrum: (d) ^{1}H at 30 kHz, (e) ^{13}C at 20 kHz and (f)^{29}Si at 20 kHz. The indirect dimension projections were deconvolved using asymmetric Gaussian functions to extract the isotropic shifts and quantify shift dispersion. (g)-(i) extracted slices with isotropic shift corresponding to the maxima of the deconvolved projections and labelled with Roman numerals. Each slice was subsequently fitted considering a simple CSA model using the Haeberlen convention [14]. Transcribed from paper II. 42

5.3 ^{1}H-^{13}C correlation spectrum achieved by using the TEDOR experiment [124] at 30 kHz MAS, yielding two distinct correlations of the resonances (III/I) and (IV/II), as shown in figure 5.2. The spinning sidebands are marked by asterisks ($*$). Transcribed from paper II. 43

5.4 ^{1}H NMR shift distributions considering solely the contributions arising from the presence of unpaired electrons and neglecting long-range PCS effects stemming from paramagnetic centers in neighboring unit cells ($\delta_{\text{con}} + \delta_{\text{pcs}}$). The shifts were calculated considering the Moon and Patchkovski [25] and Vaara et al.[13; 26; 125] formalism using the g tensor obtained using multi-reference perturbation theory and the experimental ^{1}H hyperfine tensor. A distribution of relative orientations of the g and A tensors were considered using Zaremba, Conroy, Wolfsberg orientational averaging scheme with 1154 orientations [126–128]. The relative orientation of the z axis of the g and A tensors was kept fixed at 45°, in order to match with the EPR results. Transcribed from paper II. 44

5.5 DFT-optimized structure of Yb(CH(SiMe$_3$)$_2$)$_3$ complex overlapped with ovaloid surface representation of the ^{29}Si NMR tensors in shift convention (proximal Me$_3$Si groups colored in green/red and distal Me$_3$Si groups in blue/yellow) [131]. The radius from the center of the tensor to a point on the ovaloid surface is proportional to the chemical shift when the magnetic field is aligned along that direction in space and the sign of the shift is indicated by the color of the surface, red/yellow corresponds to positive shift and green/blue to a negative shift. Transcribed from paper II. 46

6.1 RAPT sequence for enhancing the signal from the CT of a half-integer-spin quadrupolar nucleus [139], reproduced from [11], with permission from Elsevier. The effect of ST saturation is demonstrated on the nuclear-spin energy level diagrams for a spin $I = 3/2$ in (a) where the saturation of the two STs leads to the simultaneous removal of the ST polarization and enhancement of the CT polarization. The RAPT pulse sequence is shown in (b). The saturation period with total length τ_c, comprising of a pair of pulses with flip angle β and alternating phases $+x$ and $-x$, that is repeated N times. The final pulse is a CT-selective [140], low-power pulse calibrated to deliver a 90° rotation to the CT polarization. 49

6.2 RAPT-enhanced ^{23}Na solid-state NMR spectra of NaMnO$_2$, transcribed from III. (a) One-dimensional Hahn-echo spectrum of NaMnO$_2$ with and without the application of a RAPT train illustrating the enhancement of the signal intensity of the central transition by approximately a factor of 1.4. Observed centerbands and sidebands marked with by stars ($\star$) and asterisks ($*$), respectively. (b) MAT spectrum of NaMnO$_2$ exhibiting six resonances with distinct observed shifts. Inset spectra correspond to extracted direct-dimension slices, and the observed shifts correspond to the centerbands marked by stars ($\star$). RAPT pulses were applied before the MAT experiment to enhance the signal-to-noise ratio and suppress the signals arising from the satellite transitions. Both spectra were recorded at 60 kHz MAS and at an 11.7 T external magnetic field. RAPT pulse trains were employed with a repetition frequency of 525 kHz. 50

6.3 RAPT-enhancements for the six ^{23}Na resonances extracted from the MAT spectra with increasing repetition frequency of the RAPT pulses, transcribed from paper III. The data points are indicated by red circles. The smooth black curves were obtained by employing a moving-average filter and were used to estimate the maximum enhancement factor. Considering a frequency interval corresponding to $\pm 5\%$ of the maximum enhancement factor and using equation (6.1), the range of magnitudes of the quadrupolar couplings $\left|C_q\right|$ was determined. 51

6.4 Pulse sequences and CTPs for the z-filtered STMAS, figure (a), and MQQMAS experiments, figure (b). The pulse sequence shown in (a) is used for acquiring both phase-sensitive STMAS and MQMAS spectra with different pulse parameters. The CPT for STMAS is shown in (b) and the CPT for MQMAS is given in (c). Red and black pathways correspond to the N-type and P-type datasets, respectively. Transcribed from paper IV. 53

6.5 Representation of the STMAS (a) and MQMAS (b) time-domains before and after the application of a conventional shear and scale transformation, where $k^{(t_2)}$ represents the shear ratio. The time-independent rank-0 and rank-4 terms of the second-order quadrupolar interaction along with the isotropic chemical shift that are refocused along the $C^{(0)}$, $C^{(4)}$ and p echo lines, respectively. The time domain (td) echo ridge accounting for the chemical shift anisotropy and quadrupolar interactions are shown as well. After the conventional affine transformation the interactions represented by $C^{(4)}$ are refocused along t_1'. Transcribed from paper IV. 54

6.6 Simulation of a z-filtered STMAS spectrum with rotor-synchronized indirect dimension t_1, for a system comprising three independent spins 5/2. In (a)-(c)the different echo ridges are shown for the first (solid lines) and second satellites (dashed lines). The echo CT ridge, as opposed to the satellites, lies along the p ridge. In (d)-(f) and (g)-(i) the corresponding signals are shown in the time and frequency domains, respectively. In (g)-(i) the main diagonal $\omega_1 = \omega_2$ is indicated by the dotted line. After the first shear transformation, the t_1' and ω_1' dimensions contain no shift components (p) from the first satellites and, likewise, after the second transformation, the t_2' and ω_2' dimensions contain no quadrupolar broadening ($C^{(4)}$), from the first satellites as well. In figures (j) and (k) expansions of the centerband of each spin resonance of the double sheared spectrum (i) are shown. Transcribed from paper IV. 56

6.7 (a) Sheared z -Filtered TOP-STMAS spectrum showing the CT-CT diagonal peaks of five observed resonances, around 0 kHz in the indirect dimension and the Satellite Transition (ST)-CT diagonal peak for the sites whose central transition is observed at 309 and 500 ppm, at around −2.6 kHz in the indirect dimension. Sidebands are marked with ($\star$). Extracted slices along the shift and quadrupolar dimensions together with the best fits are shown in figures (b) and (c), respectively. The spectral lineshapes were all simulated considering Gauss-Lorentz curves whose centers-of-gravity were used to determine the quadrupolar products and isotropic shifts. The STMAS spectrum was recorded while spinning at 60 kHz MAS and at 11.7 T. Transcribed from paper IV. 57

6.8 (a) ^{27}Al solid-state NMR spectrum of pristine YAG where two signals arising from the AlO_4 and the AlO_6 are clearly distinguishable. (b) z-Filtered TOP-STMAS spectrum indicating the CT-ST_1 correlation cross-peak and the CT-CT diagonal peak, of lower intensity. In (c) the extracted slice is shown together with the best fit chemical shift and quadrupolar interaction parameters determined experimentally. Both spectra were acquired at 14.1 T and 60 kHz MAS. Adapted from paper IV. . 58

6.9 (a) Nd:YAG and (b) Eu:YAG ^{27}Al NMR spectrum. Shifted resonances arising from the presence of one and two Ln ions in the first Ln-Y coordination shell are denoted with (1 Nd/Eu) and (2 Nd/Eu), respectively. (c) and (d) Sheared z-filtered TOP-STMAS ^{27}Al spectra together with extracted slices and best fits of the quadrupolar dimension (e)-(f) of Nd and Eu, respectively. The shifted Eu:YAG was fitted with an additional Gaussian lineshape to account for the contributions from the CT autocorrelation that affects the quadrupolar lineshape. All spectra were acquired at 14.1 T, 60 kHz spinning speed. Transcribed from paper IV. . . . 60

6.10 (a) Nd:YAG and (b) Eu:YAG ^{27}Al NMR spectrum. Shifted resonances arising from the presence of one and two Yb ions in the first Yb-Y coordination shell are denoted with (1 Yb) and (2 Yb), respectively. (c) and (d) z-filtered TOP-STMAS ^{27}Al spectra together with extracted slices and best fits of the quadrupolar dimension (e)-(f) of Tb and Yb, respectively. Horizontal dotted line in (c) and (d) correspond to slices extracted of the shift. The shifted Tb:YAG was fitted with an additional Gaussian lineshape to account for the contributions from the CT autocorrelation that affects the quadrupolar lineshape. All spectra were acquired at 14.1 T, 60 kHz spinning speed. Transcribed from paper IV. 61

List of Tables

2.1 Rank-0, 2 and 1 contributions correspond to the isotropic shielding constant and anisotropic symmetric as well as anisotropic antisymmetric terms, respectively. $\varepsilon\tau$ corresponds to the Cartesian components of pNMR shielding tensor and S electron spin quantum number. 13

4.1 Amplitude $\omega_1(t)$, phase $\phi_{\mathrm{pul}}(t)$ and sweep of the transmitter offset, $\omega_{\mathrm{RF}}(t) = \mathrm{d}\phi_{\mathrm{pul}}(t)/\mathrm{d}t$, for the Hyperbolic secant, tanh/tan and WURST frequency-swept adiabatic pulses. ω_1^{max} is the maximum value of RF amplitude, τ_p is the pulse duration, $\Delta\omega_1$ the sweep width. For the hyperbolic secant, $\beta = \mathrm{sech}^{-1}(f)$ and f corresponds to the fraction of ω_1^{max} at which the beginning and end of the amplitude profile are truncated. For the tanh/tan ξ and κ are dimensionless parameters that control the rate at which the amplitude profile reaches ω_1^{max} and the steepness of the sweep of the transmitter offset, respectively. For the WURST n is a factor that modifies the rate at which the amplitude profile is smoothed from zero to ω_1^{max}. 23

5.1 Comparison of experimental and calculated g tensor (g_x, g_y and g_z represent the components of g tensor in the PAF) and magnetic properties of $\mathrm{Yb[CH(SiMe_3)_2]_3}$ complex. Calculated values were obtained using multi-reference perturbation theory (CASSCF/NEVPT2). Experimental values were obtained via EPR characterization and magnetic measurements. Transcribed from paper II. 40

5.2 Calculated and experimental SA parameters for the proximal (Me_3Si_2) and distal (Me_3Si_1) Me_3Si groups of $Yb[CH(SiMe_3)_2]_3$ in the Haeberlen convention [14] (experimental spectra are shown in 5.2). The calculated SAs were decomposed according to equations 2.52 and 2.40 of chapter 2. Hyperfine tensor calculated at SCS-MP2 and PBE0 level of theory, orbital chemical shifts with TPSS meta-GGA functional and g tensor with multi-reference perturbation theory (CASSCF+NEVPT2). ^{13}C and ^{1}H tensors of Me_3Si groups were averaged both within the methyl groups (along the Si-C_i bonds) and the Me_3Si groups (along the C_1-Si bond). Isotropic shifts were averaged between the three different $SiMe_3$ groups, which due to small deviations of C_3 symmetry in the optimized geometry result in different SA tensors. These deviations also account for the range of anisotropies $\Delta\delta$ and asymmetry η parameters. Adapted from paper II. . . . 45

6.1 Extracted experimental ^{27}Al isotropic shift and quadrupolar interaction parameters of the four coordinated sites in both undoped and Ln doped YAGs. The isotropic shift and quadrupolar interaction parameters for the undoped YAG reported in Florian et al. [154] and Vosegaard et al.[155] were also included for comparison. Adapted from paper IV. 59

1

Introduction

Over the last decades, solid-state Nuclear Magnetic Resonance (ssNMR) has stepped out of the shadow of its liquid-state counterpart and has risen to become a routinely applied tool to study a wide range of materials in the fields of chemistry, physics, materials science and biology [1–9]. Historically, the main limitation of ssNMR had been the poor resolution due to the presence of large anisotropic interactions, which generally vanish in the liquid-state. However, these interactions, more specifically the chemical shift anisotropy (CSA), dipole-dipole coupling and quadrupolar coupling, also provide quantitative information on molecular structure, conformation and dynamics [10]. The recent advances in both pulse sequence design and probe technology, particularly the advent of Magic-Angle-Spinning (MAS), have equipped an NMR spectroscopist with the ability to not only “switch on” or “switch off” these interactions but also to correlate them [10].

The application of these developments to paramagnetic systems, that is molecules or materials that contain one or more “paramagnetic centers” *i.e.* atoms or ions possessing at least one unpaired electron, despite recent progress, has lagged behind. This is due to the fact that the hyperfine interaction between the unpaired electrons and the observed nucleus induces a very large shifts and shift anisotropies, dramatic nuclear paramagnetic relaxation enhancements (PRE) and additional sources of broadening arising due to bulk magnetic susceptibility effects (BMS)[11]. In solids, this can potentially result in extremely broad NMR spectra spanning thousands of ppm with low resolution. Nevertheless, this interaction contains important information regarding the system’s electronic and magnetic structure, the nature of the bonding between the atoms and their local environment and the delocalisation of the unpaired electrons onto the coordinating atoms and ligands.

Paramagnetic systems are key constituents of a broad range of versatile materials with important applications in the field of catalysis, energy storage and conversion, nanodevices and Magnetic Resonance Imaging (MRI) contrast agents and, hence, addressing the current limitations of ssNMR for studying these systems is of overriding importance. In this context, the work I have carried out during my PhD had three main objectives, firstly the improvement of the excitation and manipulation of the very broad signal components due to the large anisotropic spin interactions via a thorough theoretical and experimental investigation of alternative radiofrequency (RF) irradiation schemes with increased bandwidth for spin population inversion based on frequency-swept adiabatic pulses. Secondly, the computation and interpretation of paramagnetic NMR (PNMR) shifts in an ytterbium alkyl compound, rationalizing its structure and electronic properties. Lastly, the development of methods that are suitable for half-integer quadrupolar (half-integer spin $I > 1/2$) nuclei in paramagnetic systems, where the acquisition and interpretation of NMR spectra is further complicated due to the presence of a moderate-to-large quadrupolar interaction in conjunction with the hyperfine interaction.

This document is structured as follows: in chapter 2 we start with a brief overview of the quantum mechanical framework to describe Nuclear Magnetic Resonance with particular emphasis on the chemical shielding and quadrupolar interactions. We will give a brief review of the underlying physics behind the the major observable effects in paramagnetic systems, such as the contact and pseudo-contact shifts, paramagnetic relaxation enhancement and BMS effects. In chapter 3 we give a survey of the computational methods used to predict the NMR spectra. Chapters 4 to 6 outline the main work I have carried out during my Ph.D. studies. Chapter 4 provides an unifying description the underlying theory of frequency-swept pulses applied to spinning solids in different power regimes, based on paper I. Chapter 5 details the work carried out on a paramagnetic organoytterbium complex, focusing on its characterization via quantum-chemical calculations, based on paper II. Lastly, chapter 6 summarizes the work I have done on half-integer-spin quadrupolar nuclei in magic-angle spinning paramagnetic NMR, based on papers III and IV. A brief summary and conclusion is then given in chapter 7.

2

NMR of Paramagnetic Solids: Theoretical Background

In a quantum mechanical framework, objects that possess an intrinsic spin, **I**, defined by the spin quantum number, I, which corresponds to a quantised form of angular momentum, have non-zero magnetic dipole moment, $\hat{\mu}_I$, given by the expression:

$$\hat{\mu}_I = \hbar\gamma_I\hat{I}, \tag{2.1}$$

where $\hbar$ is the reduced Planck's constant and γ_I the nuclear gyromagnetic ratio. It is important to note that there exist $2I+1$ spin states, each defined by a magnetic quantum number m_I, such that $m_I = -I, -I+1, \ldots +I$. For nuclei with intrinsic spin, in the absence of both internal interactions with the electronic cloud or surrounding nuclei and external interactions with a magnetic field, these energy levels are degenerate.

In nuclear magnetic resonance, an external magnetic field $\mathbf{B}_0$, conventionally applied along the z direction, interacts with the nuclear magnetic moment. This interaction is governed by the nuclear Zeeman Hamiltonian, which defines the frequencies of transitions between its eigenstates $|m_i\rangle$ and $|m_j\rangle$, represented in Dirac notation, and can be expressed as

$$\hat{H}_{IZ} = -\gamma_I\mathbf{B}_0\hat{I}, \tag{2.2}$$

in frequency units. This Hamiltonian, however, does not account for internal interactions, which generate additional local perturbations to the magnetic field experienced by the nuclear spin, and, hence, is only valid for an isolated nucleus. Generally these interactions can be summarized as: the chemical shift interaction between the nucleus and the surrounding electron shell, scalar through-bond J-coupling and dipolar through-space interactions between two nuclear spins, interaction between the electric nuclear quadrupole moment (only existent for $I > 1/2$) and the local electric field gradient (EFG), and the hyperfine interaction between nuclear spin and neighboring unpaired electrons. In the context of paramagnetic solids the dominating interactions are the quadrupolar, chemical shift and hyperfine interactions and, therefore, are the main focus of this work. In this chapter we will provide a brief overview of the theory of these interactions.

2.1 Chemical Shift Interaction

The application of an external magnetic field causes the electrons surrounding the nucleus to move in a way that generates an induced external magnetic field, which in turn modifies the field experienced by the nucleus. This effect can be included in the Zeeman Hamiltonian as follows:

$$\begin{aligned} \hat{H} &= \hat{H}_Z + \hat{H}_C \qquad (2.3) \\ &= -\gamma_I \mathbf{B}_0 \cdot (\mathbb{1} - \sigma) \cdot \hat{I}, \qquad (2.4) \end{aligned}$$

where $\hat{H}_C = \hbar\gamma_I \mathbf{B}_0 \cdot \sigma \cdot \hat{I}$, is the Hamiltonian describing the chemical shielding and $\mathbb{1}$ is the identity operator. The shielding tensor was originally described by Ramsey [12], who also showed that it can be broken down in the contributions arising from the electronic ground state σ^{dia}, and σ^{par} due to the mixing of excited states. The sum of these two terms is routinely referred to the orbital contribution to the shielding σ^{orb} [13]. In paramagnetic systems an additional contribution, σ^{S}, arising from the presence of unpaired electrons must be added to give the total shielding tensor

$$\sigma = \sigma^{\text{orb}} + \sigma^{\text{S}}. \qquad (2.5)$$

The principal components of the shielding tensor $\tilde{\sigma}_{xx}$, $\tilde{\sigma}_{yy}$, and $\tilde{\sigma}_{zz}$ in its principal axis frame (PAF) are typically expressed in terms of isotropic shielding σ_{iso}, anisotropy $\Delta\sigma$ and asymmetry η, defined as:

$$\begin{aligned} \sigma_{\text{iso}} &= \frac{1}{3}\left(\tilde{\sigma}_{xx} + \tilde{\sigma}_{yy} + \tilde{\sigma}_{zz}\right), \qquad (2.6) \\ \Delta\sigma &= \tilde{\sigma}_{\text{zz}} - \sigma_{\text{iso}}, \qquad (2.7) \\ \eta &= \frac{\tilde{\sigma}_{yy} - \tilde{\sigma}_{xx}}{\Delta\sigma}, \qquad (2.8) \end{aligned}$$

and ordered according to the Haeberlen convention [14] $|\tilde{\sigma}_{zz} - \sigma_{\text{iso}}| \geq |\tilde{\sigma}_{xx} - \sigma_{\text{iso}}| \geq |\tilde{\sigma}_{yy} - \sigma_{\text{iso}}|$

Under high-field conditions, the Zeeman interaction dominates over the chemical shielding which means the latter can be treated as perturbation. The first-order truncated average Hamiltonian in the reference frame rotating at the Larmor frequency (commonly referred to as the rotating frame)[15; 16] is given by

$$\begin{aligned} \bar{H}_C^{(1)} &= -\omega_0 \sigma^{(1)} \hat{I}_z, \qquad (2.9) \\ \sigma^{(1)} &= -\sqrt{\frac{1}{3}}\sigma_{00} + \sqrt{\frac{2}{3}}\sigma_{20}, \qquad (2.10) \end{aligned}$$

where σ_{00} and σ_{20} are spherical tensors of rank 0 and 2, respectively, which can be simplified as

$$\sigma_{00} = -\sqrt{3}\sigma_{\text{iso}}, \tag{2.11}$$

$$\sigma_{2m} = \sum_{m'=-2}^{+2} \tilde{\sigma}_{2m'} D^{(2)}_{m'm}(\Omega_{\text{PL}}) \tag{2.12}$$

where

$$\tilde{\sigma}_{20} = \sqrt{\frac{3}{2}}\Delta\sigma, \tag{2.13}$$

$$\tilde{\sigma}_{2\pm1} = 0, \tag{2.14}$$

$$\tilde{\sigma}_{2\pm2} = -\frac{1}{2}\eta\Delta\sigma, \tag{2.15}$$

and $\Omega_{\text{PL}} = (\alpha_{\text{PL}}, \beta_{\text{PL}}, \gamma_{\text{PL}})$ represents the set of Euler angles that define the orientation of the PAF of the shielding tensor in the laboratory frame, and $D^{(2)}_{mm'}(\Omega)$ are the elements of the Wigner rotation matrices of rank 2 [17]. Up until this point we based our discussion of the chemical shift interaction in terms of chemical shielding, however, in experimental NMR we measure the chemical shift tensor δ, with isotropic value given by

$$\delta_{\text{iso}} = \sigma^{\text{ref}}_{\text{iso}} - \sigma_{\text{iso}}, \tag{2.16}$$

where $\sigma^{\text{ref}}_{\text{iso}}$ is the isotropic shielding of a reference system. Using this convention we can write the CSA, $\Delta\delta$, and asymmetry parameter η as

$$\Delta\delta = \tilde{\delta}_{zz} - \delta_{\text{iso}}, \tag{2.17}$$

$$\eta = \frac{\tilde{\delta}_{yy} - \tilde{\delta}_{xx}}{\Delta\delta}, \tag{2.18}$$

where, once again, we used the Haeberlen convention [14] to order the principal values of the tensor, $\tilde{\delta}_{ii}$, in PAF $|\tilde{\delta}_{zz} - \delta_{\text{iso}}| \geq |\tilde{\delta}_{xx} - \delta_{\text{iso}}| \geq |\tilde{\delta}_{yy} - \delta_{\text{iso}}|$. It is important to note that, in the context of paramagnetic systems, the CSA is typically generalized to shift anisotropy (SA) to include possible contributions of the unpaired electrons.

2.2 Quadrupolar Interaction

Nuclei with spin $I > 1/2$ exhibit a quadrupolar moment which couples with the EFG due to the surrounding electrons, giving rise to the quadrupolar interaction. The EFG is derived from the electric potential of the electrons V by taking the second derivative with respect to the position coordinates x_i

$$V_{ij} = \frac{\partial^2 V}{\partial x_i \partial x_j}. \tag{2.19}$$

Since the charge distribution generating the electrostatic potential is external to the nucleus, according to Laplace's equation $\boldsymbol{\nabla}^2 V(\mathbf{r}) = 0$, and therefore, the EFG tensor must be traceless. In its PAF, the tensor is diagonal with principal components $\tilde{V}_{ii}$, ordered as $|\tilde{V}_{zz}| \geq |\tilde{V}_{yy}| \geq |\tilde{V}_{xx}|$ and similarly to SA tensor can be written in terms of the EFG anisotropy, eq, and asymmetry η^Q parameters

$$\tilde{V}_{zz} = eq, \tag{2.20}$$

$$\eta^Q = \frac{\tilde{V}_{xx} - \tilde{V}_{yy}}{\tilde{V}_{zz}}. \tag{2.21}$$

The basic form of the Hamiltonian describing this interaction is given by

$$\hat{H}_Q = \frac{eQ}{2I(2I-1)\hbar} \hat{I} \cdot \hat{V} \cdot \hat{I}, \tag{2.22}$$

where eQ is the nuclear quadrupole moment. The Hamiltonian can also be written as

$$\hat{H}_Q = \frac{2}{3} \omega_Q \hat{I} \cdot \upsilon \cdot \hat{I}, \tag{2.23}$$

where we defined the reduced EFG tensor as $\upsilon = V/(eq)$, and the quadrupolar coupling constant C_q and quadrupolar splitting frequency ω_Q as

$$C_q = \frac{e^2 qQ}{h}, \tag{2.24}$$

$$\omega_q = \frac{3\pi C_q}{2I(I-1)}. \tag{2.25}$$

The first-order truncated average Hamiltonian is given by

$$\bar{H}_Q^{(1)} = \sqrt{\frac{2}{3}} \omega_q \sum_{m=-2}^{m=2} \tilde{\upsilon}_{2,m} D_{m0}^{(2)}(\Omega_{\mathrm{QL}}) \left[\hat{I}_z^2 - \frac{1}{3} I(I+1) \mathbb{1} \right], \tag{2.26}$$

where $\Omega_{\mathrm{QL}} = (\alpha_{\mathrm{QL}}, \beta_{\mathrm{QL}}, \gamma_{\mathrm{QL}})$ are the set of Euler angles defining the orientation of the PAF of the EFG tensor relative to the laboratory frame, and $\tilde{\upsilon}_{2,m}$ is the reduced EFG tensor expressed in terms of the irreducible spherical tensor components in the PAF, given by:

$$\tilde{\upsilon}_{2,0} = \sqrt{\frac{3}{2}}, \tag{2.27}$$

$$\tilde{\upsilon}_{2,\pm 1} = 0, \tag{2.28}$$

$$\tilde{\upsilon}_{2,\pm 2} = \frac{1}{2} \eta^Q. \tag{2.29}$$

$$\tag{2.30}$$

Typically, under high-field conditions while the quadrupolar interaction can still be treated as a perturbation, its magnitude may be large enough to justify the inclusion second order term arising solely due to quadrupole interaction. This Hamiltonian is given by

$$\begin{aligned}\bar{H}_Q^{(2)} =&\frac{4\omega_q^2}{9\omega_0}\left\{W_{00}^Q\left[\frac{3}{5\sqrt{5}}\left(5\hat{I}_z^3-(3I(I+1)-1)\hat{I}_z\right)+\frac{4I(I+1)-3}{5\sqrt{5}}\hat{I}_z\right]\right.\\ &W_{20}^Q\left[-\frac{3}{5}\sqrt{\frac{2}{7}}\left(5\hat{I}_z^3-(3I(I+1)-1)\hat{I}_z\right)+\frac{4I(I+1)-3}{10\sqrt{14}}\hat{I}_z\right]\\ &\left.W_{40}^Q\left[-\frac{51}{15}\sqrt{\frac{1}{70}}\left(5\hat{I}_z^3-(3I(I+1)-1)\hat{I}_z\right)-\frac{12I(I+1)-9}{10\sqrt{70}}\hat{I}_z\right]\right\},\end{aligned} \tag{2.31}$$

where we defined the spatial properties of this interaction in terms of the following irreducible spherical tensors W_{l0}^Q in the coupled representation

$$W_{l0}^Q = \sum_m \langle 22m-m|L0\rangle\, \upsilon_{2m}\upsilon_{2-m}, \tag{2.32}$$

where υ_{ij} are the spherical tensor components of the the reduced EFG tensor.

It is important to note that similarly to basic form of the quadrupolar Hamiltonian, the first order term is also proportional to the quadrupolar splitting frequency. The second order term scales with ω_q^2/ω_0, which means it becomes less important as external magnetic field increases. Additionally, we also note that this term has spatial interactions of rank 0, *i.e* spatially isotropic, and of both ranks 2 and 4.

2.3 Magic-angle Spinning

In solution NMR, all the anisotropic components of the interactions described in the previous section are averaged to zero by the fast tumbling of molecules on the NMR timescale. As a result, narrow peaks are routinely acquired, as shown in figure 2.1(a). In a poly-crystalline powder, each crystallite orientation gives rise to a sharp peak at a particular frequency. Assuming that we have a statistical random distribution of crystallite orientations, these peaks combine to give a broad resonance, referred to as powder pattern, as shown in figure 2.1(b), which precludes the acquisition of high-resolution solid-state NMR spectra. The rank-2 induced orientation dependent broadening of the resonances can be removed by mechanically spinning the samples at 54.57°, which mimics the fast motion that molecules undergo in solution [18–20]. In figure 2.1(c) we illustrate the effect of MAS. It is important to point out that only if the MAS rate exceeds the magnitude of these anisotropic interactions, total coherent averaging is achieved, and only the isotropic frequencies remain in the spectra. Typically, the spinning speed is smaller than the span of frequencies in stationary conditions arising due to the anisotropic interactions, and, therefore, the effect of MAS is to split the resonances into narrower bands, referred to as spinning sidebands, with the same phase, and separated by the spinning frequency. This results in substantial improvements in resolution and signal to noise ratio, by concentrating the signal intensity in the sidebands.

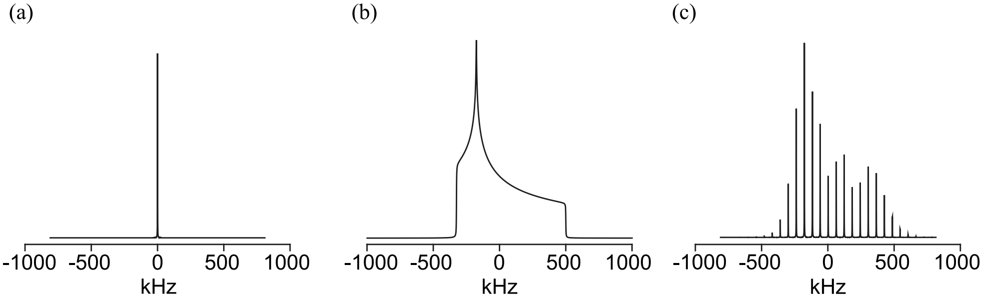

Figure 2.1: Simulated spectra of a paramagnetic system subject to a shielding interaction. The high-resolution, isotropic solution spectrum is shown in (a), exhibiting a single peak at the isotropic offset. A powder sample in the solid-state gives the classic CSA powder pattern in (b), which splits into a series of spinning sidebands under MAS, as shown in (c). The chemical shielding parameters are $-\omega_0\Delta\sigma/2\pi = 500$ kHz, and $\eta = 0.3$, and the frequency is measured relative to the isotropic offset Ω_{iso}. Adapted from [11], with permission from Elsevier.

2.3.1 Spinning Sidebands

As a result of the mechanical rotation of the rotor, the set of Euler angles that define the orientation of the rotor frame relative to the laboratory frame are time-dependent. Considering that the spinning axis is at a fixed angle θ_{RL} relative to the external field, and the rotor spins at frequency ω_{MAS} from an initial position $\alpha_{\text{RL}}(0)$, the set of Euler angles is defined as $\Omega_{\text{RL}}(t) = [-\omega_{\text{MAS}}t, \theta_{\text{M}}, 0]$. The shift Hamiltonian in the rotating frame can then be written (in frequency units) as:

$$\hat{H}_C = \sum_{l=-2}^{+2} \omega_c^{(l)}(\gamma_{\text{PR}}) \exp\{(-il\omega_{\text{MAS}}t)\}\hat{I}_z, \tag{2.33}$$

where $\omega_c^{(l)}(\gamma_{\text{PR}})$ coefficients are given by:

$$\omega_c^{(l)}(\gamma_{\text{PR}}) = -\omega_0\sigma_{\text{iso}}\delta_{l0} - \sqrt{\frac{2}{3}} \sum_{k=-2}^{+2} \tilde{\sigma}_{2k} D_{kl}^{(2)}(\alpha_{\text{PR}}, \beta_{\text{PR}}, \gamma_{\text{PR}}) D_{l0}^{(2)}(0, \theta_{\text{M}}, 0), \tag{2.34}$$

where δ_{l0} is the Kronecker delta and $\Omega_{\text{PR}} = (\alpha_{\text{PR}}, \beta_{\text{PR}}, \gamma_{\text{PR}})$ represents the set of Euler angles that relate the PAF of the of the shielding tensor to the rotor-fixed frame. The first term in equation 2.34 is isotropic, time-independent and, hence, the same for all crystallites, while second term accounts for the anisotropic frequencies which are time-dependent and periodic over the rotor period, giving rise to the spinning sideband manifold.

2.3.2 Quadrupolar Nuclei under MAS

In static conditions, the distribution of crystallite orientations affected by the quadrupolar interaction will also give rise to a broad powder pattern, as shown in figure 2.3. As an example, let us consider a spin $I = 3/2$ system. There are three observable transitions, the outer satellite transitions (STs), $|3/2+1/2\rangle\langle 3/2+3/2|$ and $|3/2-3/2\rangle\langle 3/2+1/2|$ in $|Im_I\rangle$ Dirac notation, and the symmetric central transition (CT) $|3/2-1/2\rangle\langle 3/2+1/2|$. The first-order quadropolar interaction is a rank-two spatial interaction similar to the SA, but dependent on $\hat{I}_z^2$ (see equation 2.26). As a result, the satellite transitions evolve under first order interaction with symmetric frequencies, which combines to give rise to a Pake pattern [21], while the CT does not evolve, giving rise to a sharp peak at zero frequency (see figures 2.2(a)-(c)). Similarly to SA, under MAS conditions the two satellite transitions give rise to two periodic contributions that each split into a spinning sideband manifold, whose centrebands are coincident with each other and with the CT peak (see figure 2.2(d)-(e)).

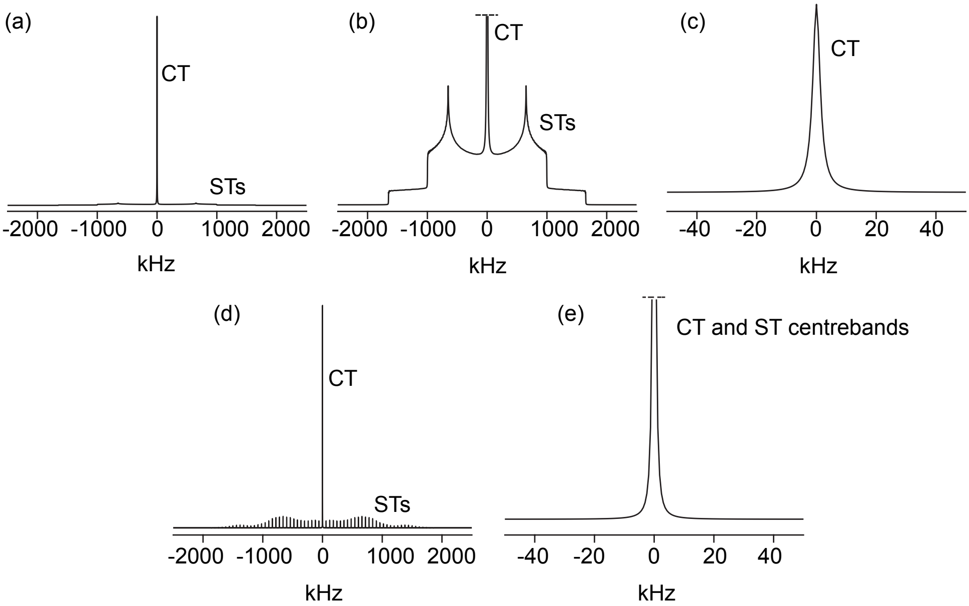

Figure 2.2: Simulated powder spectra of a spin $I = 3/2$ nucleus subject to a first-order quadrupolar interaction: (a) Static spectrum. (b) and (c) Expansions of (a) to highlight the broad ST resonances and the CT, respectively. (d) MAS spectra at 60 kHz spinning speed. (e) Expansion of (d) to highlight the CT resonance. The quadrupolar interaction parameters are C_Q = 3.3 MHz (corresponding to $\omega_q/2\pi$ = 825 kHz), η_Q = 0.21. The nuclear Larmor frequency is $\omega_0/2\pi = -105.9$ MHz. Adapted from [11], with permission from Elsevier.

As shown in equation 2.31 the inclusion of the second-order quadrupolar interaction, introduces an additional isotropic term of rank-zero, a rank-2 and a rank-4 term. All three contributions are spin transition dependent, and, as a result, differ for the STs and the CT. The effect of these contributions is highlighted in figure 4.1. For a static powder, the inclusion of the second-order quadrupolar induces a negligible change in the ST resonances, due to the fact that the first-order quadrupolar interaction is the dominant contribution to the broadening. For the CT, since it is unaffected by the first-order quadrupolar, the rank-two and rank-4 terms introduced by the second-order interaction broaden the lineshape, reducing its apparent intensity, and the rank-0 term shifts the center-of-gravity of the lineshape from zero frequency.

Under MAS conditions, while the rank-two broadening is removed, the fourth rank broadening is only scaled down by a factor of $-7/18$ which also reverses the lineshape relative to the zero frequency. Furthermore, it is also reveals that the centerbands of the CT and STs no longer appear at the isotropic position, due to the fact that isotropic term differs. This effect is commonly referred to as the quadrupolar induced shift defined as

$$\delta_{\mathrm{QIS}} = A^0(I,q)\delta_q, \tag{2.35}$$

$$\delta_q = \left[\frac{3}{4I(2I+1)}\right]^2 \frac{P_q^2}{\nu_0}, \tag{2.36}$$

where ν_0 is the Larmor frequency in Hz, $A(I,q)$ is a spin (I) and transition (q) dependent coefficient [22], which for spin $3/2$ corresponds to $-2/5$ and $4/5$ for the CT and ST respectively, and P_q is the quadrupolar product defined as

$$P_q = C_q\sqrt{1+\frac{\eta_q^2}{3}}. \tag{2.37}$$

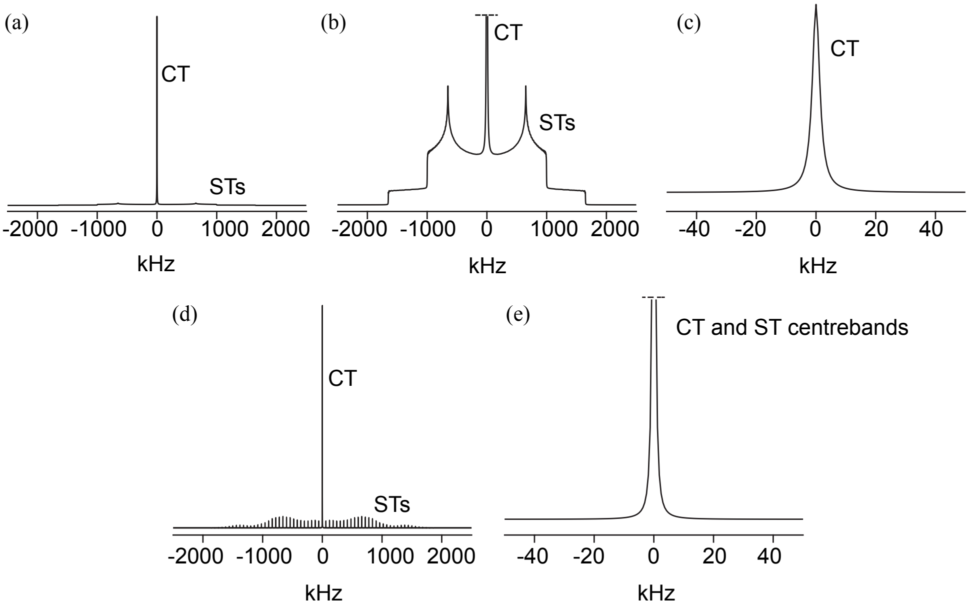

Figure 2.3: Simulated powder spectra of a spin $I = 3/2$ nucleus subject to a first- and second order quadrupolar interaction: (a) Static spectrum. (b) and (c) Expansions of (a) to highlight the broad ST resonances and the CT, respectively. (d) MAS spectra at 60 kHz spinning speed. (e) Expansion of (d) to highlight the CT resonance. The quadrupolar interaction parameters are C_Q = 3.3 MHz (corresponding to $\omega_q/2\pi$ = 825 kHz), η_Q = 0.21. The nuclear Larmor frequency is $\omega_0/2\pi = -105.9$ MHz. Adapted from [11], with permission from Elsevier.

2.4 Paramagnetic effects in solid-state NMR

So far we have not explicitly included the coupling interaction between the nucleus and the unpaired electron, which is crucial to describe NMR of paramagnetic systems. Furthermore, we must consider the presence of electron orbital angular momenta and the presence of spin-orbit coupling. Provided the orbital excited states are sufficiently far in energy from the ground state, the total electron magnetic moment $\hat{\mu}$ can be written in the form

$$\hat{\mu} = \mu_B \mathbf{g} \cdot \hat{S}, \tag{2.38}$$

where **g** tensor is associated with the ground-state multiplet taking into account the spin-orbit coupling [23], μ_B is the Bohr magneton, and $\hat{S}$ the effective electron spin operator. Electrons change their spin state much faster than the nuclei, which consequentially causes the NMR shift to depend on the interaction of the nuclear magnetic moment with a thermally averaged electron magnetic moment, calculated from the population distribution over energy levels at a given temperature. The relevant interactions can be parameterized by the standard Electron

Paramagnetic Resonance (EPR) Hamiltonian defined as

$$\hat{H}^{\text{epr}} = \hat{S}^T \cdot \mathbf{D} \cdot \hat{S} + \frac{\mu_B}{\hbar}\mathbf{B}_0^T \cdot \mathbf{g} \cdot \hat{S} + \hat{S}^T \cdot \mathbf{A} \cdot \hat{I}, \tag{2.39}$$

where D corresponds to Zero Field Splitting (ZFS) and $\hat{A}$ to the hyperfine coupling tensor. For simplicity we excluded the contribution of the orbital shielding tensor. The paramagnetic contributions can be obtained by re-deriving the Kurland-McGarvey theory of paramagnetic shifts in terms of EPR property tensors [24–26], which leads to the following formula:

$$\sigma^S = -\frac{\mu_B}{\hbar\gamma_I k_B T}\mathbf{g} \cdot \langle SS^T \rangle \cdot \mathbf{A}, \tag{2.40}$$

where k_B is the Boltzmann constant, and the term $\langle SS^T \rangle$ is the spin dyadic, which is a thermal average over all populated electronic Zeeman states and indirectly accounts for the presence of the zero-field splitting tensor since it gives rise to the splittings of the energy levels at zero field and zero nuclear magnetic moment. The spin dyadic takes the form:

$$\langle S_a S_b \rangle = \frac{\sum_{nm} Q_{nm} \langle n|S_a|m\rangle \langle m|S_b|n\rangle}{\sum_n \exp\left(-\frac{E_n}{k_B T}\right)},\ a,\ b=\{x,y,z\} \tag{2.41}$$

$$Q_{nm} = \begin{cases} \exp\left(-\frac{E_n}{k_B T}\right) & E_n = E_m, \\ -\frac{k_B T}{E_m - E_n}\left[\exp\left(-\frac{E_m}{k_B T} - \frac{E_n}{k_B T}\right)\right] & E_n \neq E_m, \end{cases} \tag{2.42}$$

where E_m and E_n are the energy of the states $|m\rangle$ and $|n\rangle$. The $\mathbf{g}$ and $\mathbf{A}$ tensors can be decomposed in three and five terms, respectively:

$$\mathbf{g} = (g_e + \Delta g_{\text{iso}})\mathbb{1} + \Delta\tilde{\mathbf{g}}, \tag{2.43}$$

$$\mathbf{A} = (A^{\text{FC}} + A^{\text{PC}})\mathbb{1} + \mathbf{A}^{\text{SD}} + \mathbf{A}^{\text{dip},2} + \mathbf{A}^{\text{as}}, \tag{2.44}$$

where $\mathbf{g}$ encompasses the free electron g_e factor and the g shift tensor $\Delta\mathbf{g} = \mathbf{g} - g_e\mathbb{1}$, with isotropic and anisotropic parts given by $\Delta\mathbf{g}_{\text{iso}}$ and $\Delta\tilde{\mathbf{g}}$, respectively. The hyperfine coupling tensor $\mathbf{A}$ was decomposed in the non-relativistic Fermi contact $A^{\text{FC}}\mathbb{1}$, spin dipolar $\mathbf{A}^{\text{SD}}$ terms, and relativistic spin-orbit terms $A^{\text{PC}}\mathbb{1} + \mathbf{A}^{\text{dip},2} + \mathbf{A}^{\text{as}}$. The combination of these terms truncated at $\mathcal{O}(\alpha^4)$ results in nines terms summarized in table 2.1,

				Tensorial Rank	
Term in $\sigma_{\varepsilon\tau}$	Number	Symbol	Order	$S = 1/2$	$S > 1/2$
$g_e A^{\mathrm{FC}}\langle S_\varepsilon S_\tau\rangle$	1	σ_{con}	$\mathcal{O}(\alpha^2)$	0	$0,2$
$g_e \sum_b A^{\mathrm{SD}}_{b\tau}\langle S_\varepsilon S_b\rangle$	2	σ_{dip}	$\mathcal{O}(\alpha^2)$	2	$0,2,1$
$g_e A^{\mathrm{PC}}\langle S_\varepsilon S_\tau\rangle$	3	$\sigma_{\mathrm{con,2}}$	$\mathcal{O}(\alpha^4)$	0	$0,2$
$g_e \sum_b A^{\mathrm{dip,2}}_{b\tau}\langle S_\varepsilon S_b\rangle$	4	$\sigma_{\mathrm{dip,2}}$	$\mathcal{O}(\alpha^4)$	0	$0,2,1$
$g_e \sum_b A^{\mathrm{as}}_{b\tau}\langle S_\varepsilon S_b\rangle$	5	σ_{as}	$\mathcal{O}(\alpha^4)$	1	$2,1$
$\Delta g_{\mathrm{iso}} A^{\mathrm{FC}}\langle S_\varepsilon S_\tau\rangle$	6	$\sigma_{\mathrm{con,3}}$	$\mathcal{O}(\alpha^4)$	0	$0,2$
$\Delta g_{\mathrm{iso}} \sum_b A^{\mathrm{SD}}_{b\tau}\langle S_\varepsilon S_b\rangle$	7	$\sigma_{\mathrm{dip,3}}$	$\mathcal{O}(\alpha^4)$	2	$0,2,1$
$A^{\mathrm{FC}} \sum_a \Delta\tilde{\mathbf{g}}_{\varepsilon a}\langle S_a S_\tau\rangle$	8	$\sigma_{\mathrm{c,aniso}}$	$\mathcal{O}(\alpha^4)$	$2,1$	$0,2,1$
$\sum_{ab} \Delta\tilde{\mathbf{g}}_{\varepsilon a} A^{\mathrm{SD}}_{b\tau}\langle S_a S_\tau\rangle$	9	σ_{pc}	$\mathcal{O}(\alpha^4)$	$0,2,1$	$0,2,1$

Table 2.1: Rank-0, 2 and 1 contributions correspond to the isotropic shielding constant and anisotropic symmetric as well as anisotropic antisymmetric terms, respectively. $\varepsilon\tau$ corresponds to the Cartesian components of pNMR shielding tensor and S electron spin quantum number.

The leading terms of $\mathbf{A}$ are the non-relativistic contributions given by:

$$\mathbf{A}^{\mathrm{SD}} = \frac{\mu_0}{4\pi}\gamma_I \mu_B g_e \int \frac{3\mathbf{rr} - r^2\mathbb{1}}{r^5}\frac{\rho(r)}{2S} d^3r, \tag{2.45}$$

$$A^{\mathrm{FC}} = \frac{\mu_0}{3}\gamma_I \mu_B g_E \frac{\rho_I}{S} \tag{2.46}$$

where r is the position vector relative to the NMR nucleus and $\rho(\mathbf{r})$ is the electron spin density distribution, ρ_I is the contact spin density at the nuclear position , and S the electron spin quantum number. For nuclei far from the paramagnetic center, the point-dipole approximation applies and the spin-dipolar hyperfine coupling can be expressed as

$$\mathbf{A}^{\mathrm{SD}} \approx -\frac{\mu_0 \mu_B^2}{k_B T}\frac{\gamma_I \mu_B}{r^3} g_e \left(\frac{3\mathbf{rr}^T}{r^2} - \mathbb{1}\right). \tag{2.47}$$

Using this approximation, a a long-range pseudo-contact contribution to the shielding tensor, $\sigma^{\mathrm{pcs,lr}}$, can be derived using equation 2.40,

$$\sigma^{\mathrm{pcs,lr}} \approx -\frac{1}{4\pi r^3}\chi' \left(\frac{3\mathbf{rr}^T}{r^2} - \mathbb{1}\right), \tag{2.48}$$

where an auxiliary non-symmetric tensor χ' was defined such as

$$\chi' = \frac{\mu_0 \mu_B^2}{k_B T} g_e \mathbf{g}\langle SS^T\rangle, \tag{2.49}$$

which differs from the magnetic susceptibility tensor, χ, by a factor of $g_e/\mathbf{g}^T$ *i.e*,

$$\chi' = \frac{\mu_0 \mu_B^2}{k_B T}\mathbf{g}\langle SS^T\rangle \mathbf{g}^T. \tag{2.50}$$

Recently Lang et al. [27] noted that this approximation neglects the orbital and gauge correction contributions to the hyperfine tensor. Following a rigorous treatment with the inclusion of these neglected terms, the alternative semi-empirical (SE) quantum mechanical framework traditionally used in experimental PNMR [28–38], given by

$$\sigma^{\mathrm{pcs,lr}} \approx -\frac{1}{4\pi r^3}\chi\left(\frac{3\mathbf{r}\mathbf{r}^T}{r^2} - \mathbb{1}\right), \tag{2.51}$$

can be deduced, which instead suggests a relation between the dipolar shielding tensor and the conventional susceptibility tensor [39]. This approach should lead to more accurate predictions of $\sigma^{\mathrm{pcs,lr}}$.

Considering table 2.1 and equation 2.51, the contribution of the unpaired electrons to the total shielding tensor can be given by

$$\sigma^{\mathrm{S}} = \sigma^{\mathrm{con}} + \sigma^{\mathrm{pcs}} + \sigma^{\mathrm{pcs,lr}}, \tag{2.52}$$

where σ^{con} arises from the Fermi contact shift contributions. The terms σ^{pcs} and $\sigma^{\mathrm{pcs,lr}}$ account for the inter- and intramolecular spin dipolar induced pseudo-contact shift, respectively. The intra-molecular contributions of the PCS were explicitly separated from the conventional PCS term because they are calculated with the point-dipole approximation.

2.4.1 Line broadening from BMS effects

One of the main factors that hinders the interpretation of PNMR spectra is the loss of resolution of the resonances due to BMS induced broadening [40–42]. Here we introduce the BMS contributions to the shielding tensor, based on the theory of classical electrodynamics [43].

A system containing an ensemble of paramagnetic ions generates a demagnetising field, which in turn leads to a BMS contribution to the total shielding tensor, which can be determined to be

$$\sigma^{\mathrm{BMS}}(r) = \begin{cases} \chi_V\left[N^T(r) - \mathbb{1}\right], & \text{inside the crystallite} \\ \chi_V N^T(r), & \text{outside the crystallite,} \end{cases} \tag{2.53}$$

where χ_V is the volume susceptibility and N corresponds to the demagnetising tensor. These contributions can be separated in two groups, those due to the isotropic volume susceptibility of the crystallite – isotropic bulk magnetic susceptibility (IBMS) effects – and those due to the volume susceptibility anisotropy – anisotropic bulk magnetic susceptibility (ABMS) effects.

In a powder sample, we need to also take into account the contributions of neighboring crystallites, where both the IBMS and ABMS shielding tensors of a particular crystallite depend on the configurations of the surrounding crystallites, their sizes, and the orientations of the volume susceptibility tensors. We also note that, as shown in figure 4.1, each crystallite is orientated independently of the others. VanderHart et al. [44] and Alla and Lippmaa [40] have demonstrated that this effect results in a distribution of anisotropic shifts, due to the contribution of the IBMS of the surrounding crystallites, and a distribution of both isotropic and anisotropic shifts due to their ABMSes. The ABMS induced shift dispersion often results in NMR linewidths of the order of 10-100 ppm. Recently, Pigliapochi et al. [45] have demonstrated that the ABMS induced anisotropic shift can be correlated with the aspect ratio of particles in single crystals.

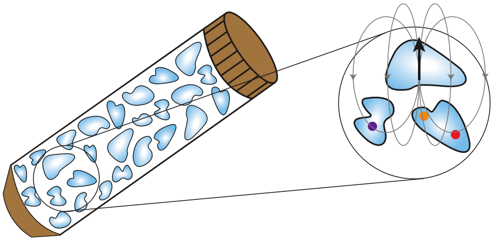

Figure 2.4: Illustration of the bulk magnetic susceptibility effects. The nuclei in the positions denoted in orange, red, purple do not experience the same nuclear shielding due to the nearby crystallites. Adapted from [46].

2.4.2 Paramagnetic relaxation enhancement

One additional feature of paramagnetic systems from the point of view of NMR is their relaxation properties. PRE of nuclear spins is among the earliest paramagnetic effects observed and was originally explored to decrease relaxation times [47]. As a consequence of the hyperfine coupling between the electron magnetic moment and the nucleus, stochastic fluctuations in the electronic magnetic moment cause large fluctuations in the local magnetic field experienced by the nucleus, which provides an efficient mechanism for relaxation [48]. The two main mechanisms for nuclear PRE are the dipolar hyperfine coupling to distant electrons – Solomon mechanism – and Fermi-contact coupling to electrons at the site of the nucleus – Bloembergen mechanism. Dipolar PRE is particularly strong for those nuclei lying in close spatial proximity to the metal center, and can occur over very large distances, particularly, considering the efficient spin diffusion mechanism among protons. At small through-bond distances from the metal center ($\sim$1-4 bonds away) due to relatively strong Fermi contact couplings.

The enhanced nuclear transverse relaxation rates causes line broadening, which often compromises spectral resolution. However, the delay time between repeated NMR experiments which is limited by the nuclear longitudinal relaxation rate is also reduced, permitting rapid repetition of experiments.

3

Basics of Quantum Chemistry

The interpretation of NMR spectra of paramagnetic systems is inherently more complicated than for diamagnetic materials due to the additional contributions to the shift as well as the presence of paramagnetic line broadening. Consequentially, in addition to the orbital term, the contributions of the Fermi contact interaction as well as contributions arising from the interaction between the hyperfine anisotropy and the magnetic anisotropy of the paramagnetic center have to be calculated. The choice of computational method is mostly determined by the desired property, but also by the size of the system. In this chapter we will provide a brief overview of the computational methods used to calculate these contributions.

The general goal of electronic structure calculations consists in finding an approximate solution to the time-dependent Schrödinger equation

$$\hat{H}\psi = E\psi, \tag{3.1}$$

where $\hat{H}$ is the Hamiltonian of the system, ψ is the N-particle wave function of the system and E is the total energy of the system. It is important to note that the Hamiltonian may be augmented by relativistic contributions. This equation is solved within the Born-Oppenheimer approximation, which implies that the electrons are moving in a field of steady nuclei, and, hence, the nuclear kinetic energy is considered zero and E represents the electronic energy. The justification for this approximation stems from the difference in mass of electrons and nuclei and, consequentially, in speed of motion. This equation is typically solved using either wave function-based methods or Kohn-Sham density functional theory (DFT).

3.1 Wave function-based methods

The simplest wave function-based method is called Hartree-Fock (HF). In it, each electron is described by an orbital, and the total wave function by a product of orbitals. The overall wave function must be antisymmetric, since electrons are indistinguishable fermions *i.e.* particles with a spin of $1/2$. The trial wave function can be generated by arranging the orbitals in a Slater determinant, and the best set of orbitals are determined using the variational principle, that is, any trial Slater determinant will have an energy expectation value that is greater or equal to the true ground-state wave function, thus, by minimizing the energy we determine the HF wave function closest to it. The HF model accounts for the interactions of the nuclei with each other and with the electrons. However, the electron-electron interaction is only approximated via the HF potential, where each electron interacts only with the averaged charge of all electrons. Since the other electrons are described by their respective orbitals, in order to minimize the energy, we are forced to solve a set of equations that depends on its own solutions, and, therefore, must be solved iteratively until the Slater determinant is self-consistent with the HF equations it generates. Expanding the molecular orbitals in a basis set permits the formulation of this method as an matrix eigenvalue problem, where the Fock operator correspond to integrals of one-and two-electron operators over basis functions multiplied by density matrix elements [49].

Exact wave functions cannot generally be expressed via a single Slater determinant, therefore the limit of the lowest energy that can be determined with a single wave function is always above the exact solution of the Schrödinger equation. The difference is called correlation energy and is normally distinguished in two types of effects [50], the dynamic correlation, which is associated with “instant” short-range correlation between electrons, and static correlation, which describes near-degeneracy effects between different configurations. These two effects are not entirely separable.

There are three main methods for calculating electron correlation: Many-Body Perturbation Theory (MBPT), Configuration Interaction (CI) and Coupled Cluster (CC). MBPT accounts for electron correlation effects by treating them as a perturbation to the Hartree-Fock wave function. Møller-Plesset (MP) corresponds to the particular case where the perturbed Hamiltonian is the sum over Fock operators and the perturbation corresponds to the difference between the electron-electron Coulomb interaction and the HF potential. To indicate up to what order of correction is included, these methods are typically referred to as MPn, where n is corresponds to the order of approximation. It is noteworthy to point out that the zeroth-order correction corresponds to HF energy and the first-order correction is zero. MP2 typically accounts for 80-90% of the correlation energy [49], and it is the least expensive method for including electron correlation, higher order approximations are typically not cost-effective and their convergence to the “correct” correlation effect can be erratic. Furthermore, for the calculations of molecular properties, increasing the order of the approximation does not necessarily lead to improvements in accuracy [50].

CI is an extension HF method where the trial wave function is instead a linear combination of Slater determinants with the expansion coefficients determined by minimizing the total energy. These additional Slater determinants are built by exciting electrons from orbitals occupied in the HF ground state determinant into non-occupied orbitals [51]. This method is, however, generally not a routine computational procedure, since even with truncation of the number of excited states. One extension of this method which is still considered to be CI [49] is the Multi-Configuration Self-Consistent Field (MCSCF) where not only the coefficients in front of the determinants but also the molecular orbitals are optimized [52]. Since the number of MCSCF iterations generally increases with the number of configurations included, the size of the wave function has to be smaller than for conventional CI. One popular method of selecting configurations necessary to calculate properties of interest is the Complete Active Space Self-Consistent Field (CASSCF) method, where the orbitals are divided in three subspaces: double occupied, active (partially occupied) orbitals and(c) virtual (empty) orbitals. CASSCF is able to describe a major part of the static correlation, however, in order to include dynamical correlation, the obtained wavefunction often needs to be refined. This is achieved by employing methods that use the multi-determinant wavefunction as reference. One popular choice are the generalizations of second-order Møller-Plesset perturbation theory to multi reference wavefunctions, such as N-electron valence state second-order perturbation theory (NEVPT2) [53–55].

Lastly, in Coupled-Cluster methods the trial wave function is also a linear combination of Slater determinants, but as opposed to CI, excited determinants are generated from the reference wave function via the exponential cluster operator which includes all corrections of a given type to infinite order [56].

3.2 Density functional theory

An alternative way to solve the many-electron time-independent Schrödinger equation is to use DFT, where the key variable is the electron density. As demonstrated by the theorems of Hohenberg and Kohn, the energy of an atomic system, as well as other observables, can be determined by the electronic density. The significance of this result and why DFT-based applications account for a significant part of the field of computational chemistry [57], lies in the fact that the electron density is independent of the number of electrons, which means it is independent of the system size, as opposed to wave function-based methods, where the complexity of a wave function increases exponentially with the number of electrons [49]. Hohenberg and Kohn also demonstrated that the minimum of the total energy functional can be determined using the exact density of the ground state. However, the exact form of that functional is unknown.

The first DFT models attempted to express all the energy components as a functional of the electron density, but, unfortunately, they had an overall poor performance. Kohn and Sham suggested that the electron kinetic energy should be calculated from an auxiliary set of orbitals used for representing the electron density. Consequentially, this results in an expression where the only unknown functional is the exchange-correlation energy, which corresponds to a small fraction of the total energy. It is important to note that this consideration significantly increases the complexity of the problem. Furthermore, similarly to the Hartree-Fock method, the Kohn-Sham operator depends on the molecular orbitals we seek to calculate, therefore, an iterative procedure also needs to be carried out to find these orbitals.

Several models with increasing complexity have been proposed for the exchange correlation functional. The simplest approximation being the local density approximation (LDA), where in each point of space the exchange-correlation term is the same as that of a uniform electron gas, which for most systems underestimates the exchange energy. Making the exchange-correlation term dependent on the density gradient (generalized gradient approximation, GGA), as opposed to approximating the electron density to be constant, normally leads to substantial improvements. A logical extension of GGA methods is to consider second order derivative of the electron density, with the Laplacian. This class of methods is called meta-GGA. DFT results can also be improved by using hybrid functionals that include some exact exchange energy from HF to compensate the self-interaction error in DFT [58]. We note that all these methods contain parameters which are determined either by enforcing that the functional fulfills certain of criteria, such as asymptotic behaviors or scaling properties, or by fitting experimental data, or a combination of both. At the present moment, as opposed to traditional wave function-based *ab-initio* theory, there are still no clear standard methods for DFT. and, consequentially, there is an ever growing "zoo" density functional approximations [59]. The "best" functional normally depends on the system and properties of interest.

3.3 Basis sets

All of the preceding methods require the knowledge of molecular orbitals, which are unknown functions. For this reason, they are approximated via expansion in a set of known functions, referred to as basis set. Since a complete basis set implies an infinite number of basis-functions, calculations are carried out with an incomplete basis set. In general, the smaller the basis set, the poorer the representation of the wave function, but, the type of basis function also influences accuracy. There are two types of basis functions for atomic orbitals, Slater-type orbitals (STOs) and Gaussian type orbitals (GTOs), which have the following functional form in spherical coordinates:

$$\xi^{\mathrm{STO}}_{\zeta,n,l,m}(r,\theta,\phi) = N Y_{l,m}(\theta,\phi) r^{n-1} \exp(-\zeta r), \tag{3.2}$$

$$\xi^{\mathrm{GTO}}_{\zeta,n,l,m}(r,\theta,\phi) = N Y_{l,m}(\theta,\phi) r^{2n-2-l} \exp\left(-\zeta r^2\right), \tag{3.3}$$

where N is a normalization factor, r is the distance of the electron from the atomic nucleus, ζ is a constant related to the effective charge of the nucleus, $Y_{l,m}(\theta,\phi)$ are spherical harmonic functions, and n, l, m are the wave function quantum numbers. Since GTOs are easier to compute, they are generally preferred.

A large number of different basis sets have been proposed over the years due to the fact that different theoretical methods and molecular properties have different basis set demands, different computer architectures and algorithms have different efficiency requirements, and the desired accuracy varies with the application [60]. Furthermore, in order to model extended (infinite) systems, such as unit cells of solid systems with periodic boundary condition, the translational invariance of all quantities also needs to be considered. Plane-wave basis functions are often used for this type of systems [61], although GTOs have also been implemented. [62].

4

Adiabatic Pulses in Solid-State MAS NMR: A Unified Analysis

In paramagnetic systems, or systems containing very broad anisotropic interactions, it is inherently challenging to excite and manipulate the spectra, primarily due to limitations in the the bandwidth of the pulses. More specifically, π pulses often have bandwidths limited to around 100 kHz. When this is the case, conventional pulses are not suitable for excitation. One possible alternative is acquiring the NMR spectrum in pieces, varying the transmitter frequency, and subsequently sum the result. This technique is often referred to as spin-echo mapping, variable offset cumulative spectroscopy (VOCS), or frequency stepping [63–78]. The two obvious limitations of this method are its lack of versatility, since it can only be readily applied to simple one-dimensional NMR spectra, and total experimental time, since it requires the acquisition of multiple sub-spectra, which is particularly deleterious for nuclei with low sensitivity. One perhaps more elegant alternative broadband pulse scheme is the swept-frequency adiabatic pulse [79] which has been commonly used in both liquid-state NMR and MRI. In this chapter, following paper I, we will proceed to present a rigorous and unified description of the underlying theory of frequency-swept pulses applied to spinning solids in different power regimes as well as illustrative examples of their applicability to paramagnetic systems.

Many swept-frequency adiabatic pulse schemes have been designed, namely the hyperbolic secant [80], tanh/tan [81] and Wideband, Uniform Rate, and Smooth Truncation (WURST) [82] with amplitude $\omega_1(t)$, phase $\phi_{\text{pul}}(t)$ and sweep of the transmitter offset $\omega_{\text{RF}}(t)$, which is defined as

$$\omega_{\mathrm{RF}}(t) = \frac{\mathrm{d}\phi_{\mathrm{pul}}(t)}{\mathrm{d}t}. \tag{4.1}$$

The profiles of these pulses are drawn in figure 4.1 and the corresponding governing equations are given in table 4.1. These pulses are designed so that over the course of the pulse duration τ_p, the variation in the pulse phase causes the transmitter offset to sweep through a range of frequencies $\Delta\omega$, while the amplitude increases from zero, at the start of the pulse up to its maximum value at its midpoint $t = \tau_p/2$, and then scales back to zero at the end of the pulse. Both amplitude and phase profiles are symmetric with respect to the midpoint of the pulse ($t = \tau_p/2$), as shown in figure 4.1.

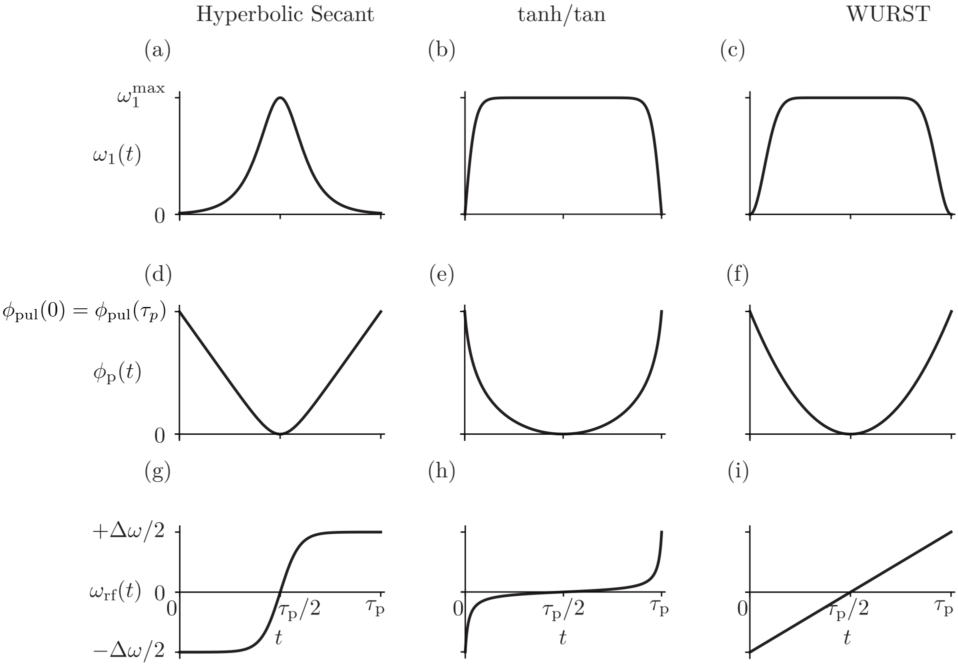

Figure 4.1: Amplitude $\omega_1(t)$ (a)-(c), phase $\phi_{\mathrm{pul}}(t)$ (d)-(f), and frequency-sweep profiles (g)-(h) for hyperbolic secant [80], tanh/tan [81] and WURST [82] frequency-swept adiabatic pulses. All waveforms have symmetric amplitudes and phases with respect to the midpoint of the pulse ($t = \tau_p/2$). It is also worth noting that close to the midpoint of the pulse, the frequency-sweep behaves approximately linearly. Adapted from [11], with permission from Elsevier.

Hyperbolic secant [80]	$\omega_1(t) = \omega_1^{\max} \operatorname{sech}\left[\beta\left(2\frac{t}{\tau_p} - 1\right)\right]$ $\phi_{\text{pul}}(t) = -\frac{\Delta\omega_1 \tau_p}{4\beta} \log\left\{\operatorname{sech}\left[\beta\left(\frac{2t}{\tau_p} - 1\right)\right]\right\}$ $\omega_{\text{rf}}(t) = \frac{\Delta\omega_1}{2} \tanh\left[\beta\left(\frac{2t}{\tau_p} - 1\right)\right]$
tanh/tan [81]	$\omega_1(t) = \begin{cases} \omega_1^{\max} \tanh\left(\frac{2\xi t}{\tau_p}\right), & 0 \leq t \leq t_p/2 \\ \omega_1^{\max} \tanh\left[2\xi\left(1 - \frac{t}{\tau_p}\right)\right], & 0 < t \leq t_p/2, \end{cases}$ $\phi_{\text{pul}}(t) = -\frac{\Delta\omega_1 \tau_p}{4\kappa \tan\kappa} \log\left\{\cos\left[\kappa\left(1 - \frac{2t}{\tau_p}\right)\right]\right\}$ $\omega_{\text{rf}}(t) = -\frac{1}{2}\Delta\omega_1 \cot(\kappa) \tan\left[\kappa\left(1 - \frac{2t}{\tau_p}\right)\right]$
WURST [82]	$\omega_1(t) = \omega_1^{\max}\left\{1 - \left\lvert\sin\left[\pi\left(\frac{t}{\tau_p} - \frac{1}{2}\right)\right]\right\rvert^n\right\}$ $\phi_{\text{pul}}(t) = \frac{\Delta\omega_1}{2}\left(\frac{t^2}{\tau_p} - t + \frac{\tau_p}{4}\right)$ $\omega_{\text{rf}}(t) = \frac{\Delta\omega_1}{2}\left(\frac{2t}{\tau_p} - 1\right)$

Table 4.1: Amplitude $\omega_1(t)$, phase $\phi_{\text{pul}}(t)$ and sweep of the transmitter offset, $\omega_{\text{RF}}(t) = \mathrm{d}\phi_{\text{pul}}(t)/\mathrm{d}t$, for the Hyperbolic secant, tanh/tan and WURST frequency-swept adiabatic pulses. $\omega_1^{\max}$ is the maximum value of RF amplitude, τ_p is the pulse duration, $\Delta\omega_1$ the sweep width. For the hyperbolic secant, $\beta = \operatorname{sech}^{-1}(f)$ and f corresponds to the fraction of $\omega_1^{\max}$ at which the beginning and end of the amplitude profile are truncated. For the tanh/tan ξ and κ are dimensionless parameters that control the rate at which the amplitude profile reaches $\omega_1^{\max}$ and the steepness of the sweep of the transmitter offset, respectively. For the WURST n is a factor that modifies the rate at which the amplitude profile is smoothed from zero to $\omega_1^{\max}$.

4.1 Theory of adiabatic pulses for solids under MAS

The Hamiltonian for a single spin I with an SA tensor in a single crystallite in the rotating-frame, in the presence of a RF pulse with time-dependent phase ($\phi_{\text{pul}}(t)$) and RF amplitude ($\omega_1(t)$), is given by [20; 83]:

$$\hat{H}_{\text{rot. frame}}(t) = \left[\sum_{l=-2}^{+2} \omega_{\text{c}}^{(l)}(\gamma_{\text{PR}}) \exp(-il\omega_{\text{MAS}}t)\right] \hat{I}_z + \omega_1(t)\hat{R}_z[\phi_{\text{pul}}(t)]\hat{I}_x\hat{R}_z^{-1}[\phi_{\text{pul}}(t)]. \quad (4.2)$$

$\hat{R}_z[\phi_{\text{pul}}(t)]$ is the operator representing a rotation of the spin through the angle $\phi_{\text{pul}}(t)$ about the z-axis and . Firstly, we transform the Hamiltonian into the frequency-modulated frame to remove the time-dependence of the phase of the pulse, $\phi_{\text{pul}}(t)$, via a rotation of the Hamiltonian by $\hat{R}_z^{-1}[\phi_{\text{pul}}(t)]$,

$$\hat{H}_0(t) = \hat{R}_z^{-1}[\phi_{\text{pul}}(t)][\hat{H}_{\text{rot. frame}}(t) - \dot{\phi}_{\text{pul}}(t)\hat{I}_z]\hat{R}_z[\phi_{\text{pul}}(t)] \tag{4.3}$$

$$= \left[\sum_{l=-2}^{+2} \omega_{\text{c}}^{(l)}(\gamma_{\text{PR}})\exp(-il\omega_{\text{MAS}}t) - \omega_{\text{rf}}(t)\right]\hat{I}_z + \omega_1(t)\hat{I}_x. \tag{4.4}$$

The term

$$R_z^{-1}[\phi_{\text{pul}}(t)][-\dot{\phi}_{\text{pul}}(t)\hat{I}_z]\hat{R}_z[\phi_{\text{pul}}(t)] = -\omega_{\text{rf}}(t)\hat{I}_z \tag{4.5}$$

arises due to the motion of the frequency-moduated frame relative to the rotating-frame which induces “inertial fields” [84]. We now define the effective field in the frequency-modulated frame as

$$\omega_{\text{eff}}^{(0)}(t)^2 = \left[\sum_{l=-2}^{+2} \omega_{\text{c}}^{(l)}(\gamma_{\text{PR}})\exp(-il\omega_{\text{MAS}}t) - \omega_{\text{rf}}(t)\right]^2 + \omega_1(t)^2, \tag{4.6}$$

with a tilt angle $\theta^{(0)}(t)$ relative to the z-axis given by

$$\theta^{(0)}(t) = \arctan\left[\frac{\omega_1(t)}{\sum_{l=-2}^{+2} \omega_{\text{c}}^{(l)}(\gamma_{\text{PR}})\exp(-il\omega_{\text{MAS}}t) - \omega_{\text{rf}}(t)}\right]. \tag{4.7}$$

Considering the pulse waveforms shown in figure 4.1 and table 4.1, at $t = 0$ the effective field starts aligned along $+z$. As the amplitude ramps up to ω_1^{max}, the transmitter offset approaches 0, and changes sign at $\tau_p/2$, which causes the effective field to invert. We can also rewrite the Hamiltonian to

$$\hat{H}_0(t) = \omega_{\text{eff}}^{(0)}\hat{R}_y[\theta^{(0)}(t)]\hat{I}_z\hat{R}_y^{-1}[\theta^{(0)}(t)]. \tag{4.8}$$

where it becomes more clear that at the start of the pulse the total magnetization is also along $+z$, aligned with the effective field. If the effective field inverts very slowly, *i.e.* adiabatically, the magnetization remains locked to the effective field and, therefore, is also inverted. The conditions for which a pulse can be considered “adiabatic” and successfully invert the magnetization are dependent on the pulse bandwidth, RF field amplitude, MAS frequency and size of the SA.

4.1.1 High-power regime

In this regime we operate at magnitudes of maximum RF amplitude much larger than twice the spinning frequency, that is $\omega_1^{\text{max}} > 2\,\omega_{\text{MAS}}$. In the previous section we introduced the idea of the effective field inverting adiabatically which, in turn, causes the magnetization to remain spin-locked to the effective field. In order to quantify the adiabaticity of a pulse and explain why it governs inversion efficiency, we proceed to diagonalize the Hamiltonian via the transformation to the first adiabatic frame:

$$\hat{D}_1(t) = R_y^{-1}[\theta^{(0)}(t)]\,[\hat{H}_0(t)]\,R_y[\theta^{(0)}(t)]. \tag{4.9}$$

However, since, once again, the transformation is time-dependent, a correction term $\hat{C}_1$ arises

$$\hat{C}_1(t) = -\dot{\theta}^{(0)}(t)\hat{I}_y. \tag{4.10}$$

The transformed Hamiltonian $\hat{H}_1(t)$ is given by

$$\hat{H}_1(t) = \hat{D}_1(t) + \hat{C}_1(t). \tag{4.11}$$

If $\left|\left|\hat{D}_1(t)\right|\right| \gg \left|\left|\hat{C}_1(t)\right|\right|$, $\hat{C}_1(t)$ can be neglected and the Hamiltonian is therefore coincident with $\hat{D}_1(t)$ over the whole pulse, and the magnetization is locked in this first adiabatic frame. This condition is quantified by the adiabaticity factor Q_1 [80], with the inclusion of the time-dependent SA [84; 85],

$$Q_1 = \min_{t\in[-\infty,\infty]} \frac{||\hat{D}_1(t)||}{||\hat{C}_1(t)||} = \min_{t\in[-\infty,\infty]} \left|\frac{\omega_{\text{eff}}^{(0)}(t)}{\dot{\theta}^{(0)}(t)}\right|, \tag{4.12}$$

$$\frac{1}{Q_1} = \max_{t\in[-\infty,\infty]} \left|\frac{\dot{\theta}^{(0)}(t)}{\omega_{\text{eff}}^{(0)}(t)}\right|. \tag{4.13}$$

If $Q_1 \gg 1$ the pulse is, in principle, adiabatic. Raising $\omega_1^{\max}$ generally increases Q_1 which leads to a more effective spin-locking and, as a result, inversion performance. However, the modulation of the SA leads to rapid oscillations of $\theta^{(0)}(t)$ and $\omega_{\text{eff}}^{(0)}(t)$ and, hence, a weakening of the adiabatic condition.

It has been shown that Q_1 is not a thorough indicator of the true adiabaticity of a quantum mechanical process. Extending this transformation iteratively into subsequent adiabatic frames k, with spin axes (x_k, y_k, z_k) defining the subsequent effective fields, $k > 0$, as

$$\left[\omega_{\text{eff}}^{(k)}(t)\right]^2 = \left[\omega_{\text{eff}}^{(k-1)}(t)\right]^2 + \left[\dot{\theta}^{(k-1)}(t)\right]^2, \tag{4.14}$$

and the tilt angles as

$$\theta^{(k)}(t) = \arctan\left[\frac{\dot{\theta}^{(k-1)}(t)}{\omega_{\text{eff}}^{(k-1)}(t)}\right], \tag{4.15}$$

the diagonal and off diagonal terms become:

$$\begin{aligned}\hat{D}_k(t) = \omega_{\text{eff}}^{(k-1)}(t)\hat{I}_{z_k}, \hat{C}_k(t) = -\dot{\theta}^{k-1}\exp\left[i(k-1)(\pi/2)\hat{I}_{z_{k-1}}\right]\hat{I}_{y_{k-1}}& \\ \cdot\exp\left[-i(k-1)(\pi/2)\hat{I}_{z_{k-1}}\right].&\end{aligned} \tag{4.16}$$

Until the iterative transformations start diverging, $\hat{C}_k(t)$ becomes increasingly smaller than $\hat{D}_k(t)$. The corresponding adiabaticity factors in frame k, defined as

$$\frac{1}{Q_k} = \max_{t\in[-\infty,\infty]} \frac{\left|\left|\hat{C}_k(t)\right|\right|}{\left|\left|\hat{D}_k(t)\right|\right|}, \tag{4.17}$$

will, therefore, increase at first but ultimately decrease. The adiabaticity condition can thus be redefined in terms of a superadiabatic quality factor such that

$$Q_s \equiv \max\left(Q_k\right), \tag{4.18}$$

which instead quantifies how well the evolving Hamiltonian is locked by the superadiabatic frame, which in turn is a much more robust indicator of inversion efficiency than Q_1 [84; 86].

Simulated inversion and superadiabatic factor profiles as a function ω_1^{max} and ω_{MAS} for a single crystal orientation with an SA of 60 and 500 kHz using short high-power adiabatic pulses (SHAPs) are shown in figure 4.2. As expected, for the smaller SA not only is the magnitude of superadiabatic factors overall higher but also the peak RF field strength necessary to achieve inversion is overall lower.

The treatment we have carried out so far is general and can be applied to analyze any adiabatic pulse. However, the superadiabatic factor fails to account for the impact of the rotary resonance conditions on inversion performance. Moreover, in the low-power region, the small basins of good inversion are still observable which are also not accounted for by Q_s, as shown in figure 4.2. This indicates that Q_s is only a good indicator of inversion in the high-power regime.

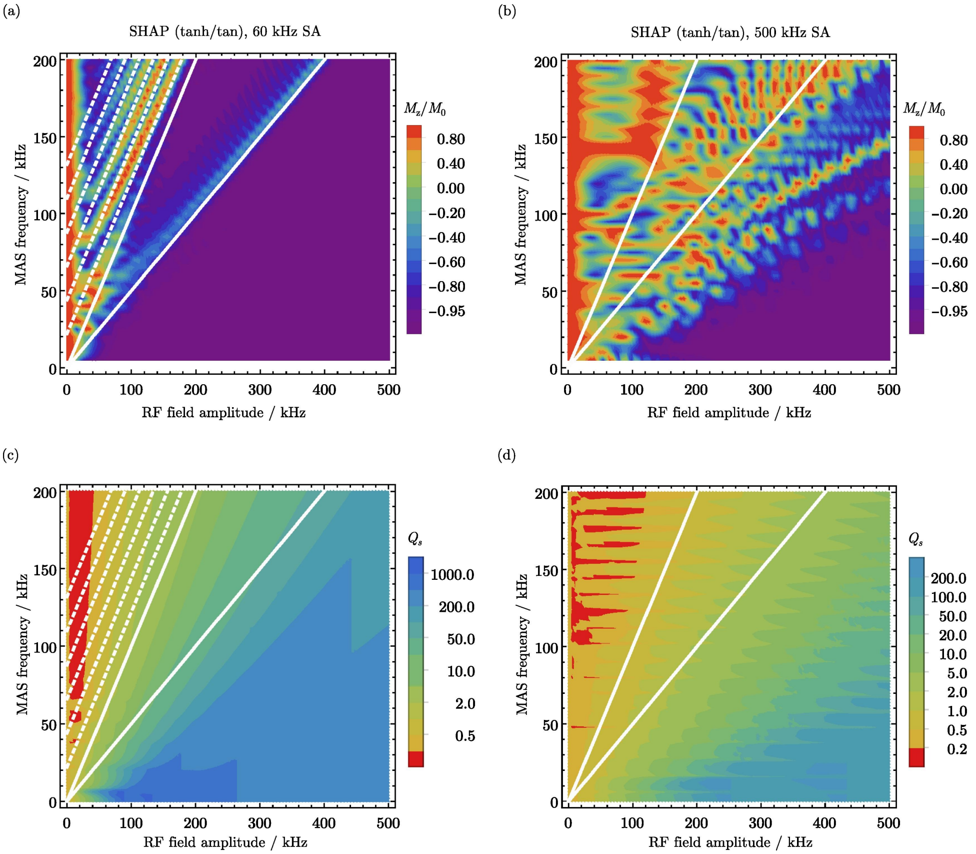

Figure 4.2: Simulated inversion profile and superadiabatic factor [87] contour plots for a SHAP (tanh/tan waveform, $\Delta\omega_1/2\pi = 5$ MHz, $\tau_p = 100\ \mu$s) as a function of MAS rate and peak RF field strength for a single crystal, transcribed from paper I. The simulations were carried out considering an SA tensor with asymmetry parameter $\eta = 0.5$ and 60 kHz ((a) and (c)) and 500 kHz ((b) and (d)) anisotropy. The chosen crystal orientation was $\Omega_{\text{PR}} = (0, \pi/4, 0)$. The z magnetization components after pulse irradiation were calculated via numeric integration of the Liouville-von Neumann equation, using the SA Hamiltonian in the rotating-frame, equation (4.2). The white lines highlight the rotary resonance conditions $\omega_1^{\max} = \omega_{\text{MAS}}$ and $\omega_1^{\max} = 2\,\omega_{\text{MAS}}$, and the dashed lines delineate the additional rotary resonance conditions with a periodicity in the MAS frequency dimension of 22 kHz. The superadiabatic factors were obtained numerically according to equations (4.13), (4.17) and (4.18), also considering the SA Hamiltonian in the rotating-frame.

4.1.2 Low-power regime

We proceed now to analyze inversion performance in the low-power regime, when $\omega_1^{\max} < \omega_{\mathrm{MAS}}$. Since the spin dynamics are notoriously complex, we start from the Hamiltonian in equation 4.2 and instead transform into the jolting frame [88], in an attempt to simplify our analysis. This frame is defined as the interaction representation of the spin interaction under MAS, which here is larger than the RF field. The operator that defines this transformation is

$$\hat{V} = \hat{R}_z\left[\phi_c(t)\right], \tag{4.19}$$

where $\phi_c(t)$

$$\phi_c(t) = \int_0^t \left[\sum_{l=-2}^{+2} \omega_c^{(l)}(\gamma_{\mathrm{PR}}) \exp\left(-il\omega_{\mathrm{MAS}}t'\right)\right] dt' \tag{4.20}$$

represents the phase accrued due to the evolution of the shift. The Hamiltonian in this frame is

$$\begin{aligned} \hat{H}_J &= \hat{R}_z^{-1}\left[\phi_c(t)\right]\hat{H}(t)\hat{R}_z\left[\phi_c(t)\right] \\ &\qquad - \left[\sum_{l=-2}^{+2} \omega_c^{(l)}(\gamma_{\mathrm{PR}}) \exp(-il\omega_{\mathrm{MAS}}t)\right]\hat{I}_z \qquad (4.21) \\ &= \omega_1(t)\hat{R}_z^{-1}\left[\phi_{\mathrm{pul}}(t)-\phi_c(t)\right]\hat{I}_x\hat{R}_z\left[\phi_{\mathrm{pul}}(t)-\phi_c(t)\right], \qquad (4.22) \end{aligned}$$

which can be rewritten as [88; 89]

$$\begin{aligned} \hat{H}_J = \omega_1(t) \sum_{m=-\infty}^{+\infty} A_c^{(m)} \hat{R}_z^{-1} &\left[\phi_{\mathrm{pul}}(t) - \varphi_c^{(m)} - \omega_c^{(0)}t - m\omega_{\mathrm{MAS}}t\right] \\ &\cdot \hat{I}_x\hat{R}_z\left[\phi_{\mathrm{pul}}(t) - \varphi_c^{(m)} - \omega_c^{(0)}t - m\omega_{\mathrm{MAS}}t\right], \end{aligned} \tag{4.23}$$

where $A_c^{(m)}$ and $\varphi_c^{(m)}$ are the intensity and phase of the mth-order sideband, where

$$\sum_m \left|A_c^{(m)}\right|^2 = 1. \tag{4.24}$$

At this point we consider a selective adiabatic pulse applied to the nth-order sideband and, therefore, we add the following linear phase to the adiabatic pulse phase $(\omega_c^{(0)} + n\omega_{\mathrm{MAS}})t$. The jolting frame Hamiltonian then has the form:

$$\begin{aligned} \hat{H}_J = \omega_1(t) \sum_{m=-\infty}^{+\infty} A_c^{(m)} \hat{R}_z &\left[\phi_{\mathrm{pul}}(t) - \varphi_c^{(m)} + (n-m)\omega_{\mathrm{MAS}}t\right] \\ &\cdot \hat{I}_x\hat{R}_z^{-1}\left[\phi_{\mathrm{pul}}(t) - \varphi_c^{(m)} + (n-m)\omega_{\mathrm{MAS}}t\right]. \end{aligned} \tag{4.25}$$

As shown in Pell et al. [89], this Hamiltonian can now be expressed as a Fourier series with a single characteristic frequency ω_{MAS}

$$\begin{aligned}\hat{H}_p = \frac{1}{2}\omega_1(t)\Big\{&A_c^{(n+p)}\exp\left[i\left(-\phi_{\text{pul}}(t)+\varphi_c^{n+p}\right)\right]\hat{I}_+ \\ &+A_c^{(n-p)}\exp\left[-i\left(-\phi_{\text{pul}}(t)+\varphi_c^{n-p}\right)\right]\hat{I}_-\Big\}, \qquad (4.26)\end{aligned}$$

where $\hat{I}_+$ and $\hat{I}_-$ are the raising and lowering spin operators. We are now in position to simplify this Hamiltonian via the effective Floquet Hamiltonian approximation [90; 91], truncated at third order. The details of this calculation are laborious and reproduced in full in ref. [89]. The first-order Hamiltonian is given by

$$\hat{H}_{\text{eff}}^{(1)} = \omega_1(t)A_c^{(n)}\hat{R}_z\left[\phi_{\text{pul}}(t)-\varphi_c^{(n)}\right]\hat{I}_x\hat{R}_z^{-1}\left[\phi_{\text{pul}}(t)-\varphi_c^{(n)}\right], \qquad (4.27)$$

which represents an RF pulse with phase $\phi_{\text{pul}}(t)-\varphi_c^{(n)}$ offset by the sideband phase and with amplitude $\omega_1(t)A_c^{(n)}$ scaled down by the irradiated sideband intensity. The second- and third-order Hamiltonians $\hat{H}_{\text{eff}}^{(2)}$ and $\hat{H}_{\text{eff}}^{(3)}$ are composed by a sum of terms $\gamma^{(2)}$ and $\gamma^{(3)}$,

$$\gamma^{(2)} = \frac{\omega_1(t)^2}{\omega_{\text{MAS}}}\left\{A^{(2)}\right\}\hat{I}_z, \qquad (4.28)$$

$$\gamma^{(3)} = \frac{\omega_1(t)^3}{\omega_{\text{MAS}}^2}\left\{A^{(3)}\right\}\hat{R}_z\left[\phi^{(3)}\right]\hat{I}_x\hat{R}_z^{-1}\left[\phi^{(3)}\right], \qquad (4.29)$$

where $\left\{A^{(n)}\right\}$ represents a product of n sideband intensities and ϕ_3 accounts for phase shifts introduced by both the pulse and the sidebands. In this way, $\hat{H}_{\text{eff}}^{(2)}$ acts as field along z and, hence, corresponds to frequency offset of the spin system analogous to a Bloch–Siegert shift [92]. The third-order term, however, is transverse and, therefore introduces phase-shifted magnetic fields which may reinforce or oppose the first-order field and consequentially improve or deteriorate inversion performance.

The main advantage of describing the spin system via the effective Floquet Hamiltonian approximation, as noted by Pell et al. [89], is that it effectively removes the oscillations from the magnetization trajectory that cause the conventional adiabatic factor to incorrectly predict poor inversion performance, as shown in figure 4.3. By defining the effective field $\omega_{\text{eff}}^{(0)}(t)$ and its tilt angle $\theta^{(0)}(t)$ considering instead the effective Floquet Hamiltonian it is possible to recalculate the (super)adiabatic factors [84] pertaining only to the smooth component of the z-magnetization. In figure 4.4 we show the superadiabatic factors profiles calculated considering the low-power approximation. Using this approximation we obtain a much better agreement with simulated inversion profiles of figure 4.3, as shown in figure 4.4.

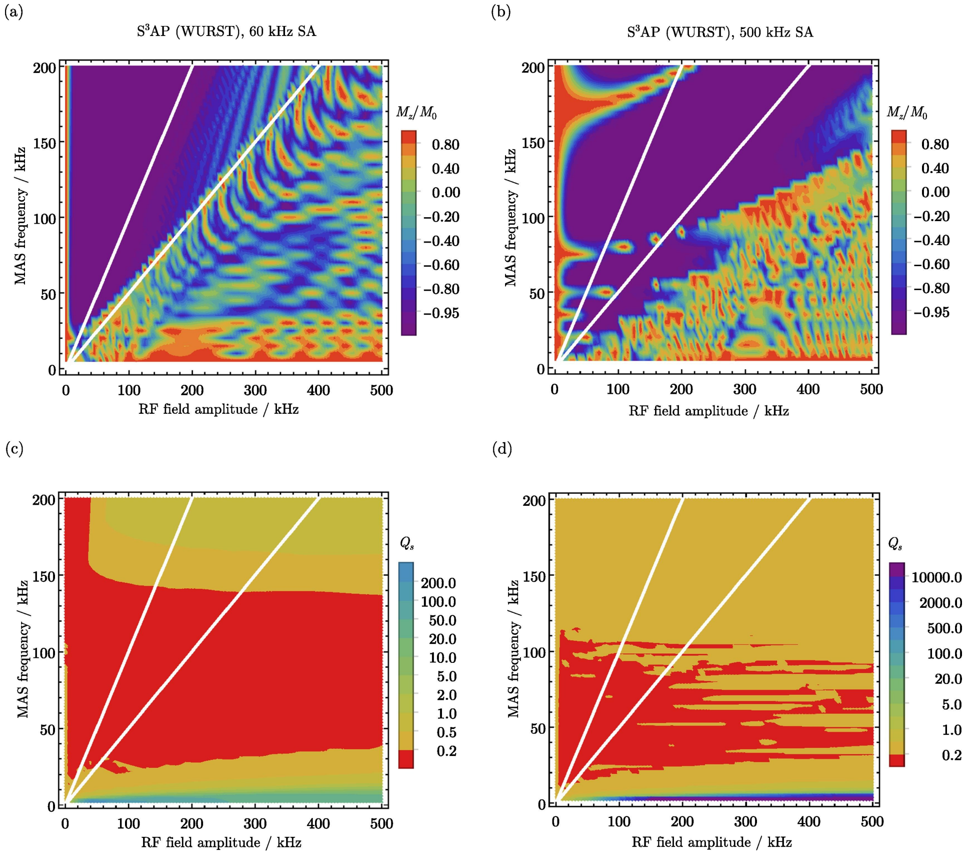

Figure 4.3: Simulated inversion profile and superadiabatic factor [87] contour plots for an S^{3}AP (WURST waveform, $\Delta\omega_1 = \omega_{\mathrm{MAS}}$, $\tau_p = 1$ ms) as a function of MAS rate and peak RF field strength for a single crystal, transcribed from paper I. The $z-$magnetization components after pulse irradiation were calculated via numeric integration of the Liouville-von Neumann equation, using the SA Hamiltonian in the rotating-frame, equation (4.2). The simulations were carried out considering an SA tensor with asymmetry parameter $\eta = 0.5$ and 60 kHz ((a) and (c)) and 500 kHz ((b) and (d)) anisotropy. The chosen crystal orientation was $\Omega_{\mathrm{PR}} = (0, \pi/4, 0)$. The white lines highlight the rotary resonance conditions $\omega_1^{\max} = \omega_{\mathrm{MAS}}$ and $\omega_1^{\max} = 2\,\omega_{\mathrm{MAS}}$. The superadiabatic factors were obtained numerically according to equations (4.13), (4.17) and (4.18), also considering the SA Hamiltonian in the rotating-frame.

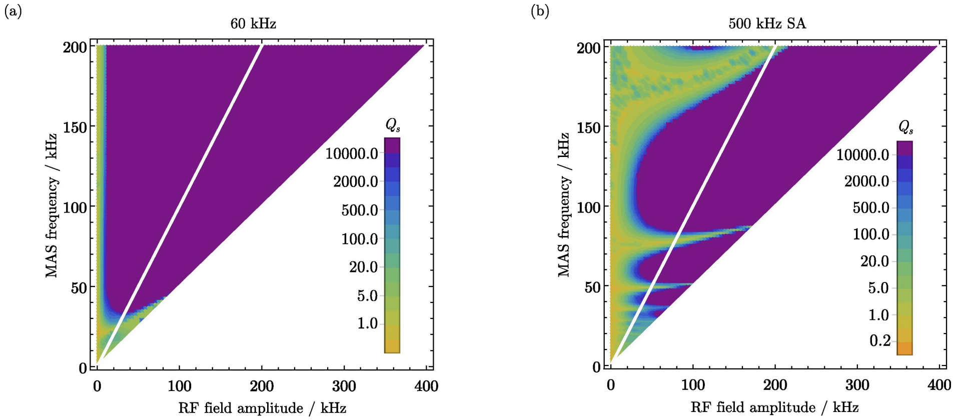

Figure 4.4: Superadiabatic factor [87] contour plots for an S^{3}AP (WURST waveform, $\Delta\omega_1 = \omega_{\mathrm{MAS}}$ irradiating the centerband, $\tau_p = 1$ ms) as a function of MAS rate and peak RF field strength for a single crystal using the low-power approximation up to the third-order effective Hamiltonian, transcribed from paper I. The simulations were carried out considering an SA tensor with asymmetry parameter $\eta = 0.5$ and 60 kHz (a) and 500 kHz (b) anisotropy. The chosen crystal orientation was $\Omega_{\mathrm{PR}} = (0, \pi/4, 0)$. The white line highlight the rotary resonance condition $\omega_1^{\mathrm{max}} = \omega_{\mathrm{MAS}}$. The superadiabatic factors were obtained numerically according to equations (4.13), (4.17) and (4.18), in the low-power approximation.

4.1.3 Intermediate-power regime

In figure 4.5 we showed the simulated trajectory of the magnetization for a SHAP rotary resonance condition in order to better understand the dynamics of the spin system. As the the trajectory of the magnetization progressively approaches the *xy* plane, where the sweep transmitter is resonant with the isotropic frequency, it starts to nutate away from the effective field.

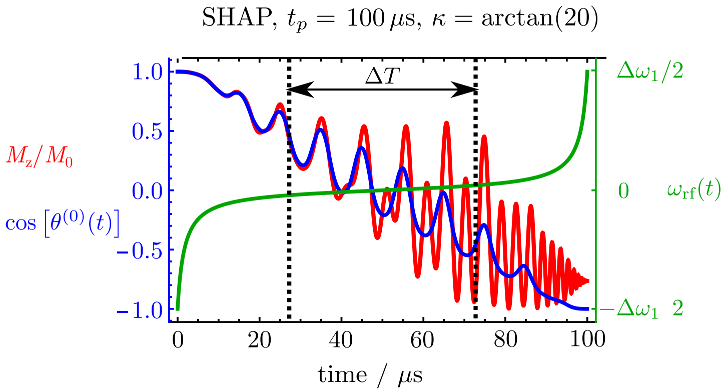

Figure 4.5: Simulated $z-$magnetization, $\cos\left[\theta^{(0)}(t)\right]$ trajectories, and frequency sweep $\omega_{\mathrm{rf}}(t)$ for SHAPs (tanh/tan waveform, $\Delta\omega_{\mathrm{RF}} = 5$ MHz, $t_p = 100$ μs, $\kappa = \arctan 20$) under rotary resonance conditions, with $\omega_{\mathrm{MAS}}/2\pi = 100$ kHz and $\omega_1^{\max}/2\pi = 200$ kHz. The intervals ΔT correspond to intervals of time where the divergence between the trajectories of the magnetization and effective field is most pronounced and are given by $\Delta T = 1/22$ ms. The simulations were carried out considering an SA tensor with asymmetry parameter $\eta = 0.5$ and 60 kHz anisotropy. The chosen crystal orientation was $\Omega_{\mathrm{PR}} = (0, \pi/4, 0)$. The trajectories and $z-$magnetization components after pulse irradiation were calculated via numeric integration of the Liouville-von Neumann equation, using the SA Hamiltonian in the rotating-frame, equation (4.2). Adapted from paper I.

Similarly to the low-power regime, it is convenient to transform the Hamiltonian 4.4 to a different frame in order to facilitate our analysis. This time we instead change into the frame of the interaction of the RF field commonly referred to as the toggling frame:

$$\begin{aligned}\hat{H}^{\mathrm{T}} &= \hat{R}_x\left[\beta_1(t,0)\right]^{-1}\left[\hat{H}_0(t) - \omega_1(t)\hat{I}_x\right]R_x\left[\beta(t,0)\right] \\ &= \left[\sum_{l=-2}^{+2} \omega_c^{(-l)}(\gamma_{\mathrm{PR}})\exp(il\omega_{\mathrm{MAS}}t) - \omega_{\mathrm{rf}}(t)\right] \\ &\qquad \times \left\{\cos\left[\beta_1(t,0)\right]\hat{I}_z + \sin\left[\beta_1(t,0)\right)\right]\hat{I}_y\right\}, \end{aligned} \tag{4.30}$$

where,

$$\beta_1(t_b, t_a) = \int_{t_a}^{t_b} \omega_1(t)dt. \tag{4.31}$$

is the accrued angle of rotation between times t_a and t_b about the RF field in the absence of off-resonance effects. At time close to τ, $\omega_{\mathrm{RF}}(t) = \omega_c^{(0)}$, which corresponds to $\tau = t_p/2$ if the transmitter offset is set to $\omega_{\mathrm{RF}}(t) + \omega_c^{(0)}$, and $\omega_1(t) \approx \omega_1^{\max}$

$$\hat{H}^{\mathrm{T}}(\tau) = \sum_{l=-2}^{+2}\sum_{m=-1}^{+1} \hat{H}_{l,m}\exp\left(il\omega_{\mathrm{MAS}}\tau\right)\exp(im\omega_1^{\max}\tau) \tag{4.32}$$

where

$$\hat{H}_{l,m} = \begin{cases} \frac{1}{2}\omega_{\mathrm{c}}^{(-l)}(\gamma_{\mathrm{PR}})(\hat{I}_z - mi\hat{I}_y), & l \neq 0, m \neq 0 \\ 0, & \text{otherwise.} \end{cases} \tag{4.33}$$

This Hamiltonian can be expressed as a Fourier series with two basic frequencies ω_{MAS} and $\omega_1^{\max}$,

$$\hat{H}(t) = \sum_{l=-\infty}^{+\infty} \sum_{m=-\infty}^{+\infty} \hat{H}_{l,m} \exp\left(il\omega_{\mathrm{MAS}}t\right) \exp\left(im\omega_1^{\max}t\right), \tag{4.34}$$

where the $\hat{H}_{l,m}$ operators satisfy the following relation

$$\hat{H}_{l,m} = \left(\hat{H}_{-l,-m}\right)^{\dagger}. \tag{4.35}$$

Once again we are in position to describe the spin system using the Floquet approximation. Truncating the Hamiltonian expansion at the second order term, we obtain

$$\hat{H}_{\mathrm{eff}}^{(1)} = \sum_{l_0,m_0} \hat{H}_{l_0,m_0} \tag{4.36}$$

$$\hat{H}_{\mathrm{eff}}^{(2)} = -\frac{1}{2} \sum_{l_0,m_0} \sum_{\lambda,\mu} \frac{\left[\hat{H}_{l_0-\lambda,m_0-\mu}, H_{-\lambda,-\mu}\right]}{\lambda\omega_{\mathrm{MAS}} + \mu\omega_1^{\max}}, \tag{4.37}$$

where l_0 and m_0 sum over all possible integers which satisfy the condition

$$l_0\omega_{\mathrm{MAS}} + m_0\omega_1^{\max} = 0, \tag{4.38}$$

i.e. degenerate Fourier states. The indices λ and μ sum over the values where the condition

$$\lambda\omega_{\mathrm{MAS}} + \mu\omega_1^{\max} \neq 0, \tag{4.39}$$

and thus describe non-degenerate Floquet states. If the rotary resonance conditions are avoided, the first-order effective Hamiltonian $\hat{H}_{\mathrm{eff}}^{(1)} = \hat{0}$, on the other hand if $\omega_1^{\max} = p\,\omega_{\mathrm{MAS}}$, with $p = 1, 2$, the first-order effective Floquet Hamiltonian and the effective Floquet Hamiltonian acts as field along z and y, as shown in paper I. Since in the toggling frame at $t = \tau$ the density operator, $\rho^T(\tau)$, is aligned along x, if rotary resonance conditions are avoided, the density operator remains spin-locked to the effective field. However, if we hit a resonance condition, the Hamiltonian is no longer locked to the effective field and evolves, analogously to conventional rotary resonance in a spin lock field [93].

Inspecting figure 4.5, under rotary resonance conditions, we still observe values of Q_s that are overall high, which indicates that the magnitude of the off-diagonal terms is significantly smaller than the diagonal term, yet the magnetization still diverges. Considering a superadiabatic tanh/tan such that:

$$\left|\theta^{(0)}(t)\right| \ll \left|\omega_{\mathrm{eff}}^{(0)}(t)\right|, \tag{4.40}$$

during the time interval ΔT, $\omega_{\mathrm{rf}}(t) \approx \omega_c^{(0)}$, and that we are examining a spin system where $\omega_1^{\max} > \left|\left\langle \sum_{l=-2,l\neq 0}^{+2} \omega_{\mathrm{c}}^{(l)}(\gamma_{\mathrm{PR}}) \exp(-il\omega_{\mathrm{MAS}}t) \right\rangle\right|$, the Hamiltonian in the Superadiabatic frame (SAF) can be expressed as:

$$\hat{H}_{\mathrm{SAF}} = \omega_1^{\max}\hat{I}_z + \frac{1}{2}\frac{1}{(\omega_1^{\max})^k} \sum_{l=-2,l\neq 0}^{+2} (-il\omega_{\mathrm{MAS}})^k \omega_{\mathrm{c}}^{(l)}(\gamma_{\mathrm{PR}}) \cdot \left[\hat{R}_z(\omega_{\mathrm{MAS}}lt)\hat{I}_+ R_z(-\omega_{\mathrm{MAS}}lt) + \hat{R}_z(-\omega_{\mathrm{MAS}}lt)\hat{I}_- R_z(\omega_{\mathrm{MAS}}lt)\right], \quad (4.41)$$

where, for simplicity, we assumed that in the adiabatic frame

$$\exp\left[i(k-1)(\pi/2)\hat{I}_{z_{k-1}}\right]\hat{I}_{y_{k-1}} \exp\left[-i(k-1)(\pi/2)\hat{I}_{z_{k-1}}\right] = \hat{I}_{x_k}. \quad (4.42)$$

By transforming this Hamiltonian to the frame that is rotating at the resonant frequency $j\omega_{\mathrm{MAS}}$, we obtain

$$\hat{H}_{\mathrm{rot,SAF}} = (\omega_1^{\max} - j\omega_{\mathrm{MAS}})\hat{I}_z + \frac{1}{2}\left(-\frac{ij\omega_{\mathrm{MAS}}}{\omega_1^{\max}}\right)^k \omega_{\mathrm{c}}^{(j)}(\gamma_{\mathrm{PR}})\hat{I}_+ + \frac{1}{2}\left(\frac{ij\omega_{\mathrm{MAS}}}{\omega_1^{\max}}\right)^k \omega_{\mathrm{c}}^{(-j)}(\gamma_{\mathrm{PR}})\hat{I}_- + \hat{H}_{\text{non-res}}(t), \quad (4.43)$$

where $\hat{H}_{\text{non-res}}(t)$ for the time-dependent terms that are not synchronous with $l\omega_{\mathrm{MAS}}$ and, hence, will have little impact on the trajectory of the magnetization, and the term $-j\omega_{\mathrm{MAS}}\hat{I}_z$ accounts for "intertial" fields arising from changing to the rotating-frame. Under rotary resonance conditions $\omega_1^{\max} = j\omega_{\mathrm{MAS}}$ with $j = 1, 2$, the magnetization vector will start rotating around an axis perpendicular to the z axis in an direct analogy to the effects of an RF pulse on the Zeeman Hamiltonian.

4.2 Applications

So far, our entire discussion on frequency-swept adiabatic pulses has been centered around population inversion whose practical applications are relatively limited. These pulses can, however, be used for refocusing (the transformation amplitude from coherence order -1 to $+1$ and vice-versa), provided the generated phase errors are canceled. Moreover, the refocusing efficiency can be linked directly to their inversion performance, using the excitation sculpting principle [79; 94–96], where pairs of back-to-back adiabatic pulses were utilized so that any phase errors generated by the first pulse are canceled by the second. In figure 4.6 we show the pulse sequences for both conventional and double adiabatic spin-echo sequences, as well as a comparison of their performance on the cathode material $\mathrm{LiFe_{0.5}Mn_{0.5}PO_4}$. The double adiabatic spin-echo sequence shows a notable improvement in bandwidth. However the conventional spin-echo sequences does yield improved sensitivity due to the fact that it minimizes PRE induced losses of signal intensity.

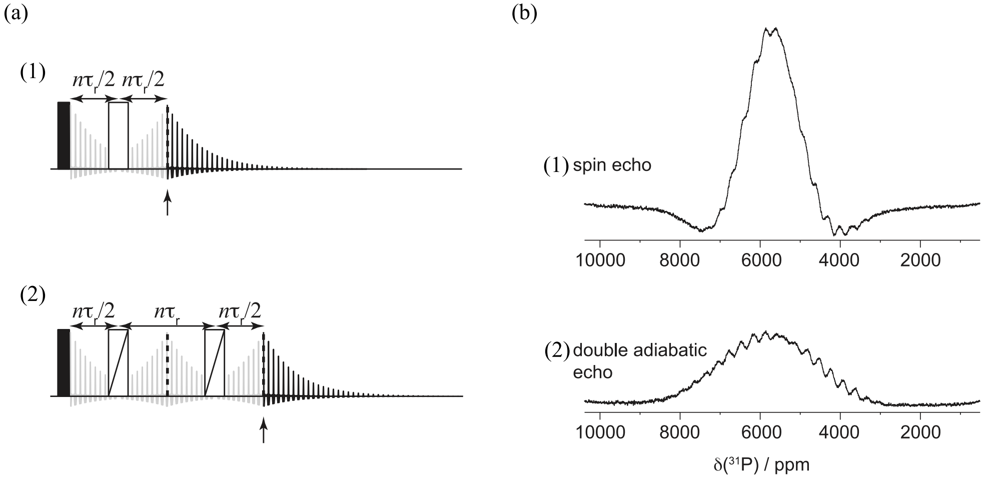

Figure 4.6: (a) Spin-echo pulse sequences: (1) Conventional Spin-Echo and (2) double adiabatic spin-echo. The arrow indicates the time point at which the isotropic shift is refocused, and must correspond to a multiple n of rotor periods τ_r. Filled rectangles indicate pulses with a nominal flip angle of 90°, unfilled rectangles indicate a 180° pulse and unfilled rectangles with a diagonal stroke indicate adiabatic pulses. All pulses have phase x. Adapted from [11], with permission from Elsevier. (b) Experimental example of improved refocusing properties of SHAPs when applied to paramagnetic materials compared to conventional pulses: (1) ^{31}P rotor-synchronized spin-echo spectra of the cathode material $LiFe_{0.5}Mn_{0.5}PO_4$ and (2) double-SHAP-echo spectra The SHAP is a tanh/tan pulse sweeping through 5 MHz in 50 μs . The RF field amplitudes were 417 kHz for all pulses and both spectra were recorded at 11.74 T at 60 kHz MAS. Adapted from [96], with permission from Elsevier.

A big advantage of frequency swept-pulses is that they can, in principle, replace π pulses in more sophisticated pulse sequences to improve bandwidth. An outstanding example of this is the application of the SHAPs in the two-dimensional Magic-Angle Turning (MAT) [97] experiment. Due to the large anisotropic effects induced by the paramagnetic centers, it is frequent that isotropic resonances overlap with spinning sidebands. In this situation, experiments like the MAT or the Phase Adjusted Spinning Sidebands (PASS) [98] sequence address this difficulty by separating shift and shift anisotropy in two-dimensions. Both experiments have the same basic pulse sequence comprising of a $\pi/2$ pulse, followed by a block of five π pulses with unique timings in order to result in a period of pure isotropic or anisotropic evolution, for MAT and PASS, respectively, and ending in direct acquisition. In contrast to conventional two-dimensional NMR experiments, the evolution time remains constant, and the evolution of the shift or SA is mapped out via the variation of the pulse timings. Considering the bandwidth limitations of π pulses, the applicability of these experiments in paramagnetic systems is relatively limited. The adiabatic MAT (aMAT) sequence [99], shown in figure 4.7(a), addresses specifically this hindrance, with only one additional sixth pulse inserted immediately after the excitation pulse to cancel phase errors. In figure

4.7(b) we show an example of an experimental aMAT spectrum recorded on ^{125}Te from the work carried out in paper A, where sets of inequivalent sites were identified and the corresponding SA parameters were extracted. Combining these results with quantum chemistry calculations permitted the breakdown of the lineshape in four inquivalent sites, which in turn demonstrated how DFT-assisted ssNMR can provide valuable insight into the topological band structure of WTe_2 and explore exotic physical phenomena. In chapter 5, based on paper II, we will also explore the application of theses pulses in an organoytterbium complex.

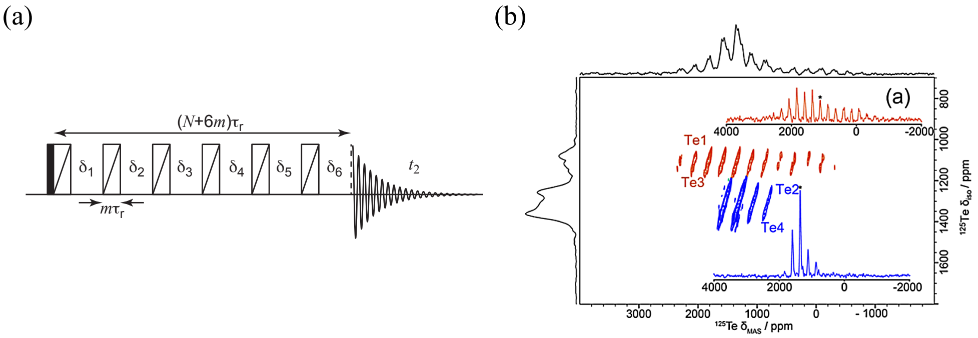

Figure 4.7: (a) The aMAT sequence where the length of the SHAP is an integer multiple *m* of the rotor period τ_r and with an evolution time of *N* rotor periods, where *N* is an integer that is not a multiple of 3. Filled rectangles indicate pulses with a nominal flip angle of 90°, unfilled rectangles indicate a 180° pulse. All pulses have phase *x*. Reprinted with permission from Clément et al. [99] (J. Am. Chem. Soc. 2012, 134, 17178-17185). Copyright 2012 American Chemical Society. (b) Experimental ^{125}Te aMAT NMR spectrum at 30 kHz MAS in magnetic field of 9.4 T. Adapted from paper A.

5

Geometry and Electronic Structure of $Yb(III)[CH(SiMe_3)_2]_3$

In recent years NMR, has emerged as an invaluable tool to study catalytic systems, due to its inherent ability to probe both local environments and electronic structure. [100–102]. As an example, our study of ultrafine Ni_2P nanoparticles carried out in paper B, precisely highlights the potential of solid-state NMR combined with DFT calculations in identifying the individual crystal facets of the terminating surfaces of the nanoparticles, which in turn provided valuable insight into the electronic origin of enhanced catalytic activity.

Heterogeneous catalysts, which involve systems where the catalyst is in different phase than reactants are highly relevant for chemical industry, due to easy separation of catalysts from reaction products [103]. These catalysts typically consist of a metal site bound to a surface such as silica or alumina [103–105]. However, NMR studies of surface-supported species whether via probing the interactions with silicon or studying carbon and nitrogen sites in ligand groups suffer from the drawback of low sensitivity due to the low natural abundance of the NMR active nuclei ^{13}C, ^{15}N and ^{29}Si, typically used to study them. One viable approach to address this limitation is to study molecular complexes that mimic the effect of binding a metal complex to a surface. In this chapter we will focus on discussing our work on a molecular organoytterbium complex, based on paper II, isostructural to a organolutetium studied in Conley et al. [106]. The lutetium complex exhibits an interesting secondary interaction between the ligand and the lanthanide metal center, which may play an important role in catalytic reactions by stabilizing the ground states and transition states. The ytterbium complex is expected to behave similarly, but the paramagnetic effects arising from the unpaired electron present additional difficulties in interpreting the NMR spectra. The characterization of this system is thus carried out by a combination of X-ray crystallography, solid-state NMR, EPR, magnetic susceptibility studies and quantum chemical calculations.

5.1 Structural characterization

The solid-state crystal structure of Yb[CH(SiMe$_3$)$_2$]$_3$ was determined by low-temperature X-ray crystallography at 100 K. The most important parameters of the low-temperature structure of Yb[CH(SiMe$_3$)$_2$]$_3$ are summarized in figure 5.1(b). The system crystallizes in the trigonal space group $P31c$ and point group C_3, as their previously studied lutetium analogue Lu[CH(SiMe$_3$)$_2$]$_3$ [106] (figure 5.1(a)). The similarity between the structures suggests that the hole in the $4f$-shell of the electronic structure of Yb(III) has little influence on the geometry or stereochemistry of the complex and, therefore, their frontier molecular orbitals. In both molecules, the lanthanide ion is elevated out of the plane defined by its ligands and all the distances and angles for the Lu and the Yb complexes indicate that they are the same within experimental error, with the exception of M-C$_2$ and M-Si$_2$, which are both longer for Yb, consistent with its larger ionic radius. The geometry of the complex also exhibits a conformational strain, such that Si$_2$ is significantly closer to the metal ion than Si$_1$, ascribed to the presence of a secondary interaction between the metal and the Si-Me$_3$ group for Si$_2$, that is absent for Si$_1$.

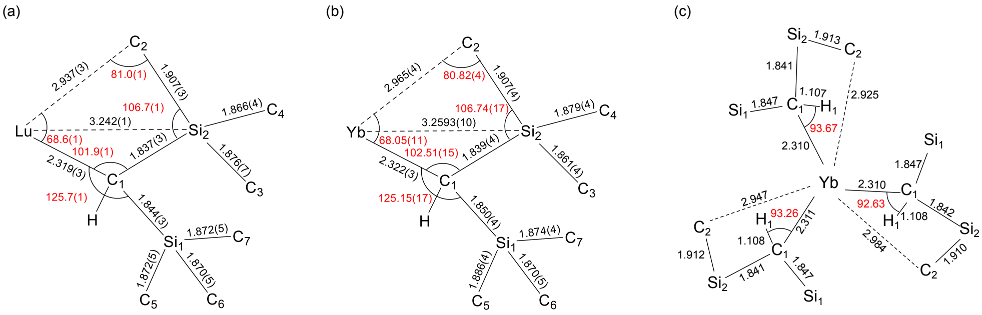
(a)
C_2
2.937(3)
81.0(1)
1.907(3)
106.7(1)
3.242(1)
1.866(4)
C_4
Lu
Si_2
68.6(1)
101.9(1)
1.837(3)
2.319(3)
C_1
1.876(7)
C_3
125.7(1)
H
1.844(3)
1.872(5)
C_7
Si_1
1.872(5)
1.870(5)
C_5
C_6
(b)
C_2
2.965(4)
80.82(4)
1.907(4)
106.74(17)
3.2593(10)
1.879(4)
C_4
Yb
Si_2
68.05(11)
102.51(15)
1.839(4)
2.322(3)
C_1
1.861(4)
C_3
125.15(17)
H
1.850(4)
1.874(4)
C_7
Si_1
1.886(4)
1.870(5)
C_5
C_6
(c)
Si_2
1.913
C_2
1.841
1.107
2.925
Si_1
1.847
C_1
H_1
93.67
2.310
Si_1
1.847
Yb
2.310
C_1
2.947
92.63
1.842
H_1
93.26
2.311
1.108
C_2
H_1
1.108
Si_2
C_1
2.984
1.912
1.847
1.910
Si_2
1.841
C_2
Si_1

Figure 5.1: Sketches of relevant bond lengths and angles: (a) Lu[CH(SiMe$_3$)$_2$]$_3$. (b) Yb[CH(SiMe$_3$)$_2$]$_3$. The Yb–Si$_1$ distance is 3.710 Å, while Lu–Si$_1$ distance is 3.677 Å. The hydrogens of the C$_3$-C$_7$ methyl groups are not shown for simplicity. (c) DFT optimized structure of Yb[CH(SiMe$_3$)$_2$]$_3$. The carbons of C$_5$-C$_7$ and the hydrogens of the C$_3$-C$_7$ methyl groups are not shown for simplicity. The Yb–Si$_1$ distance ranges between 3.711 and 3.716 Å (see table 6 of the SI for more details). All bond lengths are reported in Åand the bond angles (in red) are reported in degrees. Transcribed from paper II.

In order to further clarify whether the structure of Yb[CH(SiMe$_3$)$_2$]$_3$ exhibits the same geometry and bonding motif between the Yb center and C2 site, as the previously characterized Lu[CH(SiMe$_3$)$_2$]$_3$ [106], we carried out a geometry optimization at DFT level of theory, under the assumption that this complex possesses a single 4f^{13} configuration, corresponding to an electronic spin $S = 1/2$ and neglecting the inclusion of any excited states. The structure was computed for a single molecular complex, with atomic coordinates extracted from the low temperature XRD data, and without the inclusion of periodic boundary conditions. The optimization was carried out using the PBE0 functional [107–109] with D3BJ dispersion correction [110] and considering the relativistic ZORA Hamiltonian [111]. Symmetry restrictions were not enforced during geometry optimization, which unveiled a slight deviation from ideal C_3 symmetry, as shown in figure 5.1(c). It is important to note that all main parameters of the optimized structure are very close to those of the low-temperature solid-state XRD structure, and the close proximity of Si_2 to Yb compared to Si_1 is reproduced in the calculations.

The optimized structure is notable for their acute Yb-C-H angles of the α-H atoms (H1) of the $CH(SiMe_3)_2$ ligands, for the three C1 sites. This observed effect might be explained by a simultaneous electrostatic repulsion from the Yb center and the two Si atoms of the $(CH(SiMe_3)_2)_3$ ligand, resulting in a conformational strain. A similar effect was previously observed for the $(CH(SiMe_3)_2)_3$ ligands of the Lu(III)[106] or even for Ti(III) analogues [112]. This asymmetry in the bond lengths and bond angles is generally attributed to an agostic $M\cdots H{-}C\gamma$ or $M\cdots C\gamma{-}Si\beta$ interaction [113].

5.2 EPR characterization and magnetic susceptibility studies

The solid-state magnetic susceptibility was measured as a function of temperature between T = 2.6 and 300 K using an externally applied magnetic field of $H_{\text{ext}} = 1$ kOe. At T = 300 K the effective magnetic moment is 4.53 μ_B (χT = 2.5 cm^3 K mol^{-1}). These values are in good agreement with those from the electronic configuration of the free Yb(III) ion, which is described by a single $^2F_{7/2}$ term. The characterization the Yb(III) alkyl complex $Yb[CH(SiMe_3)_2]_3$ by continuous-wave (CW) EPR spectroscopy suggested an axial $S = 1/2$ spin Hamiltonian, having the g tensor principal values of $g^{\perp} = 0.7316$ and $g^{\|} = 7.5698$. From spectral simulation, the ^{171,173}Yb hyperfine tensors were determined to be $A^{\perp}(^{173}\text{Yb})$ = 221 MHz, $A^{\|}(^{171}\text{Yb})$ = 1650 MHz, and accordingly $A^{\perp}(^{171}\text{Yb})$ = 842 MHz. $A^{\|}(^{171}\text{Yb})$ = 6285 MHz.

A higher-resolution picture was then provided by pulsed EPR spectroscopy, more specifically 2D hyperfine sub-level correlation spectroscopy (HYSCORE) which revealed the presence of ^{1}H hyperfine couplings, resulting from the interactions of the electron spin with nuclear spins of hydrogen atoms of $CH(SiMe_3)_2$ alkyl ligands. The ^{1}H hyperfine tensor parameters were determined to be $A_{\text{iso}}(^1\text{H}) = 3.8 \pm 0.3$ MHz, $T_{\text{dip}}(^1\text{H}) = 4.0 \pm 0.5$ MHz ($A_{\text{dip}} = [-4.0 \pm 0.5; -4.0 \pm 0.5; 8.0 \pm 1.0]$ MHz), with the tensor's principal axis system rotated by $45° \pm 15°$ with respect to the z axis of the PAF of the g tensor. The HYSCORE spectrum was also consistent with the Electron Electron Double Resonance (ELDOR), detected NMR spectroscopy (EDNMR)[114] spectrum from which a single splitting due to an anisotropic hyperfine coupling to ^{1}H with $A_{\text{iso}}(^1\text{H}) = 3.1 \pm 0.7$ MHz and $T_{\text{dip}}(^1\text{H}) = 6.5 \pm 0.7$ MHz was extracted.

As an attempt to further validate our proposed structure and rationalize the EPR results we proceed to calculate the magnetic properties of the system. The calculations of the g tensor and magnetic susceptibility were carried out using multi-reference perturbation theory (CASSCF/NEVPT2) [53–55; 115–117], considering a single $S = 1/2$ $4f^{13}$ configuration and an active space comprising only of f orbitals (CAS(13,7)) including scalar relativistic effects using the second-orderr Douglas-Kroll-Hess Hamiltonian [118], as well as spin-orbit effects. The obtained results are summarized in table 5.1. The calculated g tensor and magnetic susceptibility agree well with the experimental results, which constitutes additional evidence that complex can be well described with a single configuration and that our proposed relativistic DFT optimized geometry is consistent with the EPR characterization.

	Experiment	Calculated
g_x	0.7316	0.6544
g_y	0.7316	0.6559
g_z	7.5698	7.7972
χT (300 K) [cm^{-3} K mol^{-1}]	2.50	2.34

Table 5.1: Comparison of experimental and calculated g tensor (g_x, g_y and g_z represent the components of g tensor in the PAF) and magnetic properties of Yb[CH(SiMe$_3$)$_2$]$_3$ complex. Calculated values were obtained using multi-reference perturbation theory (CASSCF/NEVPT2). Experimental values were obtained via EPR characterization and magnetic measurements. Transcribed from paper II.

The hyperfine coupling tensors for all the spin-active nuclei wer also calculated using both spin-component scaled MP2 (SCS-MP2) [119; 120] and DFT with the PBE0 functional [107–109], to ensure the consistency of our calculations. It is important to note that predicting the hyperfine coupling in lanthanide systems is extremely challenging, since it requires that the method is able to reproduce the spin-density correctly. Single-reference methods are often limited by the effects of spin contamination, and in the case of DFT the self-interaction error. From our results we can tentatively assign the single hyperfine interaction observed by HYSCORE and EDNMR to H_1, which have computed isotropic values in the range of -1.44 to 0.51 MHz, while the rest have a magnitude below 0.13 MHz. The quantitative discrepancies of the isotropic values can be explained by the close proximity of H_1 to Yb, where high-level relativistic electronic structure methods are required for accurate determination of the spin polarization and spin delocalization and the multireference character of the wave function [121]. Moreover, relativistic spin-orbit effects, which typically also require multireference methods to be accurately calculated, may play an important role. Nevertheless, our results predict an approximately axial spin-dipolar hyperfine coupling tensor of $T_{\text{dip}}(^1H_1) \sim 4$ MHz, which is in very good agreement with the experiments.

5.3 NMR characterization

While pulsed EPR spectroscopy allowed the observation of close ^{1}H nuclei, the more distant magnetic nuclei of Yb[CH(SiMe$_3$)$_2$]$_3$ can be observed via NMR spectroscopy [11]. We proceeded to examine the Yb[CH(SiMe$_3$)$_2$]$_3$ complex via solid-state NMR. The paramagnetic effects arising from the Yb$^{(III)}$ can be readily seen in the 1D MAS spectra of Yb[CH(SiMe$_3$)$_2$]$_3$ (figure 5.2(a-c)), which exhibit signals spread over hundreds of ppm, large anisotropies and extremely broad individual lineshapes. Employing the 2D aMAT sequence [122], we correlated each site to its anisotropic sideband pattern and thus removed the overlap of the spinning sideband manifolds. Two distinct resonances could clearly be observed for ^{1}H, ^{13}C and ^{29}Si (figures 5.2(d)-(f)) and the corresponding NMR parameters were determined by fitting the extracted slices (figures 5.2(g)-(i)). In order to calculate the δ_{iso} of each resonance and access the shift dispersion, the projections in the indirect dimension were fitted using asymmetric Gaussian functions defined as

$$f(\nu_1) = \frac{A}{\sqrt{2\pi\sigma}} \exp\left[-\frac{1}{2}\left(\frac{\omega-\mu}{\sigma}\right)^2\right] \operatorname{erfc}\left[-\frac{\alpha(x-\mu)}{\sqrt{2}\sigma}\right] \tag{5.1}$$

where A, μ, σ are the amplitude, mean and standard deviation of the Gaussian function, α is a scale factor and erfc is the complementary error function,

$$\operatorname{erfc}(z) = \frac{2}{\sqrt{\pi}} \int_z^\infty \exp\left(-t^2\right) dt. \tag{5.2}$$

The mean and standard deviation of the distribution are given by:

$$\mu_{\text{asym,gaus}} = \mu + \frac{\sqrt{\left(\frac{2}{\pi}\right)\alpha\sigma}}{\sqrt{(1+\alpha^2)}} \tag{5.3}$$

$$\sigma_{\text{asym,gaus}} = \left[1 - \frac{2\alpha^2}{\pi(1+\alpha^2)}\right]\sigma^2 \tag{5.4}$$

It is reasonable to tentatively assign each signal to the two inequivalent SiMe$_3$ groups, *i.e.* the two signals V and VI being due to the two inequivalent Si nuclei (specifically, one due to Si$_1$ and the other to Si$_2$), and each ^{13}C signals (III and IV) arising from the three methyl groups attached to each of the Si and the ^{1}H signals (I and II) to the corresponding group of protons (H$_{2/3/4}$ and H$_{5/6/7}$).

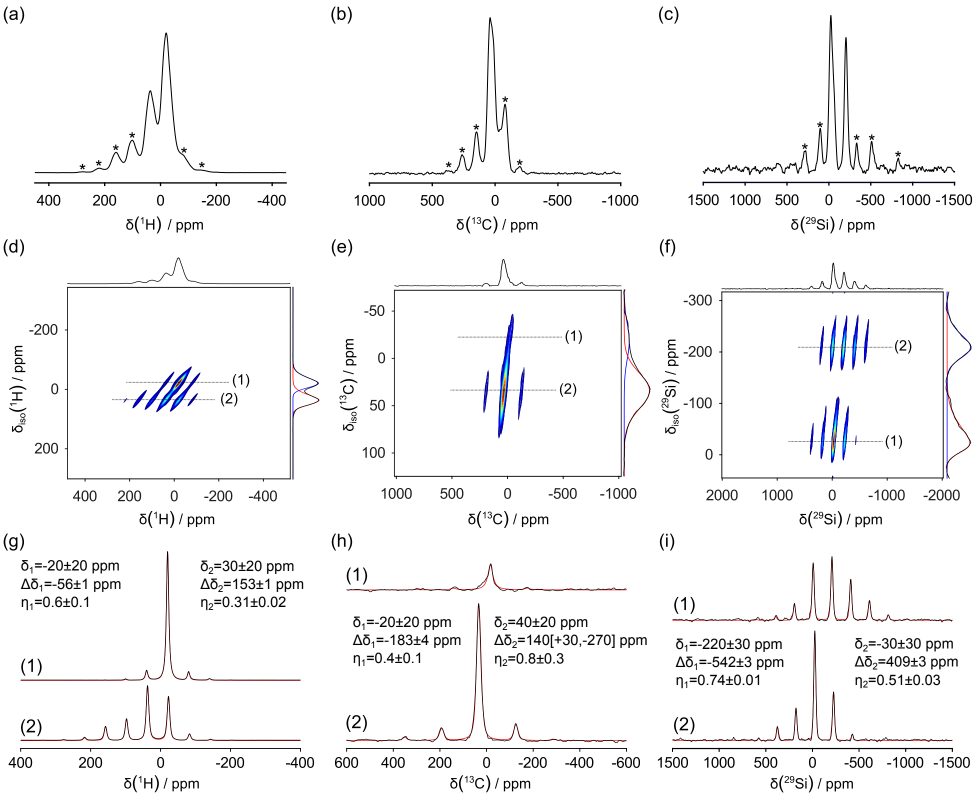

Figure 5.2: 1D NMR spectra of Yb[CH(SiMe$_3$)$_2$]$_3$: (a) ^{1}H MAS spectra at 30 kHz MAS,(b) ^{13}C MAS spectra of at 14.286 kHz MAS and (c) ^{29}Si MAS spectra at 30 kHz MAS, showing two distinct ^{29}Si signals. The spinning sidebands are marked by asterisks ($*$). 2D aMAT spectrum: (d) ^{1}H at 30 kHz, (e) ^{13}C at 20 kHz and (f)^{29}Si at 20 kHz. The indirect dimension projections were deconvolved using asymmetric Gaussian functions to extract the isotropic shifts and quantify shift dispersion. (g)-(i) extracted slices with isotropic shift corresponding to the maxima of the deconvolved projections and labelled with Roman numerals. Each slice was subsequently fitted considering a simple CSA model using the Haeberlen convention [14]. Transcribed from paper II.

To obtain a proton-carbon site-specific resonance assignment and confirm our hypothesis, a 2D heteronuclear correlation (HETCOR) spectrum was acquired. Since cross-polarization (CP) based dipolar polarization transfers are typically inefficient, the HECTOR variant of the Transferred Echo Double Resonance (TEDOR) sequence was utilized. This pulse sequence transfers polarization from protons via short dipolar-recoupling sequences that use high-powered short RF pulses and thus has been proven to be quite successful in paramagnetic systems [123; 124]. In figure 5.3 the 2D ^{1}H-^{13}C correlation spectrum is shown where correlations between signals I and III and between II and IV are observed. Considering the shift tensor parameters (isotropic shift δ, shift anisotropy $\Delta\delta$ and asymmetry parameter η) (Figures 5.2(g)-(i)) obtained by fitting the 2D aMAT slices, we can assign the set of three signals, I, III and VI, with larger isotropic shift and shift anisotropy to the same SiMe$_3$ group and the signals signals II, IV and V, to the other SiMe$_3$ group.

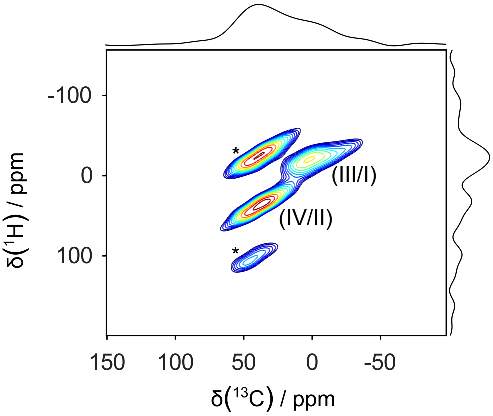

Figure 5.3: ^{1}H-^{13}C correlation spectrum achieved by using the TEDOR experiment [124] at 30 kHz MAS, yielding two distinct correlations of the resonances (III/I) and (IV/II), as shown in figure 5.2. The spinning sidebands are marked by asterisks ($*$). Transcribed from paper II.

This assignment also implies that the two resonances corresponding to C$_1$ and H$_1$ are absent from all the NMR spectra. This may be a consequence of the severe reduction of sensitivity due to the large paramagnetic relaxation enhancement expected for these nuclei in close proximity to the Yb, or to the fact that potentially large shifts push them out of the excitation window. In order to verify this hypothesis, we calculate the paramagnetic contribution to the total shift of H$_1$ (see equations 2.52 and 2.40 of chapter 2), considering the experimental ^{1}H hyperfine tensor assigned to H$_1$ and the calculated g tensor. Since the HYSCORE spectrum indicates that the z axis of the PAF of the g and A tensor have a fixed relative orientation of 45°, the PAF of the A tensor needs to be transformed to the PAF of the g tensor, and subsequently rotated again considering a distribution of Euler angles (ZYZ convention) with β fixed at 45°.

In figure 5.4 are shown the EPR based ^{1}H NMR shift simulations considering only the contributions arising from the presence of unpaired electrons. Since the shift ranges of experimental ^{1}H NMR shifts lie between -40 to 50 ppm, and we predict a range of possible shifts between 225 and 200 ppm, we do not observe resonances consistent with the experimentally observed hyperfine couplings and, therefore, we conclude that we did not observe any NMR signal from H$_1$.

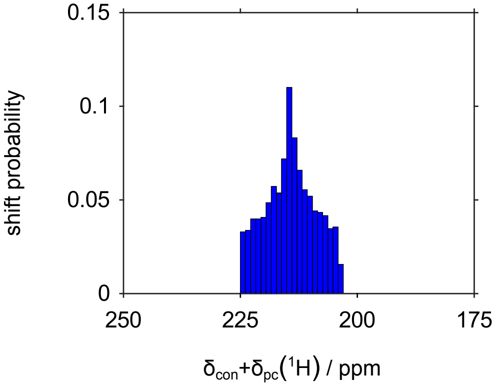

Figure 5.4: ^{1}H NMR shift distributions considering solely the contributions arising from the presence of unpaired electrons and neglecting long-range PCS effects stemming from paramagnetic centers in neighboring unit cells ($\delta_{\text{con}} + \delta_{\text{pcs}}$). The shifts were calculated considering the Moon and Patchkovski [25] and Vaara et al.[13; 26; 125] formalism using the g tensor obtained using multi-reference perturbation theory and the experimental ^{1}H hyperfine tensor. A distribution of relative orientations of the g and A tensors were considered using Zaremba, Conroy, Wolfsberg orientational averaging scheme with 1154 orientations [126–128]. The relative orientation of the z axis of the g and A tensors was kept fixed at 45°, in order to match with the EPR results. Transcribed from paper II.

In order to provide a site-specific assignment of the SiMe$_3$ groups, we calculated the total NMR shift tensors in accordance with equation 2.52 of chapter 2. Combining the computed A and g tensors, the terms $\delta_{\text{con}} + \delta_{\text{pcs}}$ were calculated following the formalism of Moon and Patchkovski [25] and Vaara et al.[13; 26; 125] (see equation 2.40 of chapter 2). The long-range pseudo-contact shifts, $\delta_{\text{pcs,lr}}$ were modeled considering a point-dipole approximation (see equation 2.51 of chapter 2) and, lastly, the orbital terms were calculated at meta-GGA level of theory with the TPSS functional [129]. Additionally, in accordance with the tentative assignment of the experimental data, a 3-site fast exchange model was employed to average the shift tensors both within the methyl groups (along the Si-C$_i$ bonds) and the Me$_3$Si groups (along the C$_1$-Si bond). The total computed shift tensors are summarized in Table 5.2.

Environment		δ_{con}	δ_{pcs}	$\delta_{\text{pcs,lr}}$	δ_{orb}	δ	$\Delta\delta$	η
				SCS-MP2				
^{1}H	Me$_3$Si$_2$ (Calc)	−1.0	6.9	1.0	2.2	9.0	[79.4, 87.0]	[0.6, 0.7]
	(Site II)					30 ± 20	153 ± 1	0.31 ± 0.02
	Me$_3$Si$_1$ (Calc)	−0.1	2.2	0.9	2.0	5.0	[39.5, 41.2]	[0.6, 0.7]
	(Site I)					−20 ± 20	−56 ± 1	0.6 ± 0.1
^{13}C	Me$_3$Si$_2$ (Calc)	−0.2	−4.6	0.9	5.1	1.2	[−103.3, 105.8]	[0.7, 1.0]
	(Site IV)					40 ± 20	−183 ± 4	0.4 ± 0.1
	Me$_3$Si$_1$ (Calc)	−8.7	0.9	0.9	2.0	−4.9	[−51.3, 49.7]	[0.9, 1.0]
	(Site III)					−20 ± 20	140[+30, −270]	0.8 ± 0.3
^{29}Si	Me$_3$Si$_2$ (Calc)	−30.3	−68.2	0.9	−5.6	−103.2	[−237.2, −188.7]	0.3
	(Site V)					−220 ± 30	−542 ± 3	0.74 ± 0.01
	Me$_3$Si$_1$ (Calc)	−47.7	−9.7	−0.8	−2.1	−58.7	[−218.7, 124.7]	[0.3, 0.9]
	(Site VI)					−30 ± 30	409 ± 3	0.51 ± 0.03
				PBE0				
^{1}H	Me$_3$Si$_2$ (Calc)	−0.6	6.7	1.0	2.2	9.2	[79.4, 86.5]	[0.6, 0.7]
	(Site II)					30 ± 20	153 ± 1	0.31 ± 0.02
	Me$_3$Si$_1$ (Calc)	0.1	2.1	0.9	2.0	5.1	[38.9, 40.8]	[0.6, 0.7]
	(Site I)					−20 ± 20	−56 ± 1	0.6 ± 0.1
^{13}C	Me$_3$Si$_2$ (Calc)	26.2	−7.8	0.9	5.1	24.5	[91.8, 147.2]	[0.2, 1.0]
	(Site IV)					40 ± 20	−183 ± 4	0.4 ± 0.1
	Me$_3$Si$_1$ (Calc)	17.6	−0.3	0.9	2.0	20.2	[49.6, 109.6]	[0.1, 1.0]
	(Site III)					−20 ± 20	140[+30, −270]	0.8 ± 0.3
^{29}Si	Me$_3$Si$_2$ (Calc)	−74.0	−64.0	0.9	−5.6	−142.7	[−360.4, −171.3]	[0.2, 0.5]
	(Site V)					−220 ± 30	−542 ± 3	0.74 ± 0.01
	Me$_3$Si$_1$ (Calc)	−69.6	−9.3	0.9	−2.1	−80.3	[−305.6, 112.3]	[0.2, 0.8]
	(Site VI)					−30 ± 30	409 ± 3	0.51 ± 0.03

Table 5.2: Calculated and experimental SA parameters for the proximal (Me$_3$Si$_2$) and distal (Me$_3$Si$_1$) Me$_3$Si groups of Yb[CH(SiMe$_3$)$_2$]$_3$ in the Haeberlen convention [14] (experimental spectra are shown in 5.2). The calculated SAs were decomposed according to equations 2.52 and 2.40 of chapter 2. Hyperfine tensor calculated at SCS-MP2 and PBE0 level of theory, orbital chemical shifts with TPSS meta-GGA functional and g tensor with multi-reference perturbation theory (CASSCF+NEVPT2). ^{13}C and ^{1}H tensors of Me$_3$Si groups were averaged both within the methyl groups (along the Si-C$_i$ bonds) and the Me$_3$Si groups (along the C$_1$-Si bond). Isotropic shifts were averaged between the three different SiMe$_3$ groups, which due to small deviations of C$_3$ symmetry in the optimized geometry result in different SA tensors. These deviations also account for the range of anisotropies $\Delta\delta$ and asymmetry η parameters. Adapted from paper II.

We note that there are quantitative discrepancies between the experimental and computed shift tensor values. This is likely a result of the shortcomings in calculation methods for the Fermi contact term, the complexity of the Yb electronic structure [130], the neglect of the spin-orbit contributions to the hyperfine tensor, and the simplified nature of our dynamic hopping model. We note, however, that consistent trends in the shift anisotropy parameters were observed when considering the hyperfine tensor calculated at both SCS-MP2 and hybrid DFT level of theory. Furthermore, in spite of these discrepancies, we observe that the magnitude of the shifts and shift anisotropies for the nuclear species from the proximal Me$_3$Si$_2$ group are larger than those from the distal Me$_3$Si$_1$ group, which for Si is a straightforward consequence of the distance to Yb. A pictorial representation of these computed silica tensors superimposed to the DFT-optimized structure is shown in Figure 5.5.

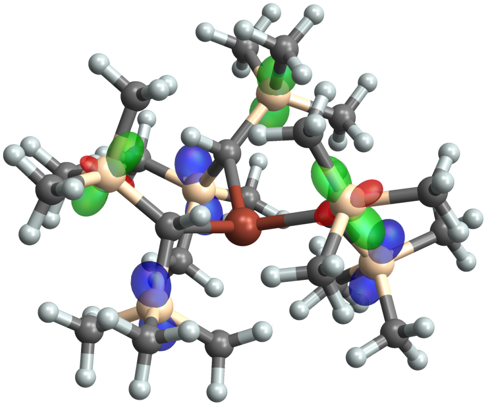

Figure 5.5: DFT-optimized structure of Yb(CH(SiMe$_3$)$_2$)$_3$ complex overlapped with ovaloid surface representation of the ^{29}Si NMR tensors in shift convention (proximal Me$_3$Si groups colored in green/red and distal Me$_3$Si groups in blue/yellow) [131]. The radius from the center of the tensor to a point on the ovaloid surface is proportional to the chemical shift when the magnetic field is aligned along that direction in space and the sign of the shift is indicated by the color of the surface, red/yellow corresponds to positive shift and green/blue to a negative shift. Transcribed from paper II.

In this chapter we have thus shown that only via a combination of X-ray crystallography, solid-state NMR using broadband methods tailored for paramagnetic systems, EPR, magnetic studies and state-of-the-art quantum chemical calculations we were able to accurately describe the electronic configuration and bonding motifs of Yb[CH(SiMe$_3$)$_2$]$_3$, highlighting the complementary nature of these techniques.

6

Extraction of NMR Parameters of Half-Integer Quadrupolar Nuclei in Paramagnetic Systems

Up to now, in spite of quadrupolar nuclei being very common in the periodic table, our entire discussion has been focused on spin 1/2 nuclei and shift interactions. The main reason for this is that quadrupolar nuclei are often perceived as cumbersome and, therefore, not as widely studied as their spin 1/2 counterparts, since their spectra, in most cases, are dominated by the quadrupolar interaction [8]. Moreover, for half-integer systems we have the additional difficulty of differentiating between the central transition of different environments and their accompanying satellite transitions. Similarly to the hyperfine interaction, the quadrupolar parameters have a close link with crystal symmetry, local environment and dynamics, which, in turn, also makes it a valuable source of information [8].

In the limit of small quadrupolar interactions, such as the case of ^{7}Li due to its small quadrupolar moment, half-integer quadrupolar nuclei essentially behave like spin 1/2 nuclei and the plethora of methods developed specifically for them can also be employed for quadrupolar nuclei. As an example, in our studies in paper D, the ^{23}Na ($I = 3/2$) environments observed in the electrochemical cycling of sodium inserted Bi_2Te_3, all exhibited small quadrupolar couplings resulting in lineshapes similar to spin 1/2 nuclei.

On the other hand, the quadrupolar interaction may be so large, normally in heavy nuclei, that the sample spinning does not exceed the broadening induced by the second-order quadrupolar interaction, which is not removed by MAS, and it overlaps with the spinning sidebands, leading to complicated spectra. In this limit, it is often easier to acquire the spectra under static conditions. In paper E, we demonstrate how DFT-assisted static ^{115}In (I=9/2) can be an effective tool for the study of indium (III) complexes.

For moderate quadrupolar couplings, spinning frequencies larger than the width of second-order induced broadening are normally possible with current probe technology. In this way, MAS is beneficial since it leads to clearer lineshapes and, hence, higher accuracy of extracted NMR parameters. However, to achieve high-resolution spectra when probing half-integer quadrupolar nuclei in conventional MAS probes the use of the Multiple Quantum (MQ) MAS experiment, originally proposed by Frydman and Harwood [132], or its rival experiment the Satellite Transition (ST) MAS , proposed by Gan [133] is required. Both experiments yield high-resolution spectra via two-dimensional experiments, by correlating either multiple quantum or satellite transitions, respectively, with the central transition.

For paramagnetic systems, the presence of moderate-to-large quadrupolar interactions in conjunction with large paramagnetic shift anisotropies and BMS effects complicates the interpretation of NMR spectra even further, which is why method development has lagged behind. For integer quadrupolar systems, notable schemes have been proposed, such as the application of the Delays Alternating with Nutation for Tailored Excitation (DANTE) [134] to achieve broadband inversion and excitation, and the low-power excitation of double-quantum coherences [135] to improve resolution. Pulse sequences designed for the separation of shift and quadrupolar interaction have also been proposed, for static samples the shifting *p*-echo [136], shifting *d*-echo [137], adiabatic shifting *d*-echo, paper C, and, more recently, phase adjusted spinning sideband (PASS) [138] for spinning samples. For half-integer quadrupoles, the applicable methods are still relatively limited. In this chapter we will discuss the work carried out towards the development of state-of-the-art methods for extraction of both half-integer quadrupolar paramagnetic systems, based on papers III and IV.

6.1 RAPT

Half-integer spin quadrupolar nuclei typically give spectra where the satellite transitions, due to the contribution of the first-order quadrupole, are extremely broad while the CTs are relatively sharp. For this reason, when probing half-integer quadradrupolar nuclei usually low-power RF excitation pulses are employed which causes the STs to have a negligible contribution to the spectra. In paramagnetic systems, however, due to the large SAs, higher RF powers are required for excitation. In spite of this, even the highest practicable RF powers typically still result in pulses operating at the CT-selective regime. One less desirable consequence of employing CT-selective pulses is the lower signal-to-noise ratio, given that the population difference in spin population of the two states connected by the CT results in a lower excited polarization that would otherwise be available if we would consider all the STs as well, as shown in figure 6.1(a).

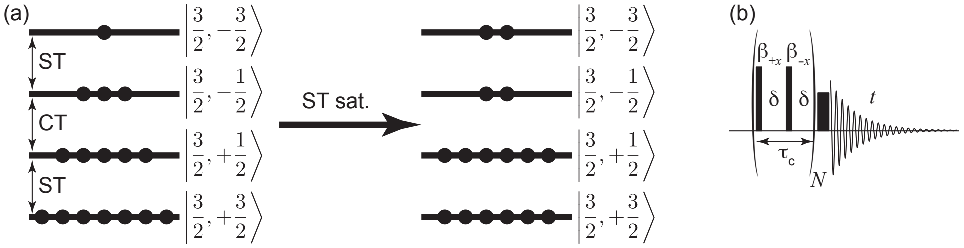
(a)
ST
CT
ST
$\left|\frac{3}{2},-\frac{3}{2}\right\rangle$
$\left|\frac{3}{2},-\frac{1}{2}\right\rangle$
$\left|\frac{3}{2},+\frac{1}{2}\right\rangle$
$\left|\frac{3}{2},+\frac{3}{2}\right\rangle$
ST sat.
(b)
β+x
β−x
δ
δ
t
τc
N

Figure 6.1: RAPT sequence for enhancing the signal from the CT of a half-integer-spin quadrupolar nucleus [139], reproduced from [11], with permission from Elsevier. The effect of ST saturation is demonstrated on the nuclear-spin energy level diagrams for a spin $I = 3/2$ in (a) where the saturation of the two STs leads to the simultaneous removal of the ST polarization and enhancement of the CT polarization. The RAPT pulse sequence is shown in (b). The saturation period with total length τ_c, comprising of a pair of pulses with flip angle β and alternating phases $+x$ and $-x$, that is repeated N times. The final pulse is a CT-selective [140], low-power pulse calibrated to deliver a 90° rotation to the CT polarization.

One way of overcoming this limitation is to saturate the population of the satellite transitions so that its net polarization is reduced to zero, which, in turn, has the effect of increasing the polarization of the CT by a factor of $I+1/2$ (see figure 6.1). This saturation can be carried out via the Rotor-Assisted Population Transfer (RAPT) [139] shown in figure 6.1(b), where a CT-selective excitation pulse is preceded by a train of N pairs of β_x β_{-x} RF pulses separated by a short delay δ. Prasad et al. [141] has demonstrated that the optimal value of the cycle time $\tau_c = 2\tau_x + 2\delta$, where τ_x is pulse duration, is given by

$$\tau_c = \frac{2\pi}{\omega_q} \tag{6.1}$$

and is independent of η_q [141] and hence provides a relatively straightforward method of determining C_q that is particularly useful for paramagnetic systems where the ABMS induced broadening may impede the extraction the quadrupolar parameters via the analysis of the quadrupolar lineshapes [142].

In our work in paper III, where we explored the structurally complex $NaMnO_2$, we employed RAPT trains to enhance the the signal-to-noise ratio and suppress the contribution of the satellite transitions of spin-echo and MAT experiments, as shown in figure 6.2. The MAT experiment permitted the identification of six distinct resonances, which in turn permitted a thorough analysis of the RAPT buildup extracting the enhancement factor for each individual site, as shown in figure 6.3.

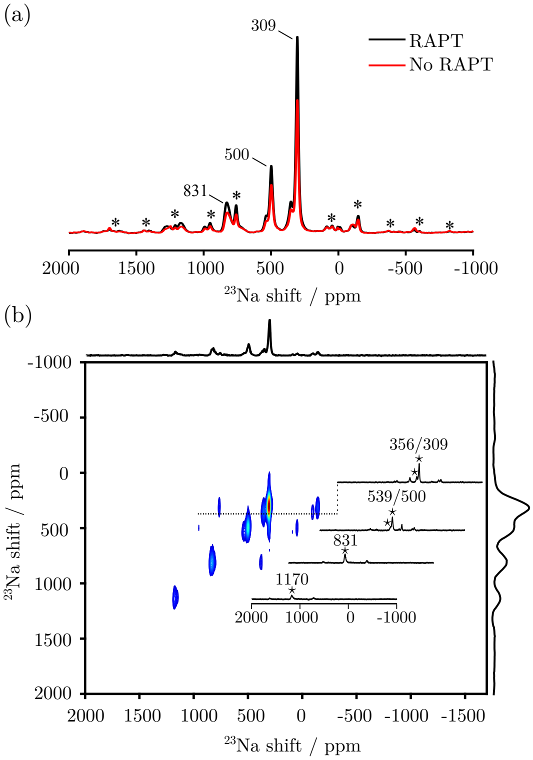

Figure 6.2: RAPT-enhanced ^{23}Na solid-state NMR spectra of $NaMnO_2$, transcribed from III. (a) One-dimensional Hahn-echo spectrum of $NaMnO_2$ with and without the application of a RAPT train illustrating the enhancement of the signal intensity of the central transition by approximately a factor of 1.4. Observed centerbands and sidebands marked with by stars ($\star$) and asterisks ($*$), respectively. (b) MAT spectrum of $NaMnO_2$ exhibiting six resonances with distinct observed shifts. Inset spectra correspond to extracted direct-dimension slices, and the observed shifts correspond to the centerbands marked by stars ($\star$). RAPT pulses were applied before the MAT experiment to enhance the signal-to-noise ratio and suppress the signals arising from the satellite transitions. Both spectra were recorded at 60 kHz MAS and at an 11.7 T external magnetic field. RAPT pulse trains were employed with a repetition frequency of 525 kHz.

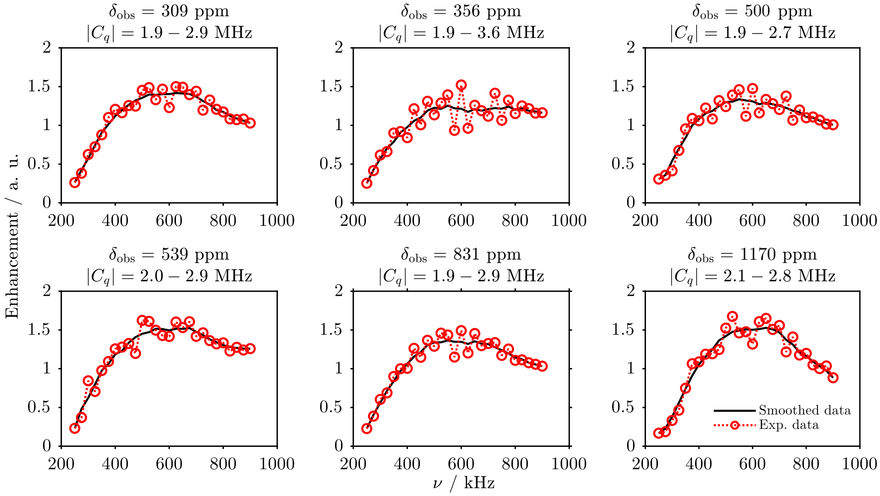

Figure 6.3: RAPT-enhancements for the six ^{23}Na resonances extracted from the MAT spectra with increasing repetition frequency of the RAPT pulses, transcribed from paper III. The data points are indicated by red circles. The smooth black curves were obtained by employing a moving-average filter and were used to estimate the maximum enhancement factor. Considering a frequency interval corresponding to ±5% of the maximum enhancement factor and using equation (6.1), the range of magnitudes of the quadrupolar couplings $|C_q|$ was determined.

6.2 MQMAS/STMAS

In the case of overlapping resonances, the analysis of the RAPT buildup is no longer a well-posed problem since it is difficult to discern the contribution of each site. Furthermore, high-resolution spectra are often necessary for a complete structural determination. The MQMAS and STMAS sequences are designed to achieve precisely that via a two-dimensional experiment. In order to explain both methods let us define the reduced spin tensor operator $\hat{t}_{\lambda,0}$ of order λ, given by

$$\hat{t}_{00} = \hat{\mathbb{1}}, \tag{6.2}$$

$$\hat{t}_{10} = \hat{I}_z, \tag{6.3}$$

$$\hat{t}_{20} = \hat{I}_z^2 - \frac{1}{3}I(I+1)\hat{\mathbb{1}}, \tag{6.4}$$

$$\hat{t}_{30} = \frac{1}{3}\left\{5\hat{I}_z^3 - [3I(I+1)-1]\hat{I}_z\right\}. \tag{6.5}$$

As discussed in chapter 2, the NMR Hamiltonian $\hat{H}$ defines the frequency of transition between the nuclear spin states $|m_i\rangle$ and $|m_j\rangle$. This frequency depends on the spatial properties of the interaction via the shielding and EFG terms, and on the spin properties via the spin orders Ξ_{λ,M_i,M_j} of rank λ for the transitions between $|m_j\rangle$ and $|m_i\rangle$ [143]:

$$\Xi_{\lambda,M_i,M_j} = \langle M_i|\hat{t}_{\lambda,0}|M_i\rangle - \langle M_j|\hat{t}_{\lambda,0}|M_j\rangle. \tag{6.6}$$

Following Grandinetti et al. [143] we define the different spin orders as $s_{M_i,M_j} = \Xi_{0,M_i,M_j}$, $p_{M_i,M_j} = \Xi_{1,M_i,M_j}$ which are also known as coherence order which defines the coherence transfer pathways (CTPs) that are fundamental concept in signal selection in multiple-pulse NMR experiment [144], $d_{M_i,M_j} = \Xi_{2,M_i,M_j}$ and $f_{M_i,M_j} = \Xi_{3,M_i,M_j}$. For the second-order quadrupolar interaction, where the spatial ranks of 0, 2 and 4 are associated with spin orders of rank 1 and 3, it is more convenient to define the C-order parameters $C^{(0)}$, $C^{(2)}$ and $C^{(4)}$ as follows:

$$C^{(0)}_{M_i,M_J} = \frac{9}{5} f_{M_i,M_j} + \frac{4I(I+1)-3}{5} p_{M_i,M_j}, \tag{6.7}$$

$$C^{(2)}_{M_i,M_J} = -\frac{18}{5} f_{M_i,M_j} + \frac{4I(I+1)-3}{10} p_{M_i,M_j}, \tag{6.8}$$

$$C^{(4)}_{M_i,M_J} = -\frac{51}{5} f_{M_i,M_j} + \frac{3[4I(I+1)-3]}{10} p_{M_i,M_j}. \tag{6.9}$$

The frequencies of the transitions due to the chemical shift Ω_{CS}, first and second-order quadrupolar $\Omega_Q^{(1)}$ and $\Omega_Q^{(2)}$ interaction are therefore given by:

$$\Omega_{\text{CS}}(\Omega_{\text{SC}},\Omega_{\text{CR}},M_i,M_j) = \Upsilon^{\text{CS}}_{0,0}\cdot p_{M_i,M_j} + \Upsilon^{\text{CS}}_{2,0}(\Omega_{\text{SC}},\Omega_{\text{CR}})\cdot p_{M_i,M_j}, \tag{6.10}$$

$$\Omega_Q^{(1)}(\Omega_{\text{QC}},\Omega_{\text{CR}},M_i,M_j) = \Upsilon^{Q^{(1)}}_{2,0}(\Omega_{\text{QC}},\Omega_{\text{CR}})\cdot d_{M_i,M_j}, \tag{6.11}$$

$$\begin{aligned}\Omega_Q^{(2)}(\Omega_{\text{QC}},\Omega_{\text{CR}},M_i,M_j) &= \Upsilon^{Q^{(2)}}_{0,0}\cdot C^{(0)}_{M_i,M_j} \\ &\quad + \Upsilon^{Q^{(2)}}_{2,0}(\Omega_{\text{QC}},\Omega_{\text{CR}})\cdot C^{(2)}_{M_i,M_j} + \Upsilon^{Q^{(2)}}_{4,0}(\Omega_{\text{QC}},\Omega_{\text{CR}})\cdot C^{(4)}_{M_i,M_j},\end{aligned} \tag{6.12}$$

where $\Upsilon^{\text{CS}}_{0,0}$, $\Upsilon^{\text{CS}}_{2,0}$ are isotropic, rank-0, and anisotropic, rank-2, spatial dependencies of the CSA, $\Upsilon^{Q^{(1)}}_{2,0}$ accounts for the rank-2 spatial anisotropy of the first-order quadrupole, and the terms $\Upsilon^{Q^{(2)}}_{x,0}$, where $x = (0,2,4)$, represent the isotropic and anisotropic spatial parts of ranks 2 and 4, of the second-order quadrupolar interaction.

The MQMAS and STMAS experiments achieve high-resolution by removal of the second-order quadrupolar-induced broadening due to the rank-4 contribution via a $C^{(4)}$ echo [143]. The pulse sequence used for both experiments is shown in 6.4(a). During t_1 evolution, the transition pathway passes through a single quantum ST or through a symmetric $(|-m\rangle \leftrightarrow |m\rangle)$ MQ transition (here 3Q), for STMAS and MQMAS, respectively and ends on the single quantum CT during t_2. For both experiments, the recorded two-dimensional time-domain signal for both the N-type and P-type pathways is given by

$$\begin{aligned}S(t_1,t_2) = &\exp\left[i\left(\Upsilon^{\text{CS}}_{0,0}\cdot p_{M_i,M_j} + \Upsilon^{Q^{(2)}}_{0,0}\cdot C^{(0)}_{M_i,M_j} + \Upsilon^{Q^{(2)}}_{4,0}\cdot C^{(4)}_{M_i,M_j}\right)t_1\right] \\ &\cdot\exp\left[i\left(-\Upsilon^{\text{CS}}_{0,0} + \Upsilon^{Q^{(2)}}_{0,0}\cdot C^{(0)}_{-1/2,+1/2} + \Upsilon^{Q^{(2)}}_{4,0}\cdot C^{(4)}_{-1/2,+1/2}\right)t_2\right],\end{aligned} \tag{6.13}$$

where $p_{-1/2,+1/2} = -1$ and, for convenience, we have only included the time-independent components of the signal. Here, m_i and m_j have values pertaining either to the MQ or ST, as required. As a consequence of rotor synchronization of the sampling interval in t_1, the time-dependent terms are refocused by MAS in this dimension. It is also worth noting that, since the multiple quantum transition is symmetric, $d_{M_i,-M_i} = 0$, for MQMAS the contribution of the first-order quadrupolar interaction vanishes. This result also holds true for the CT transition in t_2 provided that the last pulse is CT selective. Due to the fact that the $C^{(4)}$ echo is not simultaneous with the p echo, only by applying a shearing and scaling transformation parallel to t_2 is it possible to construct a 2D time-domain signal where $\Upsilon^{Q^{(2)}}_{4,0}$ does not evolve in (*i.e.*, is refocused along) t_1', as shown in figure 6.4 (a) for STMAS and (b) for MQMAS, employing the triple-quantum transition.

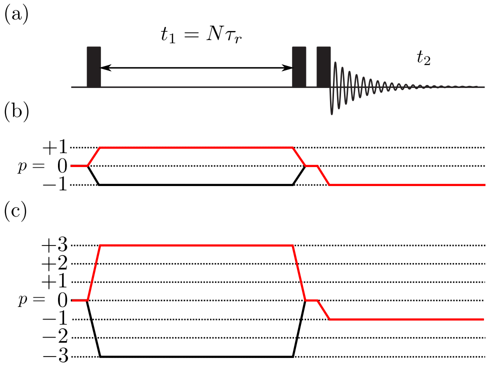

Figure 6.4: Pulse sequences and CTPs for the z-filtered STMAS, figure (a), and MQMAS experiments, figure (b). The pulse sequence shown in (a) is used for acquiring both phase-sensitive STMAS and MQMAS spectra with different pulse parameters. The CPT for STMAS is shown in (b) and the CPT for MQMAS is given in (c). Red and black pathways correspond to the N-type and P-type datasets, respectively. Transcribed from paper IV.

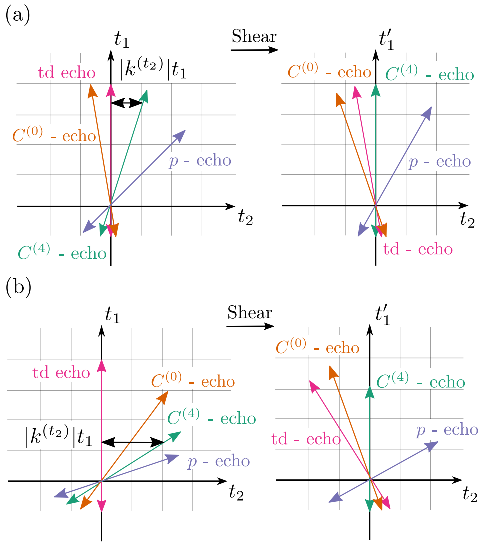

Figure 6.5: Representation of the STMAS (a) and MQMAS (b) time-domains before and after the application of a conventional shear and scale transformation, where $k^{(t_2)}$ represents the shear ratio. The time-independent rank-0 and rank-4 terms of the second-order quadrupolar interaction along with the isotropic chemical shift that are refocused along the $C^{(0)}$, $C^{(4)}$ and p echo lines, respectively. The time domain (td) echo ridge accounting for the chemical shift anisotropy and quadrupolar interactions are shown as well. After the conventional affine transformation the interactions represented by $C^{(4)}$ are refocused along t'_1. Transcribed from paper IV.

6.2.1 TOP-STMAS/MQMAS

The STMAS/MQMAS time-domain data, when processed as shown in figure 6.5, does not separate the chemical shift and the rank-4 quadrupolar lineshape into orthogonal dimensions and, hence, does not remove the quadrupolar interference of the ABMS broadening from the quadrupolar lineshapes. Additionally, due to rotor synchronization in t_1, the spectral window may not be sufficiently large to accommodate the chemical shift dispersion, especially for paramagnetic systems. Peaks that lie outside the spectral window are folded, or aliased back into the spectral window which further complicates their analysis. Both the limitations of the inhomogeneous BMS broadening and the spectral window in ω_1 can be addressed via a double shearing transformation similar to the scheme proposed in for TOP [145–149], pure shift NMR in solution [150] and COASTER [151]. After this transformation a new (t'_1, t'_2) 2D time domain system where the frequency terms that depend on p do not evolve in t'_1 is constructed, which eliminates the BMS broadening and shift in ω'_1 and instead transfers them to ω'_2 where we can benefit from the large spectral window of the directly acquired dimension, analogously to TOP processing [145–147], as demonstrated by Walder et al. [148] and Paruzzo et al. [149].

Figure 6.6 gives a visual outline of the double shearing transformation applied to a simulated system of three independent spin 5/2 sites affected by BMS, in both time- (figures 6.6(a)-(f)) and frequency-domains (figures 6.6(g)-(i)). After the first shear transformation along t_2 (figures 6.6(b), (e) and (h)) with a shear ratio $k^{(t_2)}$, a new t_1' dimension is created along which the evolution of the BMS broadening and shift are refocused and, consequentially, the folding/aliasing in ω_1, arising due to the large chemical shift dispersion, is also removed. The second shear transformation (figures 6.6(c), (f) and (i)), now parallel to t_1' with shear ratio $k^{(t_1)}$, removes the quadrupolar broadening from t_2' and ω_2, yielding pure quadrupolar and pure shift dimensions.

An expansion of the processed spectra around the resonances of each simulated site is shown in figures 6.6(j)-(k), highlighting how the double shearing transformation greatly facilitates the spectral interpretation and potential extraction of both shift and quadrupolar parameters. It is also worth noting that as in any conventional STMAS spectra, in addition to the the cross-peak arising from the correlation of first ST (ST_1) with the CT, the correlation ridges of CT and second ST (ST_2) with the CT are visible, since they cannot be filtered out via phase-cycling. Kwak and Gan [152] have proposed a method of removing these additional correlations via a double-quantum filter. Since this methods does not alter the ST_1-CT correlation the same double shearing transformation can be employed to separate the shift and quadrupolar interactions.

An analogous double shearing transformation can also be applied to MQMAS spectra, albeit with modified shearing coefficients, to separate the shift and quadrupolar interactions. However, in spite of its popularity for diamagnetic systems, MQMAS has not been widely successfully applied to paramagnetic systems, likely due to the interference between paramagnetic and quadrupolar effects.

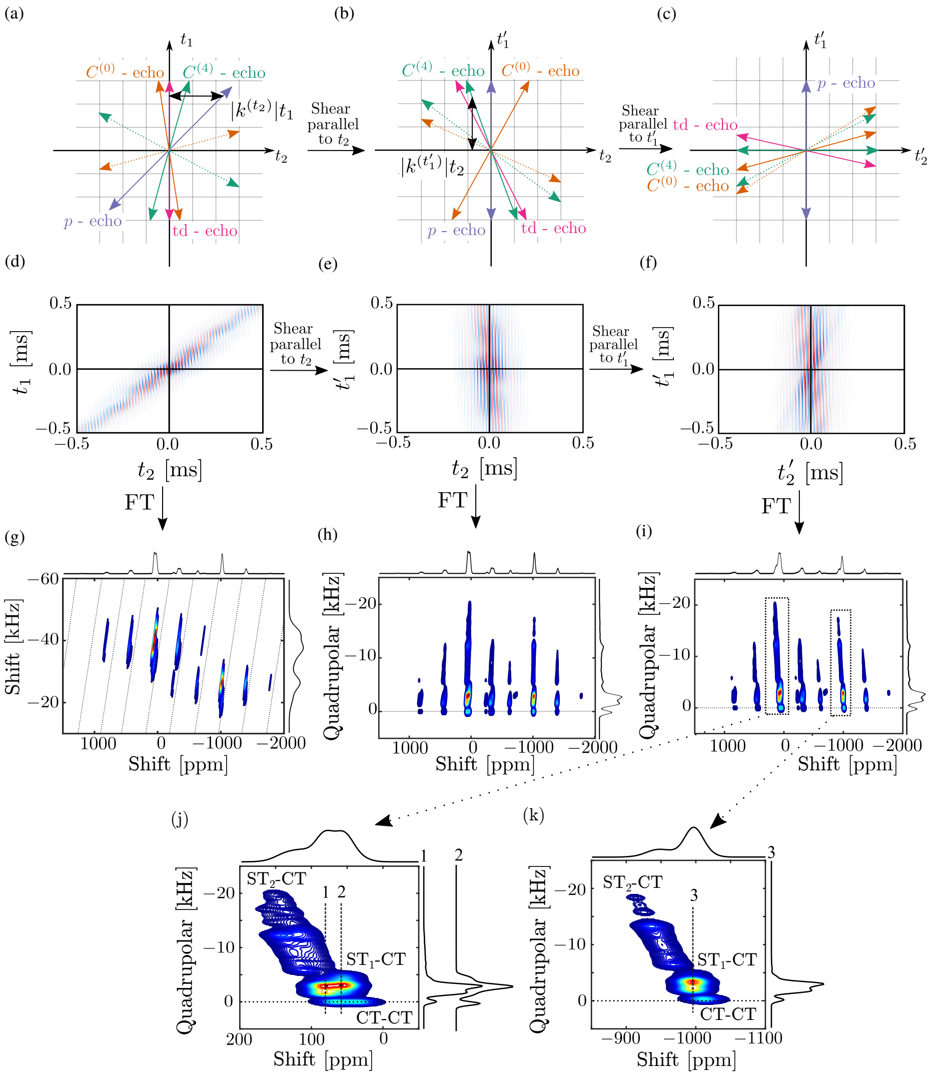

Figure 6.6: Simulation of a z-filtered STMAS spectrum with rotor-synchronized indirect dimension t_1, for a system comprising three independent spins 5/2. In (a)-(c)the different echo ridges are shown for the first (solid lines) and second satellites (dashed lines). The echo CT ridge, as opposed to the satellites, lies along the p ridge. In (d)-(f) and (g)-(i) the corresponding signals are shown in the time and frequency domains, respectively. In (g)-(i) the main diagonal $\omega_1 = \omega_2$ is indicated by the dotted line. After the first shear transformation, the t'_1 and ω'_1 dimensions contain no shift components (p) from the first satellites and, likewise, after the second transformation, the t'_2 and ω'_2 dimensions contain no quadrupolar broadening ($C^{(4)}$), from the first satellites as well. In figures (j) and (k) expansions of the centerband of each spin resonance of the double sheared spectrum (i) are shown. Transcribed from paper IV.

In figure 6.7 we show the application of this method on the $NaMnO_2$ system, from paper III. The $NaMnO_2$ ^{23}Na spectrum shown in figure 6.2 does not exhibit the features characteristic of a quadrupolar lineshape. This is likely a consequence of structural disorder, which causes its local environments to exhibit a distribution of quadrupolar parameters and, consequentially, quadrupolar induced shifts, which result in broadening of the lineshape. Broadening effects arising from PRE are also expected to play a significant role. Nevertheless, by fitting the extracted slices for the two observed sites marked with dashed lines with Gauss-Lorentz functions, we can extract the centers-of-gravity and calculate both isotropic shift and quadrupolar products. Combining the information extracted via TOP-STMAS with the RAPT buildups and MAT spectrum, the shift and quadrupolar parameters were obtained and the different resonances quantified. Very good agreement between extracted NMR parameters and the calculations reported in Clement et al. [153] was obtained, thus validating the proposed model therein.

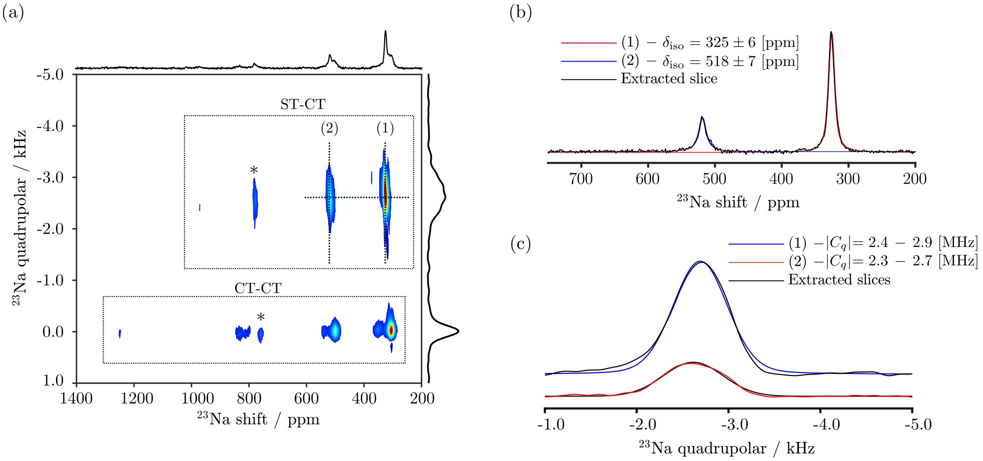

Figure 6.7: (a) Sheared z -Filtered TOP-STMAS spectrum showing the CT-CT diagonal peaks of five observed resonances, around 0 kHz in the indirect dimension and the Satellite Transition (ST)-CT diagonal peak for the sites whose central transition is observed at 309 and 500 ppm, at around −2.6 kHz in the indirect dimension. Sidebands are marked with ($\star$). Extracted slices along the shift and quadrupolar dimensions together with the best fits are shown in figures (b) and (c), respectively. The spectral lineshapes were all simulated considering Gauss-Lorentz curves whose centers-of-gravity were used to determine the quadrupolar products and isotropic shifts. The STMAS spectrum was recorded while spinning at 60 kHz MAS and at 11.7 T. Transcribed from paper IV.

In paper IV, a series of lanthanide (Ln) doped yttrium aluminum garnets (YAGs) were investigated via ssNMR. For the undoped phase, the NMR spectrum comprises both a sharp and a relatively broad signal arising from six coordinate AlO_6 environments with smaller C_q, and four coordinate AlO_4 environments, with larger C_q.

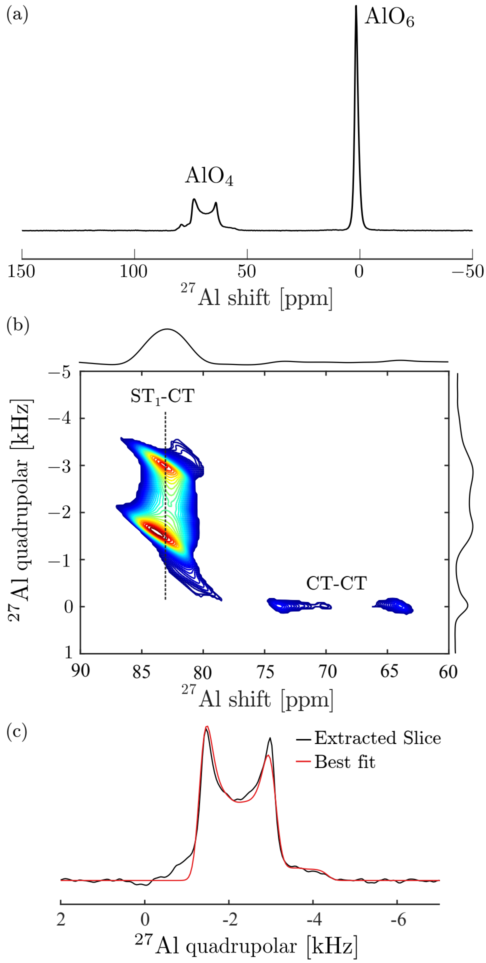

Figure 6.8: (a) ^{27}Al solid-state NMR spectrum of pristine YAG where two signals arising from the AlO_4 and the AlO_6 are clearly distinguishable. (b) *z*-Filtered TOP-STMAS spectrum indicating the CT-ST$_1$ correlation cross-peak and the CT-CT diagonal peak, of lower intensity. In (c) the extracted slice is shown together with the best fit chemical shift and quadrupolar interaction parameters determined experimentally. Both spectra were acquired at 14.1 T and 60 kHz MAS. Adapted from paper IV.

In figures 6.9(a)-(b) and 6.10(a)-(b) the spectra of Nd, Eu, Tb and Yb doped YAGs are shown. The spectra are primarily dominated by the features of the bulk AlO_4 and AlO_6 sites that are remote from the lanthanide ion and similar to the undoped YAG. However, multiple lower-intensity peaks arising from the presence of paramagnatic dopants in the first Ln-Y coordination shell, can also be observed. For the sharper AlO_6 sites, we can ascribe these resonances to the presence of one and two Ln ions in the first Ln-Y coordination shell, since the contributions to the total shift from the Ln ions are approximately additive and that the distance between two shifted AlO_6 sites and the bulk AlO_6 and the closest shifted site is approximately the same.

Employing the TOP-STMAS method we were able to extract the quadrupolar parameters of the AlO_4 sites, as shown in figures 6.8(b)-(c), 6.9(c)-(f)), 6.10(c)-(f), and table 6.1. The quadrupolar coupling parameters for both paramagnetically shifted and bulk unshifted sites do not vary significantly with the introduction of different Ln ions and are all similar to the quadrupolar parameters of the pristine material. This result suggests that the local environments are not highly distorted, which further corroborates the rigidity of the YAG host lattice, crucial to its optical properties, also evidenced by DFT calculations.

Lastly we also note that the TOP-STMAS method, using the double-quantum filter STMAS[152] experiment, was also successfully applied on a diamagnetic ZnNa2-based metal-organic framework loaded with ibuprofen exhibiting structural disorder (see paper F).

We expect the methodologies presented in this chapter to provide a blueprint for the study of half-integer quadrupolar nuclei in paramagnetic systems, and inspire new advances in the field solid-state PNMR.

		δ_{iso} [ppm]	C_q [MHz]	η
		Undoped YAG		
TOP-STMAS		77.3 ± 0.4	6.0 ± 0.1	0.06 ± 0.05
Florian et al. [154]		78 ± 1	6.15 ± 0.07	0.05 ± 0.05
Vosegaard et al.[155]		81.5 ± 0.4	6.103 ± 0.009	0.006 ± 0.002
		Ln:YAG bulk AlO_4 resonances		
TOP-STMAS	Nd:YAG	78 ± 1	5.8 ± 0.6	0.3 ± 0.1
	Eu:YAG	78 ± 2	6.0 ± 0.6	0.2 ± 0.1
	Tb:YAG	78 ± 2	6.6 ± 0.7	0.6 ± 0.2
	Yb:YAG	78 ± 3	7.0 ± 0.8	0.2 ± 0.1
		Ln:YAG shifted AlO_4 resonances		
TOP-STMAS	Nd:YAG	51 ± 2	6.2 ± 0.6	0.3 ± 0.1
	Eu:YAG	123 ± 4	6.3 ± 0.5	0.1 ± 0.2
	Yb:YAG	132 ± 3	7.0 ± 0.8	0.3 ± 0.1

Table 6.1: Extracted experimental ^{27}Al isotropic shift and quadrupolar interaction parameters of the four coordinated sites in both undoped and Ln doped YAGs. The isotropic shift and quadrupolar interaction parameters for the undoped YAG reported in Florian et al. [154] and Vosegaard et al.[155] were also included for comparison. Adapted from paper IV.

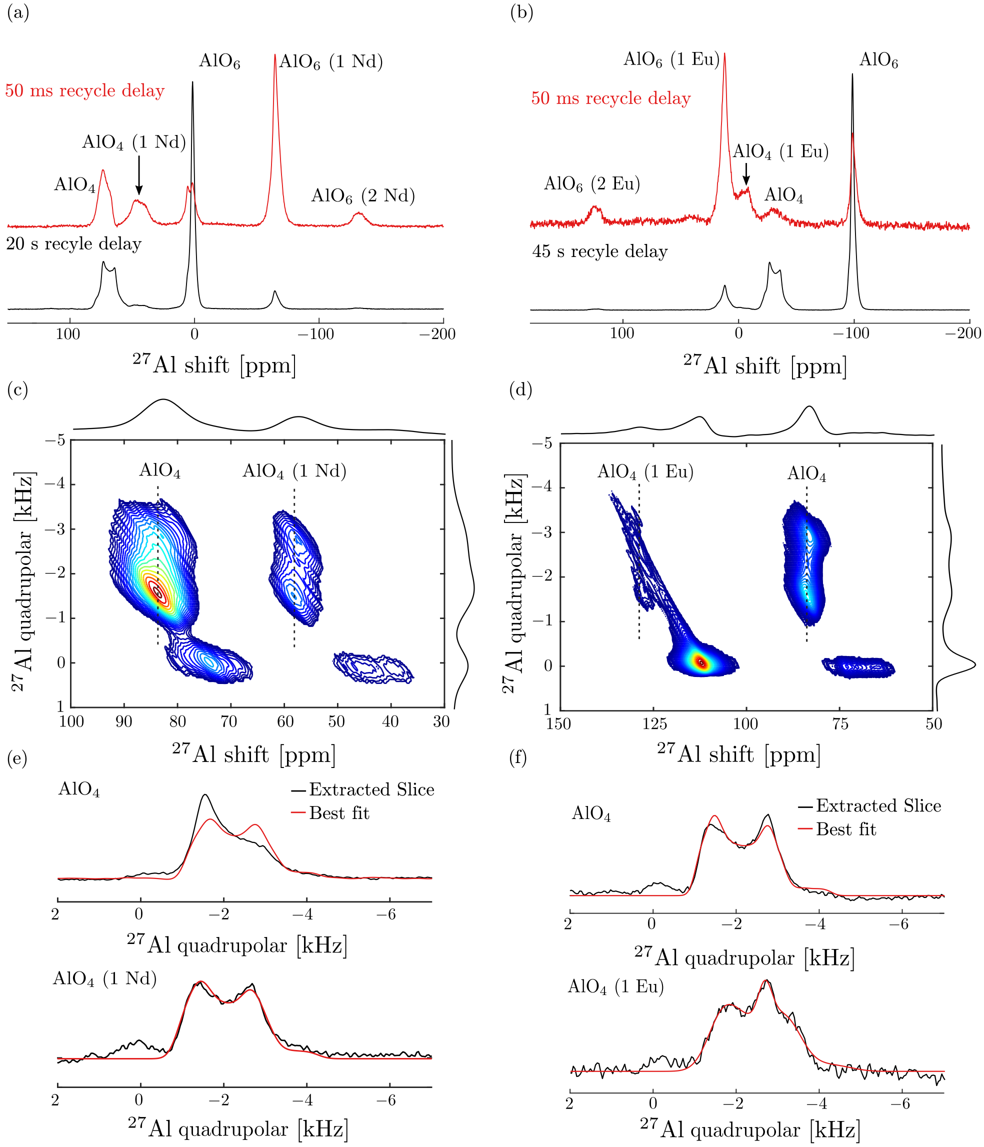

Figure 6.9: (a) Nd:YAG and (b) Eu:YAG ^{27}Al NMR spectrum. Shifted resonances arising from the presence of one and two Ln ions in the first Ln-Y coordination shell are denoted with (1 Nd/Eu) and (2 Nd/Eu), respectively. (c) and (d) Sheared z-filtered TOP-STMAS ^{27}Al spectra together with extracted slices and best fits of the quadrupolar dimension (e)-(f) of Nd and Eu, respectively. The shifted Eu:YAG was fitted with an additional Gaussian lineshape to account for the contributions from the CT autocorrelation that affects the quadrupolar lineshape. All spectra were acquired at 14.1 T, 60 kHz spinning speed. Transcribed from paper IV.

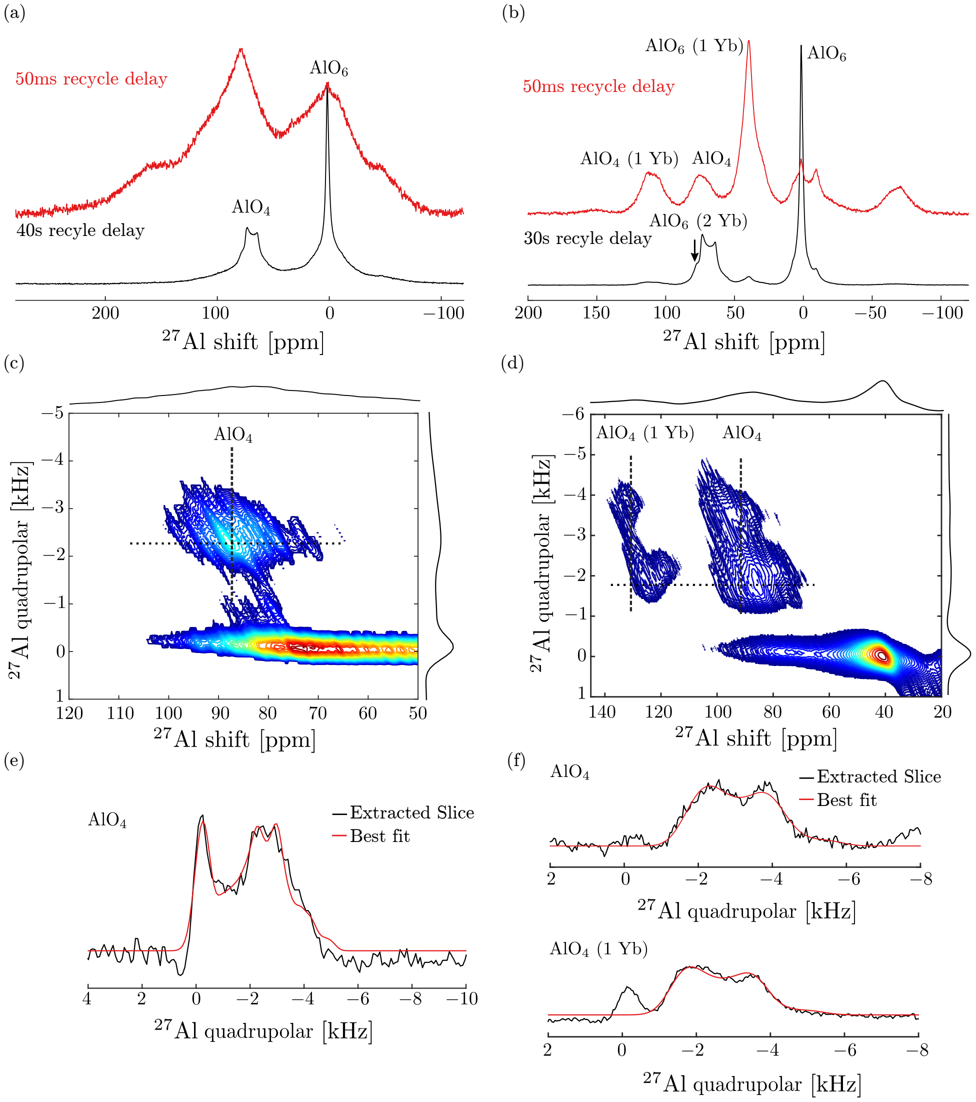

Figure 6.10: (a) Nd:YAG and (b) Eu:YAG ^{27}Al NMR spectrum. Shifted resonances arising from the presence of one and two Yb ions in the first Yb-Y coordination shell are denoted with (1 Yb) and (2 Yb), respectively. (c) and (d) *z*-filtered TOP-STMAS ^{27}Al spectra together with extracted slices and best fits of the quadrupolar dimension (e)-(f) of Tb and Yb, respectively. Horizontal dotted line in (c) and (d) correspond to slices extracted of the shift. The shifted Tb:YAG was fitted with an additional Gaussian lineshape to account for the contributions from the CT autocorrelation that affects the quadrupolar lineshape. All spectra were acquired at 14.1 T, 60 kHz spinning speed. Transcribed from paper IV.

7

Summary

In recent years, substantial progress has been made in the field of paramagnetic nuclear magnetic resonance (NMR), both in the development of the theory and methods. Moreover, specifically in solid-state NMR, the variety of systems being routinely studied today is quite diverse, ranging from battery materials, metalloproteins, heterogeneous catalysts and inorganic phosphors. The work carried out in this thesis contributes to the latest advances in this field by addressing some less developed areas.

Firstly, by using a combination of simulations and experiments we presented a complete unified description of the different frameworks to describe the behavior of a spin system under magic-angle spinning (MAS) irradiated by a frequency-swept pulse, with emphasis on how to correctly access the (super)adiabaticity and link it to inversion/refocussing performance. We also highlighted a previously unidentified regime intermediate between the high-power, where the radiofrequency (RF) amplitude is greater than twice the spinning frequency, and low-power, where the RF power is less than the spinning frequency, regimes, separated by rotary resonance conditions. The impact of rotary resonance conditions on inversion performance was also carefully examined. We foresee that this rigorous analysis will expand the scope of applications of adiabatic pulses in solid-state NMR and lead to the design of new improved adiabatic pulse schemes.

Secondly, we discussed an ytterbium alkyl compound $Yb[CH(SiMe_3)_2]_3$ with applications as a model system for heterogeneous catalysis. The full characterization of this system was only possible with a combination of X-ray diffraction, EPR, solid-state NMR and state-of-the-art quantum chemical calculations. This work constitutes a more applied example of how understanding the fundamental theory behind paramagnetic interactions can help bridge the gap between different characterization techniques, highlighting their complementarity, and provide an accurate descriptions of both the bonding motifs and electronic structure. Furthermore it pushes the frontier back to include paramagnetic lanthanide organometallic complexes, which whre yet to be characterized at this level of precision.

Lastly, we focused on half-integer quadrupolar nuclei in paramagnetic systems, which in terms of NMR method development were lagging behind. We demonstrated that integration of the Magic-Angle Turning (MAT) experiment with Rotor-Assisted Population Transfer (RAPT) can be used both to identify shifts and to extract a range of magnitudes for their quadrupolar coupling, which in turn can be used to validate proposed structural models. We also presented a new a approach to process Satellite Transition and Multiple-Quantum Magic Angle Spinning (STMAS/MQMAS) spectra by applying a double shearing transformation based on Two-Dimensional One-Pulse processing (TOP). This methodology allows us to analyze slices in the quadrupolar dimension free of bulk magnetic susceptibility induced shift dispersion, and overcomes limitations in the spectral window imposed by rotor-synchronization. We anticipate that these methods will provide new possibilities for solid-state NMR to probe half-integer quadrupolar nuclei in paramagnetic materials.

The work presented in this thesis is expected to open new avenues for studies of paramagnetic systems of increasing complexity and with an even wider range of applications.

7.1 Sammanfattning

Under de senaste åren har betydande framsteg gjorts inom området paramagnetisk kärnmagnetisk resonans (NMR- *"Nuclear Magnetic Resonance"*). Detta gäller såväl utveckling av nya metoder som ny teori. De system som rutinmässigt studeras är idag ganska varierande, i synnerhet inom området fast fas-NMR, och omfattar bland annat batterimaterial, metalloproteiner, heterogena katalysatorer och oorganiska fosforer. Arbetet i denna avhandling bidrar till de senaste framstegen inom detta forskningsfält genom att belysa några mindre utvecklade områden.

I arbetets första del presenterade vi en fullständig och enhetlig beskrivning av de olika ramverken för att beskriva ett spinnsystem under magisk vinkel spinning (MAS - *"Magic-Angle Spinning"*) bestrålat av en frekvenssvept puls genom att använda en kombination av simuleringar och experiment. Här låg fokus på hur man korrekt får tillgång till (super)adiabaticiteten och kan koppla den till inversions-/omfokuseringsprestanda. Vi lyfte också fram en tidigare oidentifierad regim mellan regimerna för hög effekt, där radiofrekvensamplituden (RF) är större än två gånger MAS-frekvensen, och låg effekt, där RF-effekten är mindre än MAS-frekvensen. Dessa regimer separeras genom rotations resonans och inverkan av rotations resonans förhållanden på inversionsprestanda undersöktes också noggrant. Vi förutser att denna rigorösa analys kommer att utöka tillämpningsområdet för adiabatiska pulser i fast fas-NMR, och leda till utformning av nya förbättrade adiabatiska pulsscheman.

Vidare studerade vi en ytterbiumalkylförening $Yb[CH(SiMe_3)_2]_3$ med tillämpningar som ett modellsystem för heterogen katalys. Den fullständiga karakteriseringen av detta system var endast möjlig med en kombination av röntgendiffraktion, EPR, fast fas-NMR och kvantkemiska beräkningar på hög nivå. Detta arbete utgör ett mer tillämpat exempel på hur förståelse av den grundläggande teorin bakom paramagnetiska interaktioner kan hjälpa till att överbrygga gapet mellan olika karakteriseringstekniker, framhäva deras komplementaritet och ge en korrekt beskrivning av både bindningsmotiv och elektronisk struktur. Arbetet möjliggör dessutom studier av paramagnetiska organometalliska lantanidkomplex, som ännu inte har karakteriserats på denna precisionsnivå.

Slutligen fokuserade vi på halvtals kvadrupolära kärnor i paramagnetiska system, som när det gäller utveckling av NMR-metoder släpade efter. Vi visade att integrering av experimentet *"Magic-Angle Turning"* (MAT) med *"Rotor-Assisted Population Transfer"* (RAPT) kan användas både för att identifiera skift och för att extrahera ett antal magnituder för deras kvadrupolkoppling, som i sin tur kan användas för att validera föreslagna strukturella modeller. Vi presenterade också ett nytt tillvägagångssätt för att bearbeta satellitövergångar och *"Satellite Transition e de Multiple-Quantum Magic-Angle Spinning"* (STMAS/MQMAS) genom att tillämpa en dubbelskjuvningstransformation baserad på *"Two-Dimensional One-Pulse"* (TOP). Denna metod tillåter oss att analysera skivor i den kvadrupolära dimensionen fria från bulkmagnetisk susceptibilitetsinducerad skiftdispersion och övervinner begränsningar i det spektrala fönstret som introduceras av rotorsynkronisering. Vi räknar med att dessa metoder kommer leda till nya möjligheter för fast fas-NMR i studier av halvtals kvadrupolära kärnor i paramagnetiska material.

Arbetet som presenteras i denna avhandling förväntas öppna nya möjligheter för studier av paramagnetiska system av ökande komplexitet och med ett ännu bredare tillämpningsområde.

7.2 Resumo

Nos últimos anos, inúmeros progressos foram alcançados no campo de ressonância magnética nuclear (RMN) paramagnética, tanto no desenvolvimento da teoria como na metodologia. Mais especificamente em RMN de estado sólido, a gama de sistemas que hoje em dia são estudados rotinamente é bastante diversificada, variando de materiais para baterias, metaloproteínas, catalisadores heterogêneos e fósforos inorgânicos. O trabalho desenvolvido nesta tese contribui para os progresso recente neste domínio ao abordar algumas áreas menos desenvolvidas.

Em primeiro lugar, começámos por apresentar uma descrição unificada e completa das diferentes formas de descrever o comportamento do sistema de spin sob rotação de ângulo mágico (MAS - *"Magic-Angle Spinning"*) irradiado por um pulso de frequência contínua, através de simulação e experiência, com ênfase em como avaliar correctamente se um pulso é (super)adiabático e em que medida isso afecta o seu desempenho na inversão/refocalização. Destacámos também um regime intermédio, ainda não identificado na literatura, situado entre os regimes de alta potência, onde a amplitude da radiofrequência (RF) é maior que o dobro da frequência de rotação, e de baixa potência, onde a potência de RF é menor que a frequência de rotação, delimitado por condições de ressonância rotativa. O impacto das condições de ressonância rotativa no desempenho da inversão também foi cuidadosamente examinado. Prevemos que esta análise rigorosa expandirá o campo de aplicações de pulsos adiabáticos em RMN de estado sólido e levará ao desenvolvimento de novos e melhorados esquemas de irradiação adiabáticos.

Em segundo lugar, discutimos um sistema alquil itérbio $Yb[CH(SiMe_3)_2]_3$ com aplicações como sistema modelo para catálise heterogénea. A caracterização completa deste sistema só foi possível usando uma combinação de estudos de difracção de raio-X, RPE, RMN de estado sólido e cálculos de química quântica recentemente desenvolvidos. Este trabalho constitui um exemplo de como a compreensão da teoria fundamental por trás das interacções paramagnéticas tem aplicações práticas e pode ajudar a preencher a lacuna entre diferentes técnicas de caracterização, destacando a sua complementaridade, fornecendo uma descrições mais precisa da estrutura química e electrónica de um sistema contendo lantanídeos. Este estudo faz progredir a fronteira para incluir complexos organometálicos de lantanídeos paramagnéticos ainda não caracterizados a este nível de precisão.

Por último, analisámos também núcleos quadrupolares semi-inteiros em sistemas parmagnéticos, que em termos de metodologia se encontram menos desenvolvidos. Demonstrámos que a integrando as sequências de *"Magic-Angle Turning"* (MAT) e *"Rotor-Assisted Population Transfer"* (RAPT) foi possível tanto identificar desvios químicos como extrair as correspondentes gamas de magnitudes de acoplamento quadrupolar, que por sua vez podem ser usadas para validar modelos estruturais. Também apresentámos uma nova abordagem para processar espectros de *"Satellite Transition e de Multiple-Quantum Magic Angle Spinning"* (STMAS/MQMAS), aplicando uma transformação de cisalhamento duplo com base no processamento de *"Two-Dimensional One-Pulse"* (TOP). Esta metodologia permite-nos analisar fatias na dimensão quadrupolar livre de dispersão de desvios químicos induzida por susceptibilidade magnética volumétrica, e supera limitações na janela espectral impostas pela sincronização da rotação. Antecipamos que estes métodos irão trazer novas possibilidades para RMN de estado sólido sondar núcleos quadrupolares semi-inteiros em sistemas paramagnéticos.

O trabalho apresentado nesta tese almeja abrir novos caminhos para estudos de sistemas paramagnéticos com crescente complexidade e com uma gama ainda maior de aplicações.

Acknowledgements

Firstly, I would like to express gratitude to my supervisor Professor Andrew Pell for his guidance and indispensable support during my PhD studies. He was always willing to listen and entertain our ideas in the group which really helped develop my intuition and independence, as well as improve my knowledge of NMR methods. I would also like to thank professor Guido Pintacuda for allowing me to visit the facilities of CRMN in Lyon and for giving me the opportunity to participate in some very interesting ongoing projects.

I would also like to thank my collaborators, professor Ram Seshadri at UC Santa Barbara and professors Gunnar Jeschke and Christophe Copéret at ETH Zurich.

My co-supervisor Professor Gérman Salazar, for his support as well as for allowing me to have access to computational resources.

All the people at CRMN for receiving me so well during my small stay there. Particularly David and Tanguy for their help with the equipment, and Tobias, Marta, Quentin, Thomas and Georges for welcoming me to Lyon, showing me around, and quickly inviting me out for friendly activities.

Professor Arnold Maliniak for his tireless support, particularly during the last year, and for always trying to make sure we had the best conditions possible to carry on our research work.

My two brothers-in-arms in the group, Wassilios and Rihards, not only for our intense discussions and scientific collaborations, without which a lot of the work presented here would not have been possible, but also for all our various endeavors outside work.

The former group members and office mates Aleks, Lorenzo, Min and Lucia. I would particularly like to single out Aleks, who was very patient in teaching me the technical intricacies of solid-state MAS NMR and for introducing me to the field of quantum chemistry.

My former supervisors back in Portugal, professors João Figueirinhas, Pedro Sebastião and Carlos Cruz who initiated me on the field of NMR and with whom I learned how to do research work and my high school teacher Pedro Cabrita for driving me to pursue science as a career.

All my current MMK colleagues, all of which have made my stay in Stockholm all the more enjoyable, particularly Paulo, Laura, Ellie, Wei-Chih, Ira, Misha, Pierre, Alisa, Andrea, Dimi, Ken, Molly, Erik and Roja. Extra thanks to Frederik for helping me out with the Sammanfattning (Swedish summary).

My other friends in Stockholm, specially those who have followed my PhD process more closely: Andreas, Annie, Nikolas, Milla, Margarida and Madalena, and all my friends and family back in Portugal for all the fun times we were able to have, whether via long voice/video calls or when I was back in Portugal for holidays.

A very special thanks to Radost for all her support which helped me retain some semblance of sanity during these intense last couple of months and for having the patience to proofread this document.

* * *

Ao meu pai e à minha mãe quero agradecer imenso por desde cedo terem encorajado a minha curiosidade e por me terem apoiado sempre que precisei. Sem a vossa ajuda com certeza não teria chegado aqui.

May 2022

José Carvalho

References

[1] Hans Wolfgang Spiess. 50th anniversary perspective: The importance of NMR spectroscopy to macromolecular science. *Macromolecules*, 50(5):1761–1777, 2017.

[2] Mattias Edén. NMR studies of oxide-based glasses. *Annual Reports Section "C" (Physical Chemistry)*, 108 (1):177–221, 2012.

[3] Randall Youngman. NMR spectroscopy in glass science: a review of the elements. *Materials*, 11(4):476, 2018.

[4] Rihards Aleksis, Filips Oleskovs, Kristaps Jaudzems, Jens Pahnke, and Henrik Biverstål. Structural studies of amyloid-β peptides: Unlocking the mechanism of aggregation and the associated toxicity. *Biochimie*, 140: 176–192, 2017.

[5] Robert J Messinger, Michel Ménétrier, Elodie Salager, Adrien Boulineau, Mathieu Duttine, Dany Carlier, Jean-Marcel Ateba Mba, Laurence Croguennec, Christian Masquelier, Dominique Massiot, et al. Revealing defects in crystalline lithium-ion battery electrodes by solid-state NMR: applications to $LiVPO_4F$. *Chemistry of Materials*, 27(15):5212–5221, 2015.

[6] Bradley F Chmelka. Materializing opportunities for NMR of solids. *Journal of Magnetic Resonance*, 306: 91–97, 2019.

[7] Aaron J Rossini, Alexandre Zagdoun, Moreno Lelli, Anne Lesage, Christophe Coperet, and Lyndon Emsley. Dynamic nuclear polarization surface enhanced NMR spectroscopy. *Accounts of chemical research*, 46(9): 1942–1951, 2013.

[8] Sharon E Ashbrook. Recent advances in solid-state NMR spectroscopy of quadrupolar nuclei. *Physical Chemistry Chemical Physics*, 11(32):6892–6905, 2009.

[9] Robert Tycko. Solid-state NMR studies of amyloid fibril structure. *Annual review of physical chemistry*, 62: 279–299, 2011.

[10] Melinda J Duer. *Solid state NMR spectroscopy: principles and applications*. John Wiley & Sons, 2008.

[11] Andrew J Pell, Guido Pintacuda, and Clare P Grey. Paramagnetic NMR in solution and the solid state. *Progress in nuclear magnetic resonance spectroscopy*, 111:1–271, 2019.

[12] Norman F Ramsey. Magnetic shielding of nuclei in molecules. *Physical Review*, 78(6):699, 1950.

[13] Teemu O Pennanen and Juha Vaara. Nuclear magnetic resonance chemical shift in an arbitrary electronic spin state. *Physical review letters*, 100(13):133002, 2008.

[14] Ulrich Haeberlen. *Advances in magnetic resonance*, volume 1. Academic Press, 1976.

[15] U Haeberlen and JS Waugh. Coherent averaging effects in magnetic resonance. *Physical Review*, 175(2): 453, 1968.

[16] Sharon E Ashbrook, Jamie McManus, Michael J Thrippleton, and Stephen Wimperis. Second-order cross-term interactions in high-resolution MAS NMR of quadrupolar nuclei. *Progress in Nuclear Magnetic Resonance Spectroscopy*, 55(2):160–181, 2009.

[17] DM Brink and GR Satchler. Angular momentum, oxford library of the physical sciences. 1968.

[18] ER Andrew, A Bradbury, and RG Eades. Nuclear magnetic resonance spectra from a crystal rotated at high speed. *Nature*, 182(4650):1659–1659, 1958.

[19] IJ Lowe. Free induction decays of rotating solids. *Physical Review Letters*, 2(7):285, 1959.

[20] M Matti Maricq and JS Waugh. NMR in rotating solids. *The Journal of Chemical Physics*, 70(7):3300–3316, 1979.

[21] George E Pake. Nuclear resonance absorption in hydrated crystals: fine structure of the proton line. *The Journal of chemical physics*, 16(4):327–336, 1948.

[22] Sharon E Ashbrook and Stephen Wimperis. High-resolution NMR of quadrupolar nuclei in solids: the satellite-transition magic angle spinning (STMAS) experiment. *Progress in Nuclear Magnetic Resonance Spectroscopy*, 45(1-2):53–108, 2004.

[23] Giacomo Parigi, Ladislav Benda, Enrico Ravera, Maurizio Romanelli, and Claudio Luchinat. Pseudocontact shifts and paramagnetic susceptibility in semiempirical and quantum chemistry theories. *The Journal of Chemical Physics*, 150(14):144101, 2019.

[24] Robert J Kurland and Bruce R McGarvey. Isotropic NMR shifts in transition metal complexes: the calculation of the fermi contact and pseudocontact terms. *Journal of Magnetic Resonance (1969)*, 2(3):286–301, 1970.

[25] Seongho Moon and Serguei Patchkovskii. First-principles calculations of paramagnetic NMR shifts. *Calculation of NMR and EPR parameters: theory and applications*, pages 325–338, 2004.

[26] Juha Vaara, Syed Awais Rouf, and Jiri Mares. Magnetic couplings in the chemical shift of paramagnetic NMR. *Journal of chemical theory and computation*, 11(10):4840–4849, 2015.

[27] Lucas Lang, Enrico Ravera, Giacomo Parigi, Claudio Luchinat, and Frank Neese. Solution of a puzzle: High-level quantum-chemical treatment of pseudocontact chemical shifts confirms classic semiempirical theory. *The Journal of Physical Chemistry Letters*, 11(20):8735–8744, 2020. doi: 10.1021/acs.jpclett.0c02462. PMID: 32930598.

[28] Guido Pintacuda, Ah Young Park, Max A Keniry, Nicholas E Dixon, and Gottfried Otting. Lanthanide labeling offers fast NMR approach to 3D structure determinations of protein- protein complexes. *Journal of the American Chemical Society*, 128(11):3696–3702, 2006.

[29] Ivano Bertini, Petri Kursula, Claudio Luchinat, Giacomo Parigi, Juha Vahokoski, Matthias Wilmanns, and Jing Yuan. Accurate solution structures of proteins from X-ray data and a minimal set of NMR data: calmodulin- peptide complexes as examples. *Journal of the American Chemical Society*, 131(14):5134–5144, 2009.

[30] Ivano Bertini, Andrea Giachetti, Claudio Luchinat, Giacomo Parigi, Maxim V Petoukhov, Roberta Pierattelli, Enrico Ravera, and Dmitri I Svergun. Conformational space of flexible biological macromolecules from average data. *Journal of the American Chemical Society*, 132(38):13553–13558, 2010.

[31] Christophe Schmitz and Alexandre MJJ Bonvin. Protein–protein HADDocking using exclusively pseudocontact shifts. *Journal of biomolecular NMR*, 50(3):263–266, 2011.

[32] Christophe Schmitz, Robert Vernon, Gottfried Otting, David Baker, and Thomas Huber. Protein structure determination from pseudocontact shifts using ROSETTA. *Journal of molecular biology*, 416(5):668–677, 2012.

[33] Yoshitaka Hiruma, Mathias AS Hass, Yuki Kikui, Wei-Min Liu, Betül Ölmez, Simon P Skinner, Anneloes Blok, Alexander Kloosterman, Hiroyasu Koteishi, Frank Löhr, et al. The structure of the cytochrome P450cam–putidaredoxin complex determined by paramagnetic NMR spectroscopy and crystallography. *Journal of molecular biology*, 425(22):4353–4365, 2013.

[34] GN Murshudov, AA Vagin, and EJ Dodson. Acta crystallogr. sect. d biol. crystallogr. 1997.

[35] Duncan J Crick, Jue X Wang, Bim Graham, James D Swarbrick, Helen R Mott, and Daniel Nietlispach. Integral membrane protein structure determination using pseudocontact shifts. *Journal of biomolecular NMR*, 61(3):197–207, 2015.

[36] Davide Sala, Andrea Giachetti, Claudio Luchinat, and Antonio Rosato. A protocol for the refinement of NMR structures using simultaneously pseudocontact shift restraints from multiple lanthanide ions. *Journal of biomolecular NMR*, 66(3):175–185, 2016.

[37] Mathias AS Hass and Marcellus Ubbink. Structure determination of protein–protein complexes with long-range anisotropic paramagnetic NMR restraints. *Current opinion in structural biology*, 24:45–53, 2014.

[38] Ivano Bertini, Vito Calderone, Linda Cerofolini, Marco Fragai, Carlos FGC Geraldes, Petr Hermann, Claudio Luchinat, Giacomo Parigi, and João MC Teixeira. The catalytic domain of MMP-1 studied through tagged lanthanides. *FEBS letters*, 586(5):557–567, 2012.

[39] Ivano Bertini, Claudio Luchinat, and Giacomo Parigi. Magnetic susceptibility in paramagnetic NMR. *Progress in Nuclear Magnetic Resonance Spectroscopy*, 40(3):249, 2002.

[40] M Alla and E Lippmaa. Resolution limits in magic-angle rotation NMR spectra of polycrystalline solids. *Chemical Physics Letters*, 87(1):30–33, 1982.

[41] U Schwerk, D Michel, and M Pruski. Local magnetic field distribution in a polycrystalline sample exposed to a strong magnetic field. *Journal of Magnetic Resonance, Series A*, 119(2):157–164, 1996.

[42] Atsushi Kubo, Thomas P Spaniol, and Takehiko Terao. The effect of bulk magnetic susceptibility on solid state NMR spectra of paramagnetic compounds. *Journal of Magnetic Resonance*, 133(2):330–340, 1998.

[43] John David Jackson. Classical electrodynamics, 1999.

[44] DL VanderHart, William L Earl, and AN Garroway. Resolution in ^{13}C NMR of organic solids using high-power proton decoupling and magic-angle sample spinning. *Journal of Magnetic Resonance (1969)*, 44(2): 361–401, 1981.

[45] Roberta Pigliapochi, Liam O'Brien, Andrew J Pell, Michael W Gaultois, Yuri Janssen, Peter G Khalifah, and Clare P Grey. When do anisotropic magnetic susceptibilities lead to large NMR shifts? exploring particle shape effects in the battery electrode material $LiFePO_4$. *Journal of the American Chemical Society*, 141(33): 13089–13100, 2019.

[46] G. Kervern. *High-resolution solid-state NMR of paramagnetic molecules*. PhD thesis, École Normale Suérieure de Lyon, 2008.

[47] Nicolaas Bloembergen, Edward Mills Purcell, and Robert V Pound. Relaxation effects in nuclear magnetic resonance absorption. *Physical review*, 73(7):679, 1948.

[48] Ivano Bertini, Claudio Luchinat, Giacomo Parigi, and Enrico Ravera. *NMR of Paramagnetic Molecules*. Elsevier, 2017.

[49] Frank Jensen. Computational chemistry: The exciting opportunities and the boring details. *Israel Journal of Chemistry*, 2021.

[50] Trygve Helgaker, Poul Jorgensen, and Jeppe Olsen. *Molecular electronic-structure theory*. John Wiley & Sons, 2014.

[51] Jean-Pierre Schermann. *Spectroscopy and modeling of biomolecular building blocks*. Elsevier, 2007.

[52] Björn O Roos. *Lecture notes in quantum chemistry*, volume 58. Springer, 1992.

[53] Celestino Angeli, Renzo Cimiraglia, S Evangelisti, T Leininger, and J-P Malrieu. Introduction of *n*-electron valence states for multireference perturbation theory. *The Journal of Chemical Physics*, 114(23):10252–10264, 2001.

[54] Celestino Angeli, Renzo Cimiraglia, and Jean-Paul Malrieu. *n*-electron valence state perturbation theory: A spinless formulation and an efficient implementation of the strongly contracted and of the partially contracted variants. *The Journal of chemical physics*, 117(20):9138–9153, 2002.

[55] Celestino Angeli, Mariachiara Pastore, and Renzo Cimiraglia. New perspectives in multireference perturbation theory: the *n*-electron valence state approach. *Theoretical Chemistry Accounts*, 117(5):743–754, 2007.

[56] Rodney J. Bartlett. Coupled-cluster approach to molecular structure and spectra: a step toward predictive quantum chemistry. *The Journal of Physical Chemistry*, 93(5):1697–1708, 1989.

[57] Wolfram Koch and Max C Holthausen. *A chemist's guide to density functional theory*. John Wiley & Sons, 2015.

[58] AV Arbuznikov. Hybrid exchange correlation functionals and potentials: Concept elaboration. *Journal of Structural Chemistry*, 48(1):S1–S31, 2007.

[59] Lars Goerigk, Andreas Hansen, Christoph Bauer, Stephan Ehrlich, Asim Najibi, and Stefan Grimme. A look at the density functional theory zoo with the advanced GMTKN55 database for general main group thermochemistry, kinetics and noncovalent interactions. *Phys. Chem. Chem. Phys.*, 19:32184–32215, 2017. doi: 10.1039/C7CP04913G.

[60] Frank Jensen. Atomic orbital basis sets. *Wiley Interdisciplinary Reviews: Computational Molecular Science*, 3(3):273–295, 2013.

[61] Xiaoyan Cao and Michael Dolg. Pseudopotentials and modelpotentials. *Wiley Interdisciplinary Reviews: Computational Molecular Science*, 1(2):200–210, 2011.

[62] IJ Bush, S Tomić, BG Searle, G Mallia, CL Bailey, B Montanari, L Bernasconi, JM Carr, and NM Harrison. Parallel implementation of the ab initio CRYSTAL program: electronic structure calculations for periodic systems. *Proceedings of the Royal Society A: Mathematical, Physical and Engineering Sciences*, 467(2131): 2112–2126, 2011.

[63] MT Sananes, A Tuel, and JC Volta. A study by ^{31}P NMR spin-echo mapping of VPO catalysts: I. characterization of the reference phases. *Journal of Catalysis*, 145(2):251–255, 1994.

[64] MT Sananes, A Tuel, JC Volta, and GJ Hutchings. Characterization of different precursors and activated vanadium phosphate catalysts by ^{31}P NMR spin echo mapping. *Journal of Catalysis;(United States)*, 148(1), 1994.

[65] MT Sananes and A Tuel. Magnetic properties of vanadium phosphorus oxide catalysts studied by spin echo mapping ^{31}P NMR. *Journal of the Chemical Society, Chemical Communications*, (13):1323–1324, 1995.

[66] YY Tong. Nuclear spin-echo fourier-transform mapping spectroscopy for broad NMR lines in solids. *Journal of Magnetic Resonance, Series A*, 119(1):22–28, 1996.

[67] L Canesson and A Tuel. The first observation of “NMR-invisible phosphorus” incobalt-substituted aluminophosphate molecular sieves. *Chemical Communications*, (2):241–242, 1997.

[68] Laurence Canesson, Yves Boudeville, and Alain Tuel. Local environment of phosphorus atoms in CoAPO4-n molecular sieves: A ^{31}P NMR study. *Journal of the American Chemical Society*, 119(44):10754–10762, 1997.

[69] Gregor Mali, Alenka Ristić, and Vence̒slav Kauc̒ic. ^{31}P NMR as a tool for studying incorporation of Ni, Co, Fe, and Mn into aluminophosphate zeotypes. *The Journal of Physical Chemistry B*, 109(21):10711–10716, 2005.

[70] Jongsik Kim, Derek S Middlemiss, Natasha A Chernova, Ben YX Zhu, Christian Masquelier, and Clare P Grey. Linking local environments and hyperfine shifts: A combined experimental and theoretical ^{31}P and ^{7}Li solid-state NMR study of paramagnetic Fe (III) phosphates. *Journal of the American Chemical Society*, 132(47):16825–16840, 2010.

[71] Dominique Massiot, Ian Farnan, Nathalie Gautier, Dominique Trumeau, Arlette Trokiner, and Jean Pierre Coutures. ^{71}Ga and ^{69}Ga nuclear magnetic resonance study of β-Ga_2O_3: resolution of four-and six-fold coordinated ga sites in static conditions. *Solid State Nuclear Magnetic Resonance*, 4(4):241–248, 1995.

[72] Robert W Schurko, Sungsool Wi, and Lucio Frydman. Dynamic effects on the powder line shapes of half-integer quadrupolar nuclei: a solid-state NMR study of XO_4-groups. *The Journal of Physical Chemistry A*, 106(1):51–62, 2002.

[73] Jason T Ash and Philip J Grandinetti. Solid-state NMR characterization of ^{69}Ga and ^{71}Ga in crystalline solids. *Magnetic Resonance in Chemistry*, 44(9):823–831, 2006.

[74] Luke A O’Dell, Aaron J Rossini, and Robert W Schurko. Acquisition of ultra-wideline NMR spectra from quadrupolar nuclei by frequency stepped WURST-QCPMG. *Chemical physics letters*, 468(4-6):330–335, 2009.

[75] Luke A O’Dell and Robert W Schurko. Fast and simple acquisition of solid-state ^{14}N NMR spectra with signal enhancement via population transfer. *Journal of the American Chemical Society*, 131(19):6658–6659, 2009.

[76] Marie-Hélène Thibault, Bryan EG Lucier, Robert W Schurko, and Frédéric-Georges Fontaine. Synthesis and solid-state characterization of platinum complexes with hexadentate amino-and iminophosphine ligands. *Dalton Transactions*, (37):7701–7716, 2009.

[77] Alan W. MacGregor, Luke A. O’Dell, and Robert W. Schurko. New methods for the acquisition of ultra-wideline solid-state NMR spectra of spin-1/2 nuclides. *Journal of Magnetic Resonance*, 208(1):103 – 113, 2011. ISSN 1090-7807.

[78] Andrew J Pell, Raphaële J Clément, Clare P Grey, Lyndon Emsley, and Guido Pintacuda. Frequency-stepped acquisition in nuclear magnetic resonance spectroscopy under magic angle spinning. *The Journal of chemical physics*, 138(11):114201, 2013.

[79] Michael Garwood and Lance DelaBarre. The return of the frequency sweep: designing adiabatic pulses for contemporary NMR. *Journal of magnetic resonance*, 153(2):155–177, 2001.

[80] J Baum, R Tycko, and Pines. Broadband and adiabatic inversion of a two-level system by phase-modulated pulses. *Physical Review A*, 32(6):3435, 1985.

[81] Tsang-Lin Hwang, Peter CM Van Zijl, and Michael Garwood. Fast broadband inversion by adiabatic pulses, 1998.

[82] E Kupcče and R Freeman. Adiabatic pulses for wideband inversion and broadband decoupling. *Journal of magnetic resonance. Series A (Print)*, 115(2):273–276, 1995.

[83] R.R. Ernst, G. Bodenhausen, and A. Wokaun. *Principles of Nuclear Magnetic Resonance in One and Two Dimensions*. Clarendon Press, 1987. ISBN 9780198556299.

[84] Michaël Deschamps, Gwendal Kervern, Dominique Massiot, Guido Pintacuda, Lyndon Emsley, and Philip J. Grandinetti. Superadiabaticity in magnetic resonance. *The Journal of Chemical Physics*, 129(20):204110, 2008. doi: 10.1063/1.3012356.

[85] Bert Heise, Jörg Leppert, and Ramadurai Ramachandran. REDOR with adiabatic dephasing pulses. *Journal of Magnetic Resonance*, 146(1):181 – 187, 2000. ISSN 1090-7807. doi: https://doi.org/10.1006/jmre.2000.2129.

[86] Michael Victor Berry. Histories of adiabatic quantum transitions. *Proceedings of the Royal Society of London. A. Mathematical and Physical Sciences*, 429(1876):61–72, 1990.

[87] Michael Victor Berry. Quantal phase factors accompanying adiabatic changes. *Proceedings of the Royal Society of London. A. Mathematical and Physical Sciences*, 392(1802):45–57, 1984. doi: 10.1098/rspa.1984.0023.

[88] P Caravatti, G Bodenhausen, and RR Ernst. Selective pulse experiments in high-resolution solid state NMR. *Journal of Magnetic Resonance (1969)*, 55(1):88–103, 1983.

[89] Andrew J Pell, Gwendal Kervern, Lyndon Emsley, Michaël Deschamps, Dominique Massiot, Philip J Grandinetti, and Guido Pintacuda. Broadband inversion for MAS NMR with single-sideband-selective adiabatic pulses. *The Journal of chemical physics*, 134(2):024117, 2011.

[90] Ingo Scholz, Jacco D van Beek, and Matthias Ernst. Operator-based floquet theory in solid-state NMR. *Solid state nuclear magnetic resonance*, 37(3-4):39–59, 2010.

[91] Michal Leskes, PK Madhu, and Shimon Vega. Floquet theory in solid-state nuclear magnetic resonance. *Progress in nuclear magnetic resonance spectroscopy*, 57(4):345–380, 2010.

[92] F Bloch and A Siegert. Magnetic resonance for nonrotating fields. *Physical Review*, 57(6):522, 1940.

[93] Zhe-Hong Gan and David M Grant. Rotational resonance in a spin-lock field for solid state NMR. *Chemical physics letters*, 168(3-4):304–308, 1990.

[94] T.L. Hwang and A.J. Shaka. Water suppression that works. excitation sculpting using arbitrary wave-forms and pulsed-field gradients. *Journal of Magnetic Resonance, Series A*, 112(2):275 – 279, 1995. ISSN 1064-1858. doi: https://doi.org/10.1006/jmra.1995.1047.

[95] Katherine Stott, Jonathan Stonehouse, James Keeler, Tsang-Lin Hwang, and A. J. Shaka. Excitation sculpting in high-resolution nuclear magnetic resonance spectroscopy: Application to selective noe experiments. *Journal of the American Chemical Society*, 117(14):4199–4200, 1995. doi: 10.1021/ja00119a048.

[96] Andrew J Pell and Guido Pintacuda. Broadband solid-state MAS NMR of paramagnetic systems. *Progress in nuclear magnetic resonance spectroscopy*, 84:33–72, 2015.

[97] Jian Zhi Hu, DW Alderman, CH Ye, RJ Pugmire, and DM Grant. An isotropic chemical shift-chemical shift anisotropy magic-angle slow-spinning 2D NMR experiment. *Journal of Magnetic Resonance, Series A*, 105 (1):82–87, 1993.

[98] Oleg N Antzutkin, SC Shekar, and Malcolm H Levitt. Two-dimensional sideband separation in magic-angle-spinning NMR. *Journal of Magnetic Resonance, Series A*, 115(1):7–19, 1995.

[99] Raphaële J Clément, Andrew J Pell, Derek S Middlemiss, Fiona C Strobridge, Joel K Miller, M Stanley Whittingham, Lyndon Emsley, Clare P Grey, and Guido Pintacuda. Spin-transfer pathways in paramagnetic lithium transition-metal phosphates from combined broadband isotropic solid-state MAS NMR spectroscopy and DFT calculations. *Journal of the American Chemical Society*, 134(41):17178–17185, 2012.

[100] Etienne Grau, Anne Lesage, Sébastien Norsic, Christophe Copéret, Vincent Monteil, and Philippe Sautet. Tetrahydrofuran in $TiCl_4$/THF/$MgCl_2$: a non-innocent ligand for supported ziegler–natta polymerization catalysts. *ACS Catalysis*, 3(1):52–56, 2013.

[101] Pierrick Berruyer, Moreno Lelli, Matthew P Conley, Daniel L Silverio, Cory M Widdifield, Georges Siddiqi, David Gajan, Anne Lesage, Christophe Copéret, and Lyndon Emsley. Three-dimensional structure determination of surface sites. *Journal of the American Chemical Society*, 139(2):849–855, 2017.

[102] Christophe Copéret, Wei-Chih Liao, Christopher P Gordon, and Ta-Chung Ong. Active sites in supported single-site catalysts: An NMR perspective. *Journal of the American Chemical Society*, 139(31):10588–10596, 2017.

[103] Christophe Coperet, Aleix Comas-Vives, Matthew P Conley, Deven P Estes, Alexey Fedorov, Victor Mougel, Haruki Nagae, Francisco Nunez-Zarur, and Pavel A Zhizhko. Surface organometallic and coordination chemistry toward single-site heterogeneous catalysts: strategies, methods, structures, and activities. *Chemical reviews*, 116(2):323–421, 2016.

[104] Monica Trueba and Stefano P Trasatti. γ-alumina as a support for catalysts: a review of fundamental aspects. *European journal of inorganic chemistry*, 2005(17):3393–3403, 2005.

[105] Guilherme Sippel Machado, Kelly Aparecida Dias de Freitas Castro, Omar José de Lima, Eduardo José Nassar, Kátia Jorge Ciuffi, and Shirley Nakagaki. Aluminosilicate obtained by sol–gel process as support for an anionic iron porphyrin: Development of a selective and reusable catalyst for oxidation reactions. *Colloids and Surfaces A: Physicochemical and Engineering Aspects*, 349(1-3):162–169, 2009.

[106] Matthew P Conley, Giuseppe Lapadula, Kevin Sanders, David Gajan, Anne Lesage, Iker Del Rosal, Laurent Maron, Wayne W Lukens, Christophe Coperet, and Richard A Andersen. The nature of secondary interactions at electrophilic metal sites of molecular and silica-supported organolutetium complexes from solid-state NMR spectroscopy. *Journal of the American Chemical Society*, 138(11):3831–3843, 2016.

[107] John P Perdew, Matthias Ernzerhof, and Kieron Burke. Rationale for mixing exact exchange with density functional approximations. *The Journal of chemical physics*, 105(22):9982–9985, 1996.

[108] A Becke. Density-functional thermochemistry. III. the role of exact exchange. *J. Chem. Phys*, 98:5648, 1993.

[109] Carlo Adamo and Vincenzo Barone. Toward reliable density functional methods without adjustable parameters: The PBE0 model. *The Journal of chemical physics*, 110(13):6158–6170, 1999.

[110] Stefan Grimme, Jens Antony, Stephan Ehrlich, and Helge Krieg. A consistent and accurate ab-initio parametrization of density functional dispersion correction (DFT-D) for the 94 elements H-Pu. *The Journal of chemical physics*, 132(15):154104, 2010.

[111] E van Lenthe, Evert-Jan Baerends, and Jaap G Snijders. Relativistic regular two-component hamiltonians. *The Journal of chemical physics*, 99(6):4597–4610, 1993.

[112] Florian Allouche, Daniel Klose, Christopher P Gordon, Anton Ashuiev, Michael Wörle, Vidmantas Kalendra, Victor Mougel, Christophe Copéret, and Gunnar Jeschke. Low-coordinated titanium (III) alkyl—molecular and surface—complexes: Detailed structure from advanced EPR spectroscopy. *Angewandte Chemie*, 130 (44):14741–14745, 2018.

[113] Wolfgang Scherer and G Sean McGrady. Agostic interactions in d^0 metal alkyl complexes. *Angewandte Chemie International Edition*, 43(14):1782–1806, 2004.

[114] P Schosseler, Th Wacker, and A Schweiger. Pulsed ELDOR detected NMR. *Chemical physics letters*, 224 (3-4):319–324, 1994.

[115] Per Siegbahn, Anders Heiberg, Björn Roos, and Bernard Levy. A comparison of the super-CI and the newton-raphson scheme in the complete active space SCF method. *Physica Scripta*, 21(3-4):323, 1980.

[116] Björn O Roos, Peter R Taylor, and Per EM Sigbahn. A complete active space SCF method (CASSCF) using a density matrix formulated super-CI approach. *Chemical Physics*, 48(2):157–173, 1980.

[117] Per EM Siegbahn, Jan Almlöf, Anders Heiberg, and Björn O Roos. The complete active space SCF (CASSCF) method in a newton–raphson formulation with application to the HNO molecule. *The Journal of Chemical Physics*, 74(4):2384–2396, 1981.

[118] Markus Reiher. Douglas–kroll–hess theory: a relativistic electrons-only theory for chemistry. *Theoretical Chemistry Accounts*, 116(1):241–252, 2006.

[119] Reinhold F Fink. Spin-component-scaled møller–plesset (SCS-MP) perturbation theory: a generalization of the mp approach with improved properties. *The Journal of chemical physics*, 133(17):174113, 2010.

[120] Simone Kossmann and Frank Neese. Correlated ab initio spin densities for larger molecules: orbital-optimized spin-component-scaled MP2 method. *The Journal of Physical Chemistry A*, 114(43):11768–11781, 2010.

[121] Rulin Feng, Thomas J. Duignan, and Jochen Autschbach. Electron-nucleus hyperfine coupling calculated from restricted active space wavefunctions and an exact two-component Hamiltonian. *Journal of Chemical Theory and Computation*, 17(1):255–268, 2021. doi: 10.1021/acs.jctc.0c01005. PMID: 33385321.

[122] Raphaële J Clément, Andrew J Pell, Derek S Middlemiss, Fiona C Strobridge, Joel K Miller, M Stanley Whittingham, Lyndon Emsley, Clare P Grey, and Guido Pintacuda. Spin-transfer pathways in paramagnetic lithium transition-metal phosphates from combined broadband isotropic solid-state MAS NMR spectroscopy and DFT calculations. *Journal of the American Chemical Society*, 134(41):17178–17185, 2012.

[123] Andrew W Hing, Shimon Vega, and Jacob Schaefer. Transferred-echo double-resonance NMR. *Journal of Magnetic Resonance (1969)*, 96(1):205–209, 1992.

[124] Gwendal Kervern, Guido Pintacuda, Yong Zhang, Eric Oldfield, Charbel Roukoss, Emile Kuntz, Eberhardt Herdtweck, Jean-Marie Basset, Sylvian Cadars, Anne Lesage, et al. Solid-state NMR of a paramagnetic DIAD-FeII catalyst: Sensitivity, resolution enhancement, and structure-based assignments. *Journal of the American Chemical Society*, 128(41):13545–13552, 2006.

[125] Teemu O Pennanen and Juha Vaara. Density-functional calculations of relativistic spin-orbit effects on nuclear magnetic shielding in paramagnetic molecules. *The Journal of chemical physics*, 123(17):174102, 2005.

[126] Stanisław K Zaremba. Good lattice points, discrepancy, and numerical integration. *Annali di matematica pura ed applicata*, 73(1):293–317, 1966.

[127] Harold Conroy. Molecular schrödinger equation. VIII. a new method for the evaluation of multidimensional integrals. *The Journal of Chemical Physics*, 47(12):5307–5318, 1967.

[128] Vera B Cheng, Henry H Suzukawa Jr, and Max Wolfsberg. Investigations of a nonrandom numerical method for multidimensional integration. *The Journal of Chemical Physics*, 59(8):3992–3999, 1973.

[129] Jianmin Tao, John P Perdew, Viktor N Staroverov, and Gustavo E Scuseria. Climbing the density functional ladder: Nonempirical meta–generalized gradient approximation designed for molecules and solids. *Physical Review Letters*, 91(14):146401, 2003.

[130] Jochen Autschbach, Serguei Patchkovskii, and Ben Pritchard. Calculation of hyperfine tensors and paramagnetic NMR shifts using the relativistic zeroth-order regular approximation and density functional theory. *Journal of Chemical Theory and Computation*, 7(7):2175–2188, 2011.

[131] Robert P Young, Corbin R Lewis, Chen Yang, Luther Wang, James K Harper, and Leonard J Mueller. Tensorview: A software tool for displaying NMR tensors. *Magnetic Resonance in Chemistry*, 57(5):211–223, 2019.

[132] Lucio Frydman and John S Harwood. Isotropic spectra of half-integer quadrupolar spins from bidimensional magic-angle spinning NMR. *Journal of the American Chemical Society*, 117(19):5367–5368, 1995.

[133] Zhehong Gan. Isotropic NMR spectra of half-integer quadrupolar nuclei using satellite transitions and magic-angle spinning. *Journal of the American Chemical Society*, 122(13):3242–3243, 2000.

[134] Veronika Vitzthum, Marc A Caporini, Simone Ulzega, and Geoffrey Bodenhausen. Broadband excitation and indirect detection of nitrogen-14 in rotating solids using delays alternating with nutation (DANTE). *Journal of Magnetic Resonance*, 212(1):234–239, 2011.

[135] Rihards Aleksis and Andrew J Pell. Low-power synchronous helical pulse sequences for large anisotropic interactions in MAS NMR: Double-quantum excitation of ^{14}N. *The Journal of Chemical Physics*, 153(24): 244202, 2020.

[136] Sasa Antonijevic and Stephen Wimperis. Separation of quadrupolar and chemical/paramagnetic shift interactions in two-dimensional ^{2}H (I= 1) nuclear magnetic resonance spectroscopy. *The Journal of chemical physics*, 122(4):044312, 2005.

[137] Brennan J Walder, Krishna K Dey, Michael C Davis, Jay H Baltisberger, and Philip J Grandinetti. Two-dimensional NMR measurement and point dipole model prediction of paramagnetic shift tensors in solids. *The Journal of Chemical Physics*, 142(1):014201, 2015.

[138] Rihards Aleksis and Andrew J Pell. Separation of quadrupolar and paramagnetic shift interactions in high-resolution nuclear magnetic resonance of spinning powders. *The Journal of Chemical Physics*, 155(9): 094202, 2021.

[139] Zhi Yao, Hyung-Tae Kwak, Dimitris Sakellariou, Lyndon Emsley, and Philip J Grandinetti. Sensitivity enhancement of the central transition NMR signal of quadrupolar nuclei under magic-angle spinning. *Chemical Physics Letters*, 327(1-2):85–90, 2000.

[140] Nicole M Trease, Krishna K Dey, and Philip J Grandinetti. Optimum excitation of "enhanced" central transition populations. *Journal of Magnetic Resonance*, 200(2):334–339, 2009.

[141] Subramanian Prasad, Hyung-Tae Kwak, Ted Clark, and Philip J Grandinetti. A simple technique for determining nuclear quadrupole coupling constants with RAPT solid-state NMR spectroscopy. *Journal of the American Chemical Society*, 124(18):4964–4965, 2002.

[142] Jeongjae Lee, Ieuan D Seymour, Andrew J Pell, Siân E Dutton, and Clare P Grey. A systematic study of ^{25}Mg NMR in paramagnetic transition metal oxides: applications to Mg-ion battery materials. *Physical Chemistry Chemical Physics*, 19(1):613–625, 2017.

[143] Philip J Grandinetti, Jason T Ash, and Nicole M Trease. Symmetry pathways in solid-state NMR . *Progress in Nuclear Magnetic Resonance Spectroscopy*, 59(2):121–196, 2010.

[144] Geoffrey Bodenhausen, Herbert Kogler, and RR Ernst. Selection of coherence-transfer pathways in NMR pulse experiments. *Journal of Magnetic Resonance (1969)*, 58(3):370–388, 1984.

[145] B Blümich, P Blümler, and J Jansen. Presentation of sideband envelopes by two-dimensional one-pulse (TOP) spectroscopy. *Solid state nuclear magnetic resonance*, 1(2):111–113, 1992.

[146] Peter Blümler, J Jansen, and B Blümich. Two-dimensional one-pulse rotational echo spectra. *Solid State Nucl. Magn. Reson.*, 3(4):237–240, 1994.

[147] Dominique Massiot, Julian Hiet, Nadia Pellerin, Franck Fayon, Michael Deschamps, Stefan Steuernagel, and Philip J. Grandinetti. Two-dimensional one pulse MAS of half-integer quadrupolar nuclei. *J. Magn. Reson.*, 181(2):310 – 315, 2006. ISSN 1090-7807.

[148] Brennan J Walder, Krishna K Dey, Derrick C Kaseman, Jay H Baltisberger, and Philip J Grandinetti. Sideband separation experiments in NMR with phase incremented echo train acquisition. *J. Chem. Phys.*, 138(17): 174203, 2013.

[149] Federico M. Paruzzo, Brennan J. Walder, and Lyndon Emsley. Line narrowing in ^{1}H NMR of powdered organic solids with TOP-CT-MAS experiments at ultra-fast MAS. *J. Magn. Reson.*, 305:131 – 137, 2019. ISSN 1090-7807.

[150] Andrew J. Pell, Richard A. E. Edden, and James Keeler. Broadband proton-decoupled proton spectra. *Magnetic Resonance in Chemistry*, 45(4):296–316, 4 2007.

[151] Jason T Ash, Nicole M Trease, and Philip J Grandinetti. Separating chemical shift and quadrupolar anisotropies via multiple-quantum NMR spectroscopy. *Journal of the American Chemical Society*, 130(33): 10858–10859, 2008.

[152] Hyung-Tae Kwak and Zhehong Gan. Double-quantum filtered STMAS. *Journal of Magnetic Resonance*, 164(2):369 – 372, 2003. ISSN 1090-7807.

[153] Raphaele J Clement, Derek S Middlemiss, Ieuan D Seymour, Andrew J Ilott, and Clare P Grey. Insights into the nature and evolution upon electrochemical cycling of planar defects in the β-NaMnO$_2$ na-ion battery cathode: An NMR and first-principles density functional theory approach. *Chemistry of Materials*, 28(22): 8228–8239, 2016.

[154] Pierre Florian, Monique Gervais, André Douy, Dominique Massiot, and Jean-Pierre Coutures. A multinuclear multiple-field nuclear magnetic resonance study of the Y_2O_3-Al_2O_3 phase diagram. *The Journal of Physical Chemistry B*, 105(2):379–391, 2001.

[155] Thomas Vosegaard, Inger P Byriel, Dorota A Pawlak, Krzysztof Wozniak, and Hans J Jakobsen. Crystal structure studies on the garnet $Y_3Al_5O_{12}$ by ^{27}Al single-crystal NMR spectroscopy. *Journal of the American Chemical Society*, 120(31):7900–7904, 1998.